Self-assembly of binary block copolymers and supramolecular copolymer complexes

Faber, Martin Gerrit

Self-Assembly of Binary Block Copolymers and Supramolecular Copolymer Complexes

Martin Faber

Self-Assembly of Binary Block Copolymers and Supramolecular Copolymer Complexes

Martin Faber
PhD thesis
University of Groningen

December 2013

Zernike Institute PhD thesis series 2013-25
ISBN (print) : 978-90-367-6627-2
ISBN (electronic) : 978-90-367-6628-9
ISSN : 1570-1530

The research presented in this thesis was performed in the Polymer Chemistry group of the Zernike Institute for Advanced Materials at the University of Groningen, The Netherlands. This work was funded by The Netherlands Organization for Scientific Research (NWO).

Printed by Ipskamp Drukkers B.V. Enschede

RIJKSUNIVERSITEIT GRONINGEN

Self-Assembly of Binary Block Copolymers and Supramolecular Copolymer Complexes

Proefschrift

ter verkrijging van het doctoraat in de
Wiskunde en Natuurwetenschappen
aan de Rijksuniversiteit Groningen
op gezag van de
Rector Magnificus, dr. E. Sterken,
in het openbaar te verdedigen op
maandag 2 december 2013
om 14.30 uur

door

Martin Gerrit Faber

geboren op 23 augustus 1975
te Sneek

Promotores:	Prof. dr. G. ten Brinke
	Prof. dr. K. Loos
Beoordelingscommissie:	Prof. dr. O. Ikkala
	Prof. dr. Y. Matsushita
	Prof. dr. V. Abetz

Voor Lizette

Contents

Chapter 3

Chapter 4

Chapter 5

Chapter 1

Introduction

1.1 Polymers

Polymers are long and flexible molecules (macromolecules) formed by connecting a large number of monomer units via covalent bonds. Thanks to their large range of intriguing properties, polymers are being used extensively in consumer goods as well as in advanced technologies. The simplest form is a homopolymer in which the polymer consists of chemically identical monomers. Block copolymers are formed by covalent bonding of two or more chemically distinct polymer chains. Examples of di-, tri-, star, comb and multiblock copolymers are depicted in Figure 1.1.

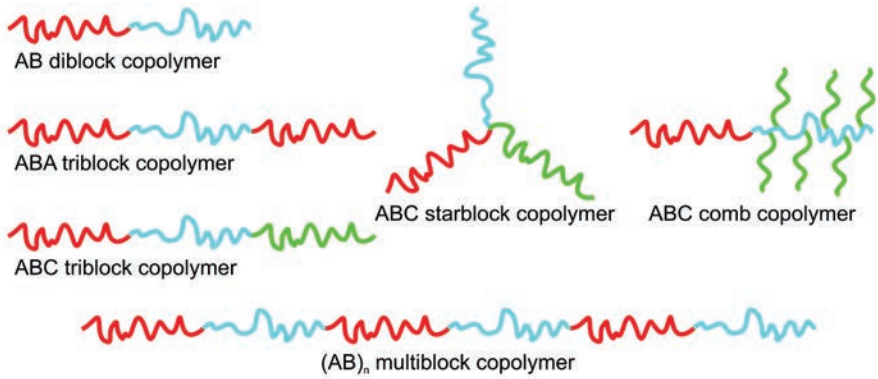

Figure 1.1 Examples of possible block copolymer architectures.

Polymer chains form short-lived knots, so called entanglements, in the bulk. These entanglements influence the flow behavior of molten polymers as well as the mechanical strength in the solid state. The properties of the polymers such as mechanical strength, glass transition temperature, viscoelasticity, etc., are further determined by the type of monomer used. These properties are extremely important for their practical applications.

Fine-tuning the properties can be accomplished by mixing two polymers. However, two chemically different polymers do not tend to mix very well due to unfavorable interactions. Even when the respective monomers can be mixed homogeneously, the polymers generally do not and phase separate instead. The reason for this is the very low entropy of mixing of polymers. When two polymers of which the chains consist of

N monomers are mixed, only the first segment can choose a new position, the other N - 1 cannot. This causes the entropy of mixing to be about $1/N$ lower compared to the mixing of their monomers.

Mixing of two polymers, A and B, is normally realized using extruders in which rigorous mechanical mixing occurs at temperatures high enough that both polymers are in the liquid state. The shearing of the high viscosity fluids produces fine dispersions. Demixing is prevented by fast cooling below temperatures at which the polymers become solid. However, demixing starts again upon increasing the temperature. To increase the stability of the formed dispersions, AB diblock copolymers can be added which act as compatibilizers, a polymer analogue of a surfactant. These AB diblock copolymers segregate to the interface between the two polymers where they lower the interfacial tension.

Besides acting as compatibilizers between two immiscible polymers, diblock copolymers are also of interest for their unique behavior in solution and in the bulk. While mixtures of polymers separate macroscopically, diblock copolymers cannot since the chemically different polymers are covalently bonded. Therefore, the separation takes place on the nanometer scale in which a number of well-ordered structures, having a domain spacing ranging from approximately 5 to 100 nm, are formed via self-assembly. The formation of these nanoscale morphologies and their possible application in nanotechnology is the reason that the synthesis and self-assembly of block copolymers have been the focus of a large number of studies.[1-5] New routes are explored to gain further control on morphologies formed and to broaden their applicability, frequently inspired by the results obtained using theoretical modeling and computer simulations. Advances in polymer synthesis resulted in tailor made block copolymers having various architectures and consisting of a whole range of monomers. The self-assembly of these block copolymers resulted in intriguing nanoscaled morphologies in bulk, thin films, and in solution. Subtle changes in the chemical structure of the monomers and the copolymer architecture or the creation of supramolecular copolymer complexes via addition of components which have specific interactions with the copolymer studied, can lead to enhanced control of the morphologies formed or even result in exciting new morphologies.[6-13]

The boundary between theoretical and experimental research on block copolymer synthesis and self-assembly is an exciting area of research and has been the inspiration

for the investigations presented in this thesis. To provide an overview of the scientific foundation of this research the remainder of the introduction is organized as follows. Section 1.2 presents a more detailed discussion on the two polymerization techniques used to synthesize the (block) copolymers investigated. Section 1.3 provides a reference framework for the thesis by presenting an overview of the self-assembly of diblock copolymers, binary multiblock copolymers and supramolecular copolymer complexes. Finally, Section 1.4 provides an overview of the research presented in Chapters 2 to 5.

1.2 Synthesis of block copolymers

The experimental study of the self-assembly of block copolymers starts with the preparation of well-defined block copolymers. This requires a polymerization technique in which undesired transfer and termination reactions are absent. Furthermore, all the chains should be allowed to grow for the same amount of time. Two polymerization techniques fulfilling these requirements were applied to synthesize the polymers studied, namely: living anionic polymerization[14-16] and reversible addition-fragmentation chain transfer (RAFT).[17, 18]

1.2.1 Living anionic polymerization

Living anionic polymerization of styrene and isoprene was successfully demonstrated in the 1950's by M. Szwarc.[14, 15] It was discovered that the polymerization continued until all the monomers had reacted and that upon adding new monomer the polymerization continued. This started the development of the field of living anionic polymerization.[16]

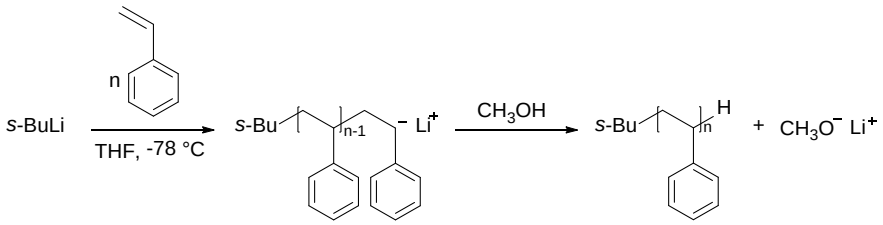

Scheme 1.1 Synthetic pathway for the living anionic polymerization of polystyrene using *sec*-butyllithium (*s*-BuLi) as the initiator.

A typical example of an anionic polymerization of styrene is given in Scheme 1.1. The reactive chain end is a carbanion that is mostly introduced using an organometallic initiator such as butyllithium (monofunctional initiator) or sodium naphtalenide (bifunctional initionator). The monomers should be able to stabilize the anion via electron withdrawing groups otherwise initiation will not occur. The initiation should also be very fast compared to the propagation to ensure all the polymers grow at the same time. The fast initiation together with the fact that due to Coulomb repulsion termination by combination or disproportionation is impossible, results in polymers characterized by a narrow polydispersity, PDI $<$ 1.1. To end the reaction, terminating agents are added after complete consumption of monomer. This can be a proton donor such as methanol and ethanol or specific agents that provide functional end groups.[19]
Many block copolymers reported were synthesized using living anionic polymerization. Sequential addition of chemically different monomers to the living carbanion end of a polymer chain has led to for example, AB diblock-,[20-22] ABA- and ABC triblock-,[23-27] ABCDE pentablock,[28] and $(AB)_n$ multiblock copolymers.[29-32] Sequential addition of different monomers leads to block copolymers with a precisely controlled architecture. However, when synthesizing block copolymers the variation in reactivity of the carbanion species of the different monomers has to be taken into account. The sequence in which the blocks are polymerized is crucial to successfully obtain the desired block copolymer. It is essential to start the polymerization with the monomer having the least stable anion in order to be able to transfer the carbanion to the next monomer.
The number of compatible monomers is limited and protection often necessary. Since carbanions are strong nucleophiles, polar functional groups cannot be used without suitable protection. Much effort has been undertaken to increase the number of monomers accessible by using different initiators[16] or using protection of the functional groups.[33]
To be able to polymerize successfully very controlled conditions are necessary to circumvent secondary reactions and control the kinetics of the polymerization. This means a tight control on the temperature and extremely pure reagents and solvents. Very low reaction temperatures are often necessary to suppress side reactions.

1.2.2 Reversible addition-fragmentation chain transfer (RAFT) polymerization

The rigorous conditions necessary for living anionic polymerization and the constriction on suitable monomers stimulated scientist to find new polymerization techniques that overcome these challenges. These efforts resulted in a controlled polymerization methods based on free radical polymerization like atom-transfer radical polymerization (ATRP),[34] nitroxide mediated polymerization (NMP),[35] and reversible addition-fragmentation chain transfer (RAFT) polymerization.[17, 18] This opened up new synthetic pathways to polymerize monomers containing a vinyl group while maintaining a narrow polydispersity. In free radical polymerizations the extreme nonselective reactivity results in an abundant presence of chain transfer- and termination reaction which results in a broad molecular weight distribution. Controlled radical polymerizations circumvent the unwanted side reactions by introducing a reversible end-capping of the active chain. Via this method the majority of the growing polymer chains are maintained in a dormant state for long periods of time. This reduces the overall concentration of free radicals drastically and therefore reduces the chance on irreversible termination. This results in a molecular weight which increases linearly with conversion and a much narrower chain length distribution. Above that, the resulting polymer chains are end-capped after the polymerization and can be reactivated again in order to extend the polymer chain with the same monomer or a second type of monomer to give a block copolymer.[36, 37] Via the controlled radical polymerizations unique block copolymers having different architectures could be synthesized using a whole range of monomers.[36-39]

The development of RAFT polymerization using dithioesters as chain transfer agents was first reported in 1998.[18] It is a radical polymerization in which the reversible deactivation of the propagating chain using a RAFT agent provides a controlled character. The RAFT agent is a special chain transfer agent (CTA) which can transfer polymer chains reversibly resulting in a rapid equilibrium between the active and dormant chains. Adding the RAFT agent in excess compared to the initiator results in the majority of the polymer chains formed being end-capped by the RAFT agent and

reducing the amount of bimolecular terminations. Dithioesters are used as CTA since they can accommodate two polymer chains plus one radical in the dormant state. Figure 1.2 displays the general structure of the RAFT agent which contains R- and Z substituents which determine the effectiveness.[17, 40] The Z substituent is connected to the carbon atom of the thioester and will strongly affect the stability of the thiocarbonyl-thio radical intermediate.[17, 41] Increasing the stability of the radical intermediate using a specific Z-group will make termination less probable, but the overall rate of polymerization will decrease.

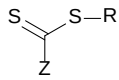

Figure 1.2 The general structure of the RAFT agent in which the Z-group affects the stability of the thiocarbonyl-thio radical intermediate and the R-group functions as the re-initiating group.

The R-group, directly connected to sulphur, functions as the re-initiating group.[17, 41] The R substituent should be a better leaving group compared to the dormant polymer chain to ensure fast initiation. The radical formed should therefore be stable enough to induce fragmentation. However, it still needs to be reactive enough towards monomer in order to initiate effectively.

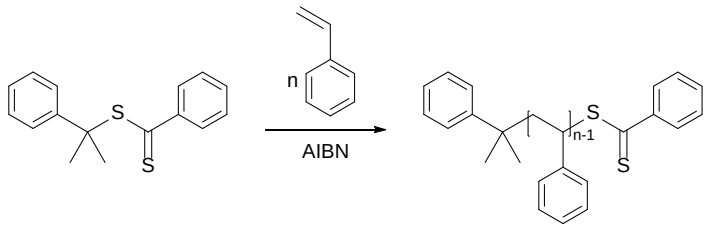

Scheme 1.2 Synthetic pathway for the RAFT polymerization of polystyrene using cumyl dithiobenzoate as the RAFT agent and AIBN as the initiator of the reaction.

The RAFT agent plays an important role in the polymerization; therefore it should be selected with great care. Both the Z- and the R-group can be optimized for the

monomer which needs to be polymerized. An example of a RAFT polymerization of styrene using cumyl dithiobenzoate as the RAFT agent and azobis(isobutyronitril) (AIBN) as initiator is shown in Scheme 1.2.

All the reactions associated with free radical polymerizations are also present during the RAFT polymerization, i.e., initiation, propagation, and termination. The radical source is only needed to start the reaction. The formation of one radical is in principle enough to start the initiation and propagation of all polymer chains. Although accompanied by higher chance of chain termination, increasing the amount of radicals increases the rate of the reaction. In general, the ratio of initiator compared to the RAFT agent is kept low in order to initiate the majority of the polymer chains by the R substituent.

The RAFT agent provides a chain activation-deactivation mechanism as depicted in Scheme 1.3. A fast exchange between the propagating species, P_n and P_m, is required to ensure al chains have equal opportunity to grow. The equilibrium should favor the dormant intermediate to prevent termination as much as possible.

After ending the reaction the resulting polymers are end-capped with the dithioester functionality. In other words, a macro-chain-transfer agent (macro-CTA) has been formed and via reinitiation with new monomer block copolymers can be obtained.

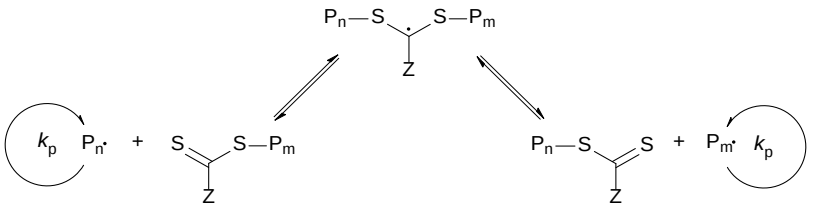

Scheme 1.3 The main equilibrium of the RAFT polymerization.

Most monomers that can be polymerized via radical polymerization can also be used in RAFT polymerization. Monomers containing functionalities like OH-, COOH-, or NR_2-groups can be used without protecting groups. Polymerization in the bulk, solution, emulsion, and suspension, can be employed and even aqueous and protic solvents are possible. The main drawback of the RAFT polymerization is that there is always a fraction of dead chains present after the reaction due to the use of the initiator.

RAFT together with living anionic polymerization provide suitable methods to obtain tailor-made polymers with the desired properties using a large range of monomers and combining them into block copolymers having different architectures. Employing different polymerization techniques consecutively by using the end-functionalized polymer obtained via the first polymerization technique as a macroinitiator for the second polymerization technique broadens the possibilities even further.[39, 42-44]

1.3 Block copolymer self-assembly

1.3.1 Diblock copolymers

The driving force behind the microphase separation is an unfavorable enthalpy of mixing combined with a small entropy of mixing. The formation of a morphology is depending on the competition between interfacial tension (enthalpic contribution) between the two blocks and the elastic stretching (entropic contribution). On microphase separation, the two blocks minimize the interfacial area by separating from each other. This results in chain stretching away from the preferred coiled chain conformation. When these two opposing effects are balanced, the minimum of the free energy, the equilibrium structure is found.

The self-assembly of an AB diblock copolymer depends on three parameters, namely: the volume fractions of the blocks, f_{A} and f_{B}, the overall degree of polymerization, N, and the Flory-Huggins interaction parameter, $\chi_{\mathrm{A,B}}$.

The overall degree of polymerization (based on a common reference segment), N, is proportional to the molecular weight. The block copolymer composition is expressed as the volume fractions of component A, f_{A}:

$$f_{\mathrm{A}} = \frac{N_{\mathrm{A}}}{N_{\mathrm{A}} + N_{\mathrm{B}}} = \frac{N_{\mathrm{A}}}{N} \qquad 1.1$$

Here, N_{A} and N_{B} are the number of A- and B monomer units and N is the total number of monomers.

The interaction between two dissimilar monomers is given by the dimensionless interaction parameter, $\chi_{A,B}$, which is inversely proportional to temperature. The

χ-parameter is a measure for the incompatibility between the two blocks and is inversely dependent on the temperature, T as shown in equation 1.2.

$$\chi_{\mathrm{A,B}} = \left(\frac{z}{k_{\mathrm{B}}T}\right)\left[\varepsilon_{\mathrm{AB}} - \frac{1}{2}(\varepsilon_{\mathrm{AA}} + \varepsilon_{\mathrm{BB}})\right] \qquad 1.2$$

Here, z is the number of nearest neighbours per repeat unit in the polymer, k_{B} is the Boltzman constant, T is the temperature, and $\varepsilon_{\mathrm{AB}}$, $\varepsilon_{\mathrm{AA}}$, and $\varepsilon_{\mathrm{BB}}$ are the interaction energies per repeat unit of AB, AA, and BB interactions, respectively. The term $k_{\mathrm{B}}T$ is a measure for the thermal energy. In diblock copolymers where interactions such as hydrogen-bonding or ionic charges are not playing any role, $\chi_{\mathrm{A,B}}$ is often positive and small.

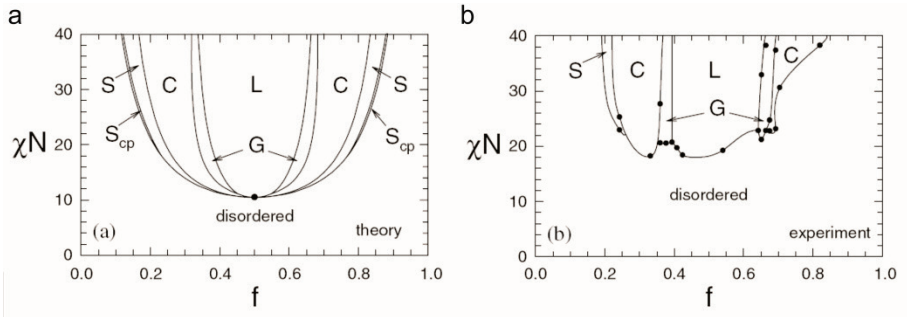

Figure 1.3 Block copolymer phase diagram as calculated using the self-consistent mean-field theory (a) and the experimental phase diagram for polystyrene-*b*-polyisoprene diblock copolymers (b). Reproduced with permission from: Matsen, M.W. *J. Phys.: Condens. Matter* **2002**, 14, R21-R47. Copyright 2002 IOP Publishing.

Calculations using self-consistent mean-field theory resulted in the phase diagram for diblock copolymers in which the equilibrium morphologies are shown as function of the segregation product χN and f_{A} as depicted in Figure 1.3a.[45-47] If there are repulsive interactions between A and B blocks, $\chi N > 0$, while in the case of favorable (attractive) interactions between the blocks, $\chi N < 0$. Increasing χN results in a larger incompatibility between the blocks. For χN two limit values are defined, namely, the weak segregation limit ($\chi N < 10$) and the strong segregation limit ($\chi N \gg 10$). For a symmetric diblock copolymer the order-disorder transition (ODT) was predicted to occur at $\chi N = 10.5$.

To verify the theoretical phase diagram, investigations using polystyrene-*b*-polyisoprene diblock copolymers (PS-*b*-PI) were undertaken.[20, 46, 48] A remarkable similarity, although somewhat less symmetric, between the theoretical and the experimental diagram is found as can be seen in Figure 1.3b.
At a fixed χN of about 30, increasing the f_A results in order-to-order transitions (OOT) starting from body-centered cubic spheres (S), through hexagonally packed cylinders (C) and bicontinuous gyroid (G), to lamellae (L) (Figure 1.4).[46] Complete mixing is observed for $\chi N < 20$.

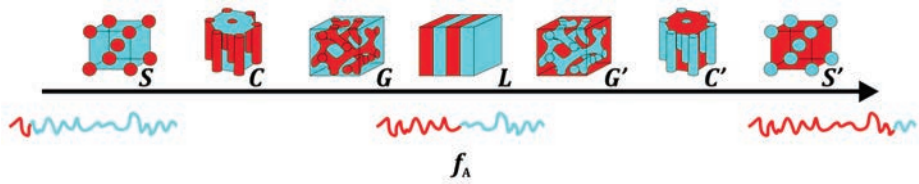

Figure 1.4 Schematic representation of the morphologies observed in diblock copolymers with increasing volume fraction f_A. The illustrated stuctures are body-centered cubic spheres (S), hexagonally packed cylinders (C), bicontinous gyroid (G) and lamellae (L).

1.3.2 Binary multiblock copolymers

The most straightforward linear AB multiblock copolymers are buildup of n AB diblocks, $(AB)_n$, as depicted in Figure 1.5a. Such systems were synthesized using sequential anionic polymerization of styrene (S) and isoprene (I) blocks to result in $(SI)_n$ multiblock copolymers of which the phase behavior was investigated.[29-32] Alternating lamellar nanostructures were observed in the strongly segregated multiblock copolymers. It was found that the lamellar domain spacing decreased with increasing n.[29, 31] Sheared $(SI)_n$ samples showed an transition from bridged to looped conformations when a low shear rate and a large strain amplitude is applied.[32]

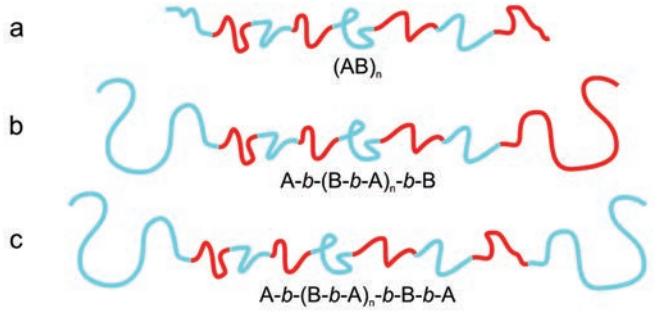

Figure 1.5 Illustration of three binary multiblock copolymer architectures: (a) $(AB)_n$, (b) A-*b*-(B-*b*-A)$_n$-*b*-B-*b*-A, and (c) A-*b*-(B-*b*-A)$_n$-*b*-B.

Increasing the chain length of the outer blocks to a significantly different size than the inner blocks leads to for example an A-*b*-(B-*b*-A)$_n$-*b*-B-*b*-A or A-*b*-(B-*b*-A)$_n$-*b*-B, schematically depicted in Figures 1.5b and 1.5c. The latter being fully symmetric in composition. In such systems, two intrinsic different length scales are present which can give rise to a self-assembled hierarchical morphology even though only two chemically different species are used. Several theoretical studies describe the self-assembly of such binary systems.[49-57] In these studies hierarchical lamellar morphologies were found consisting of smaller inner lamellae formed by the small inner blocks inside large lamellae formed by the outer blocks. The presence and the number of thin internal layers depend on the segregation and on the number and relative length of the internal diblocks n.

Experimentally Matsushita et al.[58] showed examples using an S-(IS)$_4$-I-S undecablock copolymer (asymmetric in composition) in which the two outer S blocks are considerably longer than the inner blocks. Parallel lamellar-in-lamellar morphologies were observed in which the long polystyrene chains formed thick lamellae with in between three thin lamellar domains consisting of the short middle blocks, I,S, and I, depicted in Figure 1.6.

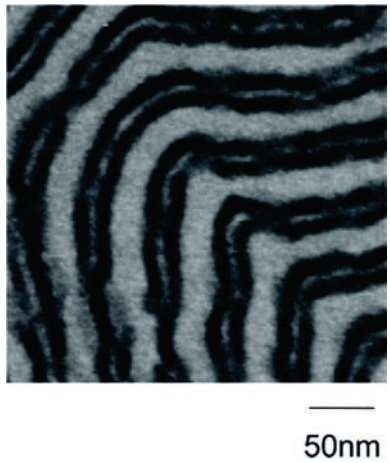

Figure 1.6 TEM image of a S-(IS)$_4$-I-S undecablock copolymer showing a hierarchical lamellar-in-lamellar morphology. Reprinted with permission from Nagata, Y.; Masuda, J.; Noro, A.; Cho, D. Y.; Takano, A.; Matsushita, Y. *Macromolecules* **2005**, 38, (24), 10220-10225. Copyright 2005 American Chemical Society.

1.3.3 Supramolecular copolymer complexes

Another interesting approach in copolymer self-assembly is the use of supramolecular copolymer complexes.[12, 13, 59, 60] Specifically of interest are the low molecular weight side chains noncovalently bonded to a polymer backbone to form comb-shaped supramolecules. These systems gathered a lot of attention theoretically as well as experimentally.[13, 60, 61]

A striking example of such a system is the hydrogen-bonding of 3-pentadecylphenol (PDP) to poly(4-vinylpyridine) (P4VP) shown first in 1996.[62-64] PDP can donate hydrogen via the phenol group, while pyridine group of P4VP can accept hydrogen (Figure 1.7). Microphase separated lamellar morphologies were found in the complex formed due to the phase separation of the long nonpolar alkyl chains from the polar P4VP/phenol complex.

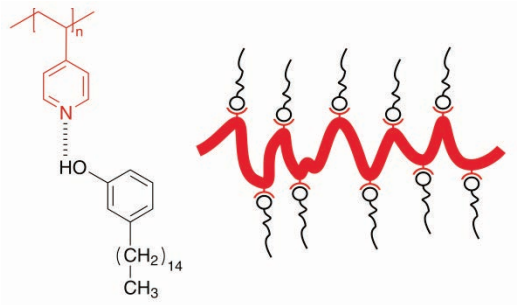

Figure 1.7 Schematic representation of the supramolecular comb copolymer complex between P4VP and PDP.

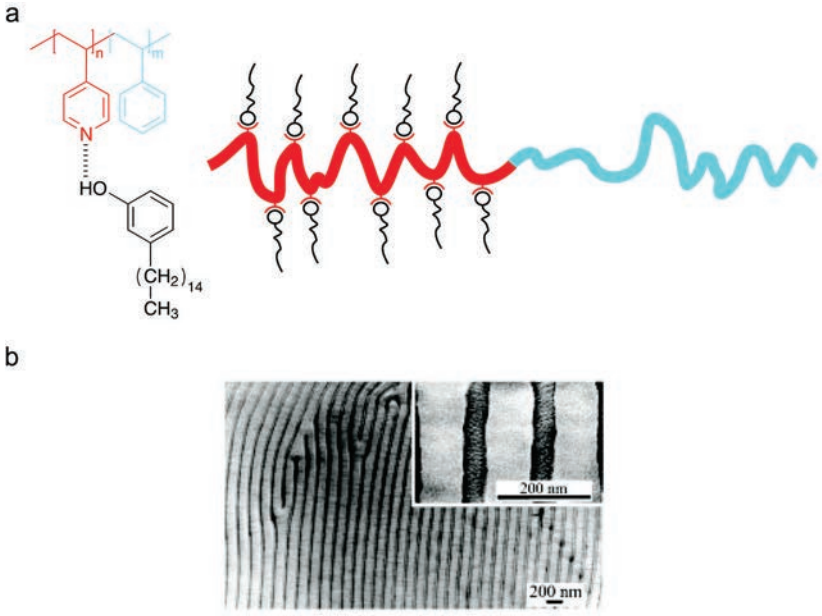

Figure 1.8 Schematical representation of the supramolecular comb-coil copolymer complex between PS-*b*-P4VP and PDP (a) and the TEM micrograph of the microphase separated lamellar-in-lamellar morphology observed in such systems. Reprinted with permission from Ruokolainen, J.; Saariaho, M.; Ikkala, O.; ten Brinke, G.; Thomas, E. L.; Torkkeli, M.; Serimaa, R. *Macromolecules* **1999**, 32, (4), 1152-1158. Copyright 1999 American Chemical Society.

This principle was developed further using AB diblock copolymers consisting of a styrene- and a 4-vinylpyridine block, PS-*b*-P4VP. Addition of PDP resulted in a PS-*b*-P4VP(PDP) comb-coil copolymer in which the comb is formed by the P4VP(PDP) complex and the coil by the styrene block (Figure 1.8a).[65] Self-assembly of the supramolecular complex resulted in a hierarchical perpendicular lamellar-in-lamellar morphology in which PS is phase separated from the P4VP(PDP) complex and within this complex, the PDP alkyl tails are phase separated from phenol/P4VP. A TEM image of such a system with PDP is shown in Figure 1.8b.[66] An interesting benefit of the supramolecular complex is the ability to fine-tune the self-assembled structures formed using the same parent block copolymer by varying the amount of amphiphiles added.[67] Changing the amount of surfactant per 4VP unit results in changing the fraction of the P4VP(PDP) comb (f_{comb}) and alters the interaction between the blocks. Effectively, it is a tool to move through the phase diagram and allows the formation of the desired structure without having to synthesize new polymers. Furthermore, after establishing the right structure, there is the possibility to "empty" the structure by selectively dissolving the low molecular weight amphiphile to form nanotemplates.[68-71]

1.4 Thesis overview

The previous sections showed only a few of the highlights of the research in the self-assembly of block copolymers, focusing on binary block copolymers and supramolecular complexes using hydrogen-bonding. Although many more interesting examples can be shown, e.g., triblock copolymers or multiblock tercopolymers, the foundation of the work presented in the coming chapters was formed using the examples described above. By applying subtle changes to the block copolymers investigated, new and exciting effects can often be observed having a possible application in novel functional nanomaterials. It is therefore very important to obtain a better understanding of these tools available to access and fine-tune specific morphologies, the domain spacing and the responsiveness to external stimuli. The objective of this thesis is to extend this investigation on the self-assembly of binary

block copolymers and supramolecular copolymer complexes. The thesis is outlined as follows.

Chapter 2 describes the synthesis and self-assembly of four poly(*tert*-butoxystyrene)-*b*-poly(4-vinylpyridine) diblock copolymers having different weight fractions of 4-vinylpyridine. Although the system is quite similar to polystyrene-*b*-poly(4-vinylpyridine) diblock copolymers, the addition of the *tert*-butoxy group at the para position of the phenyl ring of styrene changes the interaction parameter and therefore also the phase behavior observed. The four morphologies observed are discussed in relation with the interaction parameter.

Chapter 3 investigates the self-assembly of symmetric A-*b*-(B-*b*-A)$_n$-*b*-B multiblock copolymers synthesized via sequential living anionic polymerization of styrene and *tert*-butoxystyrene. The appearance of a lamellar-in-lamellar morphology is discussed in connection with theoretical predictions.

Chapter 4 investigates a supramolecular copolymer complex in which alkylpyridine amphiphiles are hydrogen-bonded to a poly(*p*-hydroxystyrene) polymer backbone. Although this complex is similar to the poly(4-vinylpyridine)/3-pentacedylphenol complexes described in Section 1.3.3, remarkable differences are observed in the self-assembly of these two systems. These differences, together with the stability of the hydrogen-bonding, the lamellar morphologies formed and the influence of the length of the alkyl tail of the alkyl pyridine amphiphiles, are discussed.

Chapter 5 describes the synthesis and self-assembly of a supramolecular double comb diblock copolymer in which 3-pentadecylphenol is hydrogen-bonded to both blocks of a poly(4-vinylpyridine)-*b*-poly(*N*,*N*-dimethylacrylamide) diblock copolymer. The hydrogen-bonding of the amphiphiles to both blocks and the formation of a unique hierarchical structure are discussed.

1.5 References

1. Bates, F. S.; Fredrickson, G. H. *Annu. Rev. Phys. Chem.* **1990,** 41, 525-557.
2. Hajduk, D. A.; Harper, P. E.; Gruner, S. M.; Honeker, C. C.; Kim, G.; Thomas, E. L.; Fetters, L. J. *Macromolecules* **1994,** 27, (15), 4063-4075.
3. Hamley, I. W., *The physics of block copolymers*. Oxford University Press: 1998.
4. Abetz, V.; Simon, P. F. W., Phase Behaviour and Morphologies of Block Copolymers. In *Block Copolymers I*, Springer Berlin Heidelberg: Berlin, 2005; Vol. 189, pp 125-212.
5. Matsushita, Y. *Macromolecules* **2007,** 40, (4), 771-776.
6. Darling, S. B. *Prog. Polym. Sci.* **2007,** 32, (10), 1152-1204.
7. Park, C.; Yoon, J.; Thomas, E. L. *Polymer* **2003,** 44, (22), 6725-6760.
8. Kim, J. K.; Yang, S. Y.; Lee, Y.; Kim, Y. *Prog. Polym. Sci.* **2010,** 35, (11), 1325-1349.
9. Lazzari, M.; Lopez-Quintela, M. A. *Adv. Mater.* **2003,** 15, (19), 1583-1594.
10. Ruzette, A. V.; Leibler, L. *Nat. Mater.* **2005,** 4, (1), 19-31.
11. Hamley, I. W. *Angew. Chem.-Int. Edit.* **2003,** 42, (15), 1692-1712.
12. Lehn, J. M. *Polym. Int.* **2002,** 51, (10), 825-839.
13. Pollino, J. M.; Weck, M. *Chem. Soc. Rev.* **2005,** 34, (3), 193-207.
14. Szwarc, M. *Nature* **1956,** 178, (4543), 1168-1169.
15. Szwarc, M.; Levy, M.; Milkovich, R. *J. Am. Chem. Soc.* **1956,** 78, (11), 2656-2657.
16. Baskaran, D.; Muller, A. H. E. *Prog. Polym. Sci.* **2007,** 32, (2), 173-219.
17. Moad, G.; Rizzardo, E.; Thang, S. H. *Polymer* **2008,** 49, (5), 1079-1131.
18. Chiefari, J.; Chong, Y. K.; Ercole, F.; Krstina, J.; Jeffery, J.; Le, T. P. T.; Mayadunne, R. T. A.; Meijs, G. F.; Moad, C. L.; Moad, G.; Rizzardo, E.; Thang, S. H. *Macromolecules* **1998,** 31, (16), 5559-5562.
19. Hirao, A.; Hayashi, M. *Acta Polym.* **1999,** 50, (7), 219-231.
20. Khandpur, A. K.; Forster, S.; Bates, F. S.; Hamley, I. W.; Ryan, A. J.; Bras, W.; Almdal, K.; Mortensen, K. *Macromolecules* **1995,** 28, (26), 8796-8806.
21. Takenaka, M.; Wakada, T.; Akasaka, S.; Nishitsuji, S.; Saijo, K.; Shimizu, H.; Kim, M. I.; Hasegawa, H. *Macromolecules* **2007,** 40, (13), 4399-4402.
22. Rahman, S. S. A.; Kawaguchi, D.; Matsushita, Y. *Macromolecules* **2011,** 44, (8), 2799-2807.
23. Mai, S. M.; Mingvanish, W.; Turner, S. C.; Chaibundit, C.; Fairclough, J. P. A.; Heatley, F.; Matsen, M. W.; Ryan, A. J.; Booth, C. *Macromolecules* **2000,** 33, (14), 5124-5130.

24. Taribagil, R. R.; Hillmyer, M. A.; Lodge, T. P. *Macromolecules* **2010,** 43, (12), 5396-5404.
25. Mogi, Y.; Kotsuji, H.; Kaneko, Y.; Mori, K.; Matsushita, Y.; Noda, I. *Macromolecules* **1992,** 25, (20), 5408-5411.
26. Ludwigs, S.; Boker, A.; Abetz, V.; Muller, A. H. E.; Krausch, G. *Polymer* **2003,** 44, (22), 6815-6823.
27. Krappe, U.; Stadler, R.; Voigt-Martin, I. *Macromolecules* **1995,** 28, (13), 4558-4561.
28. Ekizoglou, N.; Hadjichristidis, N. *J. Polym. Sci. Pol. Chem.* **2002,** 40, (13), 2166-2170.
29. Matsushita, Y.; Mogi, Y.; Mukai, H.; Watanabe, J.; Noda, I. *Polymer* **1994,** 35, (2), 246-249.
30. Wu, L. F.; Cochran, E. W.; Lodge, T. P.; Bates, F. S. *Macromolecules* **2004,** 37, (9), 3360-3368.
31. Smith, S. D.; Spontak, R. J.; Satkowski, M. M.; Ashraf, A.; Heape, A. K.; Lin, J. S. *Polymer* **1994,** 35, (21), 4527-4536.
32. Wu, L. F.; Lodge, T. P.; Bates, F. S. *Macromolecules* **2004,** 37, (22), 8184-8187.
33. Hirao, A.; Loykulnant, S.; Ishizone, T. *Prog. Polym. Sci.* **2002,** 27, (8), 1399-1471.
34. Matyjaszewski, K.; Xia, J. H. *Chem. Rev.* **2001,** 101, (9), 2921-2990.
35. Hawker, C. J.; Bosman, A. W.; Harth, E. *Chem. Rev.* **2001,** 101, (12), 3661-3688.
36. Braunecker, W. A.; Matyjaszewski, K. *Prog. Polym. Sci.* **2007,** 32, (1), 93-146.
37. Rizzardo, E.; Chiefari, J.; Chong, B. Y. K.; Ercole, F.; Krstina, J.; Jeffery, J.; Le, T. P. T.; Mayadunne, R. T. A.; Meijs, G. F.; Moad, C. L.; Moad, G.; Thang, S. H. *Macromol. Symp.* **1999,** 143, 291-307.
38. Coessens, V.; Pintauer, T.; Matyjaszewski, K. *Prog. Polym. Sci.* **2001,** 26, (3), 337-377.
39. Gregory, A.; Stenzel, M. H. *Prog. Polym. Sci.* **2012,** 37, (1), 38-105.
40. Moad, G.; Rizzardo, E.; Thang, S. H. *Aust. J. Chem.* **2005,** 58, (6), 379-410.
41. Perrier, S.; Takolpuckdee, P. *J. Polym. Sci. Pol. Chem.* **2005,** 43, (22), 5347-5393.
42. Sugihara, S.; Iwata, K.; Miura, S.; Ma'Radzi, A. H.; Maeda, Y. *Polymer* **2013,** 54, (3), 1043-1052.
43. Pafiti, K. S.; Patrickios, C. S.; Filiz, V.; Rangou, S.; Abetz, C.; Abetz, V. *J. Polym. Sci. Pol. Chem.* **2013,** 51, (1), 213-221.

44. Yin, L. G.; Dalsin, M. C.; Sizovs, A.; Reineke, T. M.; Hillmyer, M. A. *Macromolecules* **2012,** 45, (10), 4322-4332.
45. Matsen, M. W.; Schick, M. *Phys. Rev. Lett.* **1994,** 72, (16), 2660-2663.
46. Bates, F. S.; Fredrickson, G. H. *Phys. Today* **1999,** 52, (2), 32-38.
47. Matsen, M. W.; Bates, F. S. *Macromolecules* **1996,** 29, (4), 1091-1098.
48. Matsen, M. W. *J. Phys.-Condes. Matter* **2002,** 14, (2), R21-R47.
49. Nap, R. J.; Kok, C.; ten Brinke, G.; Kuchanov, S. I. *Eur. Phys. J. E* **2001,** 4, (4), 515-519.
50. Nap, R.; Sushko, N.; Erukhimovich, I.; ten Brinke, G. *Macromolecules* **2006,** 39, (19), 6765-6770.
51. Klymko, T.; Subbotin, A.; ten Brinke, G. *J. Chem. Phys.* **2008,** 129, (11), 114902.
52. Smirnova, Y. G.; ten Brinke, G.; Erukhimovich, I. Y. *Polym. Sci. Ser. A* **2005,** 47, (5), 430-435.
53. Smirnova, Y. G.; ten Brinke, G.; Erukhimovich, I. Y. *J. Chem. Phys.* **2006,** 124, (5), 054907.
54. Kriksin, Y. A.; Erukhimovich, I. Y.; Khalatur, P. G.; Smirnova, Y. G.; ten Brinke, G. *J. Chem. Phys.* **2008,** 128, (24), 244903.
55. Kriksin, Y. A.; Erukhimovich, I. Y.; Smirnova, Y. G.; Khalatur, P. G.; ten Brinke, G. *J. Chem. Phys.* **2009,** 130, (20), 204901.
56. Kuchanov, S.; Pichugin, V.; Ten Brinke, G. *e-Polymers* **2006,** 12, 1-31.
57. Kuchanov, S.; Pichugin, V.; Ten Brinke, G. *Europhys. Lett.* **2006,** 76, (5), 959-964.
58. Nagata, Y.; Masuda, J.; Noro, A.; Cho, D. Y.; Takano, A.; Matsushita, Y. *Macromolecules* **2005,** 38, (24), 10220-10225.
59. Kato, T.; Mizoshita, N.; Kishimoto, K. *Angew. Chem.-Int. Edit.* **2006,** 45, (1), 38-68.
60. ten Brinke, G.; Ruokolainen, J.; Ikkala, O., Supramolecular Materials Based On Hydrogen-Bonded Polymers. In *Hydrogen Bonded Polymers*, Springer Berlin Heidelberg: Berlin, 2007; Vol. 207, pp 113-177.
61. Osuji, C. O.; Chao, C. Y.; Ober, C. K.; Thomas, E. L. *Macromolecules* **2006,** 39, (9), 3114-3117.
62. Ruokolainen, J.; ten Brinke, G.; Ikkala, O.; Torkkeli, M.; Serimaa, R. *Macromolecules* **1996,** 29, (10), 3409-3415.
63. Ruokolainen, J.; Torkkeli, M.; Serimaa, R.; Komanschek, B. E.; Ikkala, O.; ten Brinke, G. *Phys. Rev. E* **1996,** 54, (6), 6646-6649.
64. TenBrinke, G.; Ruokolainen, J.; Ikkala, O. *Europhys. Lett.* **1996,** 35, (2), 91-95.

65. Ruokolainen, J.; Makinen, R.; Torkkeli, M.; Makela, T.; Serimaa, R.; ten Brinke, G.; Ikkala, O. *Science* **1998,** 280, (5363), 557-560.
66. Ruokolainen, J.; Saariaho, M.; Ikkala, O.; ten Brinke, G.; Thomas, E. L.; Torkkeli, M.; Serimaa, R. *Macromolecules* **1999,** 32, (4), 1152-1158.
67. Vukovic, I.; Voortman, T. P.; Merino, D. H.; Portale, G.; Hiekkataipale, P.; Ruokolainen, J.; ten Brinke, G.; Loos, K. *Macromolecules* **2012,** 45, (8), 3503-3512.
68. Sidorenko, A.; Tokarev, I.; Minko, S.; Stamm, M. *J. Am. Chem. Soc.* **2003,** 125, (40), 12211-12216.
69. van Zoelen, W.; Bondzic, S.; Landaluce, T. F.; Brondijk, J.; Loos, K.; Schouten, A. J.; Rudolf, P.; ten Brinke, G. *Polymer* **2009,** 50, (15), 3617-3625.
70. du Sart, G. G.; Vukovic, I.; Vukovic, Z.; Polushkin, E.; Hiekkataipale, P.; Ruokolainen, J.; Loos, K.; ten Brinke, G. *Macromol. Rapid Commun.* **2011,** 32, (4), 366-370.
71. Vukovic, I.; Punzhin, S.; Vukovic, Z.; Onck, P.; De Hosson, J. T. M.; ten Brinke, G.; Loos, K. *ACS Nano* **2011,** 5, (8), 6339-6348.

Chapter 2

Poly(*tert*-butoxystyrene-*b*-poly(4-vinylpyridine) Diblock Copolymers

Linear poly(4-tert-butoxystyrene)-b-poly(4-vinylpyridine) (PtBOS-b-P4VP) diblock copolymers were synthesized using reversible addition-fragmentation chain transfer (RAFT) polymerization. The stepwise monomer addition to S-dodecyl-S'-(isobutyric acid) trithiocarbonate (DIBTTC) chain-transfer agent resulted in four well-defined diblock copolymers: $tBOS_{62}$-b-$4VP_{28}$, $tBOS_{62}$-b-$4VP_{199}$, $tBOS_{146}$-b-$4VP_{120}$, and $tBOS_{146}$-b-$4VP_{190}$ (subscripts indicate degree of polymerization). The self-assembly of the four different PtBOS-b-P4VP diblock copolymers was studied using SAXS and TEM and a number of interesting observations were made. The $tBOS_{62}$-b-$4VP_{28}$ diblock copolymer with a weight fraction P4VP of 0.21 showed a disordered morphology of P4VP spheres in a liquid-like short-range order despite an estimated value of χN of the order of 50. Increasing the length of the 4VP block to $tBOS_{62}$-b-$4VP_{199}$ gives a diblock copolymer with a weight fraction P4VP of 0.66. It forms a remarkably well-ordered lamellar structure. Likewise the $tBOS_{146}$-b-$4VP_{120}$ diblock copolymer with a weight fraction P4VP of 0.33 forms an extremely well-ordered hexagonal structure of P4VP cylinders. Increasing the P4VP block of this block copolymer to $tBOS_{146}$-b-$4VP_{190}$ with a weight fraction P4VP of 0.44 resulted in a bicontinuous gyroid morphology despite the estimated strong segregation of $\chi N \cong 150$. We discuss these results in terms of the architectural dissimilarity of the two monomers, characterized by the presence of the large side group of PtBOS, and the previously reported value of the interaction parameter, $\chi \cong 0.39$ for this monomer pair.

2.1 Introduction

The synthesis of block copolymers and their ability to form a variety of nanoscale structures via self-assembly has been the subject of extensive research.[1-4] The structures formed depend on the degree of polymerization, N, the block volume fractions, f, and the interaction parameter, χ. For linear diblock copolymers the self-assembled structures include spherical, cylindrical, lamellar and bicontinuous gyroid morphologies.[5, 6] The latter appears in a relatively small range of the copolymer composition in the diblock copolymer phase diagram, mostly in the weak segregation regime ($10 < \chi N < 40$).[7]

Although many of the block copolymers investigated have been synthesized via living anionic polymerization, more often controlled radical polymerization techniques are used to circumvent the disadvantages of anionic polymerizations, e.g., very low temperatures, and complete removal of moisture and oxygen. Furthermore, techniques like atom transfer radical polymerization (ATRP),[8] nitroxide-mediated polymerization (NMP),[9] and reversible addition-fragmentation chain transfer (RAFT) polymerization[10, 11] have a much wider range of compatible monomers. RAFT polymerization is particularly of interest for the synthesis of block copolymers since it has no limitations in temperature and solvents used, can be performed in bulk, emulsion, and solution, and has a broad selection of compatible monomers.[12] There are several advantages to perform RAFT polymerization in solution: the solvent lowers the viscosity of the reaction mixture, in particular at higher conversions, and the initiator can be introduced quantitatively using stock solutions. The latter is very useful since the amount of initiator is often kept very low since each introduced radical leads to an extra terminated polymer chain. These polymers are unwanted byproducts as they do not contain the thiocarbonyl-thio moiety and therefore circumvent further extension using a second monomer to form a block copolymer.

Although investigations involving the synthesis and self-assembly of polystyrene-*b*-poly(4-vinylpyridine) (PS-*b*-P4VP) block copolymers[13] and their supramolecular complexes[14] are available, not much is known about self-assembly of P*t*BOS-*b*-P4VP diblock copolymers. Even though quite a few papers deal with the synthesis of block copolymers containing P*t*BOS,[15-20] many of them convert P*t*BOS to poly(*p*-hydroxystyrene) (P*p*HS) via hydrolysis of the *tert*-butoxy group in order to

utilize the hydrogen-bonding capacities of P*p*HS. In most studies living anionic polymerization[15-17] or NMP[18-20] is employed to synthesize *t*BOS containing block copolymers, only one entry could be discovered in the literature concerning the RAFT polymerization of P*t*BOS homopolymer.[21] Self-assembly of a linear P*t*BOS-*b*-PS-*b*-P4VP triblock copolymers ($f_{t\mathrm{BOS}}$ = 0.29, f_{S} = 0.56, $f_{4\mathrm{VP}}$ = 0.15) results in the formation of core-shell cylindrical self-assembled morphology in which the cylinders are formed by P4VP having a hexagonally shaped PS shell.[22] Microphase separation is expected to be achieved easily in P*t*BOS-*b*-P4VP diblock copolymers since a random copolymer miscibility study showed that the χ-parameter of this combination was determined to be relatively high: $0.39 < \chi_{4VP,t\mathrm{BOS}} < 0.43$.[23] This value is even slightly higher in comparison to the PS-*b*-P4VP system, $0.30 < \chi_{\mathrm{S,4VP}} \leq 0.35$.[24]

In this chapter the synthesis and self-assembly of four linear poly(4-*tert*-butoxystyrene)-*b*-poly(4-vinylpyridine) diblock copolymers (P*t*BOS-*b*_P4VP) via RAFT polymerization in which S-dodecyl-S'-(isobutyric acid) trithiocarbonate (DIBTTC) is used as chain-transfer agent (CTA) will be discussed (Scheme 2.1). After characterization of the molecular weights and compositions, the nanostructures formed via self-assembly of the block copolymers were characterized using transmission electron microscopy (TEM) and small-angle X-ray scattering (SAXS).

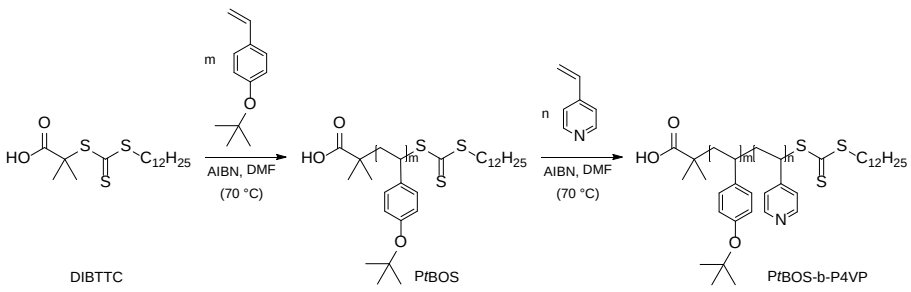

Scheme 2.1 Synthetic pathway for the RAFT polymerization of P*t*BOS and P*t*BOS-*b*-P4VP.

2.2 Experimental

2.2.1 Materials

α,α'-Azobis(isobutyronitrile) (AIBN, Fluka, 98+%) was recrystallized twice from methanol (0.14 g mL^{-1} at maximum 40 °C) at -18 °C, dried in a vacuum desiccator and stored under nitrogen. 4-Vinylpyridine (4VP, Acros, 95%) was stirred over calcium hydride for 24 h and condensed at a high vacuum line (10^{-6} mbar) into a flask containing freshly cut sodium. After stirring overnight at room temperature, it was condensed a second time into an ampule, subjected to three freeze-pump-thaw cycles and stored under nitrogen at -18 °C. 4-*tert*-Butoxystyrene (*t*BOS, Aldrich, 99%) was distilled twice under reduced pressure from finely ground CaH_2, subjected to three freeze-pump-thaw cycles and stored under nitrogen at -18 °C. S-dodecyl-S'-(isobutyric acid) trithiocarbonate (DIBTTC, Aldrich, 98%), toluene (Lab-Scan, 99.5%), *N,N*-dimethylformamide (DMF, Acros, 99.8%, extra dry over Molecular Sieve, AcroSeal), methanol (Lab-Scan, 99.8%), acetone (Lab-Scan, 99.5%), and chloroform ($CHCl_3$, Lab-Scan, 99.5+%) were used as received. 3-Pentadecylphenol (PDP, Aldrich, 98%) was recrystallized twice from petroleum ether.

2.2.2 Synthesis of P*t*BOS homopolymer (macro-CTA)

A typical procedure to prepare a P*t*BOS homopolymer is as follows. To a 50 mL round-bottom flask equipped with a Teflon stirring bar was added DIBTTC (50.8 mg, 0.139 mmol), AIBN (4.1 mg, 0.025 mmol) and 2 mL of DMF. Next *t*BOS (5 mL, 26.6 mmol) was added via a syringe and the flask was connected to a high-vacuum line. Subsequently, the bright yellow solution was subjected to freeze-pump-thaw cycles (10^{-6} mbar) until no more gas release was observed. After backfilling with nitrogen the flask was closed and submerged in a thermostated oil bath at 70 °C. After a reaction time of 43 h the polymerization was stopped by placing the flask in liquid nitrogen. The obtained viscous bright yellow reaction mixture was diluted by adding 3 mL of DMF and subsequently the polymer was precipitated in a 10-fold excess of cold methanol. The yellow solid was isolated via filtration over a pore size 3 glass filter and dried under vacuum overnight at 40 °C. Next, the solid was dissolved in 9 mL of acetone and reprecipitated in a 10-fold excess of cold methanol. The solid was isolated via filtration over a pore size 3 glass filter and dried under vacuum overnight at 40 °C

yielding P*t*BOS as a yellow solid (2.77 g, 59% yield). The product was stored in a vacuum oven at 40 °C until further use. M_n= 25.7 kg mol^{-1}, PDI = 1.09; ^{1}H NMR ($CDCl_3$, 300 MHz): δ = 1.0 - 2.1 (br. m, CH, CH_2 and CH_3), 3.2 (br. s, CH_2 - DIBTTC), 6.2 - 6.8 (br. m, ArH) ppm.

The polymerization reaction of *t*BOS was followed kinetically using the following procedure. To a round-bottom flask equipped with a Teflon stirring bar was added DIBTTC (122.1 mg, 0.335 mmol), AIBN (9.8 mg, 0.060 mmol), *t*BOS (12 mL, 63.7 mmol) and 4.8 mL of DMF. Next, the flask was connected to a high-vacuum line and the bright yellow solution was subjected to freeze-pump-thaw cycles (10^{-6} mbar) until no more gas release was observed. After backfilling the flask with nitrogen, portions of 4.2 mL of the mixture were transferred into four Schlenk tubes equipped with a Teflon stirring bar. All four reactions were started at exactly the same moment by submerging the Schlenk tubes in a oil bath thermostated at 70 °C. The reactions were stopped at 8, 17, 26, and 41 h, respectively, by quenching the reaction mixture in liquid nitrogen. The monomer-to-polymer conversion was determined via ^{1}H NMR spectroscopy by taking the ratio between the peak area of the olefinic protons of the monomer and the peak area of the aliphatic protons of the polymer. The molecular weights and polydispersities were determined by gel permeation chromatography (GPC).

2.2.3 Synthesis of P*t*BOS-*b*-P4VP

For the preparation of P*t*BOS-*b*-P4VP diblock copolymers two trithiocarbonate end-capped P*t*BOS macro-CTA were used: tBOS$_{62}$ (M_n = 11.0 kg mol^{-1}, PDI = 1.09) and tBOS$_{146}$ (M_n = 25.7 kg mol^{-1}, PDI = 1.09) in which the subscripts denote the degrees of polymerization.

A typical procedure to prepare a P*t*BOS-*b*-P4VP diblock copolymer is as follows. To a 50 mL round-bottom flask equipped with a Teflon stirring bar was added the trithiocarbonate end-capped P*t*BOS macro-CTA tBOS$_{146}$ (1.204 g, 0.0468 mmol) described in the previous section and 3.0 mL of DMF. The mixture was stirred until the homopolymer had dissolved completely, resulting in a bright yellow solution. AIBN (0.5 mL of a 3.15 mg mL^{-1} solution in DMF, 0.0096 mmol) and 4VP (1.5 mL, 14.0 mmol) were added to the solution and the flask was connected to a high-vacuum

line. The reaction mixture was subjected to freeze-pump-thaw cycles (10^{-6} mbar) until no more gas release was observed. After backfilling with nitrogen the flask was closed and immersed in a thermostated oil bath at 70 °C. After a reaction time of 20 h the polymerization was stopped by placing the flask in liquid nitrogen. The obtained viscous orange reaction mixture was diluted by adding 4 mL of DMF and subsequently the polymer was precipitated in a 10-fold excess of demineralized water. The precipitate was isolated via filtration over a pore size 3 glass filter and dried under vacuum overnight at 40 °C. Next, the orange solid (1.80 g) was dissolved in 8 mL of DMF and reprecipitated in a 10-fold excess of demineralized water. The product was isolated via filtration over a pore size 3 glass filter and dried under vacuum overnight at 40 °C yielding P*t*BOS-*b*-P4VP as a slightly orange solid (1.71 g, 64% yield). M_n = 38.3 kg mol^{-1}, f_{P4VP} = 0.33, PDI = 1.13; ^{1}H NMR ($CDCl_3$, 300 MHz): δ = 0.8 - 2.2 (br. m, CH, CH_2 and CH_3 - P*t*BOS and P4VP), 3.2 (br. s, CH_2 - DIBTTC), 6.0 - 6.8 (br. m, ArH - P4VP and P*t*BOS), 8.1 - 8.5 (br. m, ArH - P4VP) ppm.

2.2.4 Sample preparation

Films of the P*t*BOS-*b*-P4VP diblock copolymers were prepared according to the following procedure. Ca. 100 mg of each diblock copolymer was dissolved in 7 mL of $CHCl_3$ resulting in 1 wt% solutions. The clear solutions were stirred for at least 1 h at room temperature and subsequently cast in Petri dishes which were then placed into an atmosphere saturated with $CHCl_3$ so that the solvent was allowed to evaporate slowly. After at least one week of solvent annealing, during which all the solvent had evaporated, the Petri dishes were heated for 30 min in an oven at 130 °C.

2.2.5 Characterization

Proton nuclear magnetic resonance (^{1}H NMR) spectra were recorded on a 300 MHz Varian VXR spectrometer at room temperature, using deuterated chloroform ($CDCl_3$) as solvent.

Gel permeation chromatography (GPC) measurements were performed in *N,N*-dimethylformamide with 0.01 M LiBr on a Viscotek GPCMAX equipped with model 302 TDA detectors, using 2 columns (PSS-Gram-1000/30, 10μm, 30 cm). Calibration was performed using narrow disperse polystyrene standards (Polymer

Laboratories). The molecular weights and the polydispersity indices of the homopolymers and the polydispersity index of the block copolymer were determined using universal calibration (UC).

Differential scanning calorimetry was performed using a DSC Q1000 (TA Instruments). The pure polymers were analyzed during a heat/cool/heat cycle in a range between 0 to 180 °C using a heating/cooling rate of 10 °C min^{-1}. The second heating cycle was used to determine the glass transition temperature of the polymers. The glass transition temperatures reported are determined by the inflection point method using Universal Analysis software provided by TA Instruments.

Ultrathin sections (ca. 80 nm) of the prepared block copolymer films embedded in epoxy resin (Epofix, Electron Microscopy Sciences) were obtained using a Leica Ultracut UCT-ultramicrotome at room temperature and placed on copper grids. The microtomed sections were stained using iodine (30 min to 3 h) or ruthenium tetroxide (30 min) to obtain contrast during TEM so that the microphase separation of the diblock copolymer could be observed.

Bright-field transmission electron microscopy (TEM) was performed on a Philips CM12 transmission electron microscope operating at an accelerating voltage of 120 kV. Images were recorded using a Gatan slow-scan CCD camera.

Small-angle X-ray scattering (SAXS) measurements were performed at the Nanomicroscopy Center at the Aalto University using a Bruker Microstar microfocus rotating anode X-ray source with Montel optics (parallel beam, Cu K_α radiation λ = 1.54 Å), where the beam was further collimated using three sets of JJ X-ray 4 blade slits. A sample-to-detector distance of 4.64 m was used. The scattering intensities were measured using a 2D area detector (Bruker HiStar). The samples were measured at room temperature in vacuum.

Additional SAXS measurements were performed at the Dutch-Belgian Beamline (DUBBLE) station BM26B of the European Synchrotron Radiation Facility (ESRF) in Grenoble (France).[25-27] The sample-to-detector distance was ca. 5 m. The wavelength was 1.033 Å. A Dectris-Pilatus 1M detector with a resolution of 981 × 1043 pixels and a pixel size of 172 × 172 μm has been employed to record the 2D-SAXS scattering patterns. Standard corrections for sample absorption and background subtraction have been performed. The data was normalized with respect to the incident beam intensity in order to correct for primary beam intensity fluctuations. The scattering patterns

from silver behenate (AgBh) were used for the detector calibration. The scattering vector q is defined as $q = 4\pi/\lambda \sin \theta$ with 2θ being the scattering angle. The SAXS intensity profiles were acquired at room temperature.

2.3 Results and discussion

2.3.1 Synthesis

2.3.1.1 P*t*BOS homopolymer

The RAFT polymerization of *t*BOS resulted in well-defined P*t*BOS homopolymers with a PDI of 1.09. Table 2.1 lists the details of the polymerization reactions and the properties of the prepared homopolymers. Conversions were determined by ^{1}H NMR spectroscopy and the molecular weights via GPC (universal calibration). The theoretical molecular weights $M_{n,calc}$ were calculated by taking the sum of the molecular weight of DIBTTC precursor and the ratio of [*t*BOS]/[DIBTTC] multiplied by the molar mass of *t*BOS and the conversion. The concentration of the thermal initiator, AIBN, was kept low so that the majority of the polymer chains were initiated by the carboxylic acid containing R-group of the RAFT agent DIBTTC. All the reactions were degassed thoroughly using multiple freeze-pump-thaw cycles on a high-vacuum line to ensure the complete removal of oxygen.

Table 2.1 Ratio of reactants and molecular characteristics of the P*t*BOS homopolymers.

	*t*BOS:AIBN: DIBTTC	V_{DMF} (mL)	Time (h)	Conv [a] (%)	Yield (%)	$M_{n,calc}$ [b] (kg mol^{-1})	M_n [c] (kg mol^{-1})	PDI [c]
*t*BOS$_{62}$	984:1.0:5.5	2	25	31	22	10.1	11.0	1.09
*t*BOS$_{146}$	1064:1.0:5.6	2	43	69	59	23.5	25.7	1.09

[a] Determined by ^{1}H NMR spectroscopy. [b] Calculated using the monomer/initiator ratio, the conversion and the molecular weights of the used monomer and RAFT agent. [c] Determined by GPC (DMF).

2.3.1.2 Kinetics of the synthesis of P*t*BOS by DIBTTC

To investigate whether the RAFT polymerization of *t*BOS using DIBTTC as CTA is proceeding in a controlled manner, the reaction was followed kinetically. A solution of *t*BOS, AIBN, and DIBTTC in 4.8 mL of DMF ([*t*BOS]:[AIBN]:[DIBTTC] = 1056:1.0:5.6 ; [*t*BOS] = 3.8 M) was prepared and subsequently divided into four equal portions. All four polymerizations were started at exactly the same moment by submerging the reaction vessels in a thermostated oil-bath at 70 °C. The polymerizations were stopped at various reaction times by rapidly cooling the respective reaction mixtures using liquid nitrogen. The monomer conversion and the polymer M_n and PDI of the samples stopped at various reaction times were determined. An overview of the results is shown in Table 2.2.

Table 2.2 Reaction time, monomer conversion and molecular characteristics of the PtBOS homopolymers synthesized for the kinetic study.

Entry	t_R (h)	c [a] (%)	$M_{n,calc}$ [b] (kg mol^{-1})	$M_{n,calc}$ [c] (kg mol^{-1})	PDI [c]
1	8	31	10.8	12.5	1.08
2	17	50	17.1	20.8	1.06
3	26	63	21.5	24.5	1.05
4	41	73	24.8	28.8	1.06

[a] Determined by ^{1}H NMR spectroscopy. [b] Calculated using the monomer/initiator ratio, the conversion and the molecular weights of the used monomer and RAFT agent. [c] Determined by GPC (DMF).

The first order kinetic plot, shown in Figure 2.1a, indicates that the number of propagating chains remained constant during the polymerization. Rapid transfer of the growing polymeric chain between the dormant and the free form results in a minimization of termination reactions.[28] The M_n determined by GPC analysis, using DMF as eluent and PS standards for calibration, increased in a linear fashion with monomer conversion and showed a relative good agreement with the corresponding monomer/chain-transfer agent ratio (Figure 2.1b). The difference observed between the experimental and theoretical M_n values can be attributed either to the difference in hydrodynamic volume of the PS used for calibration or to some of the RAFT agent not being active. The polydispersities of the polymers ranged between 1.05 and 1.08. Both

results presented in Figure 2.1 are good indications the RAFT polymerization of *t*BOS is well-controlled.

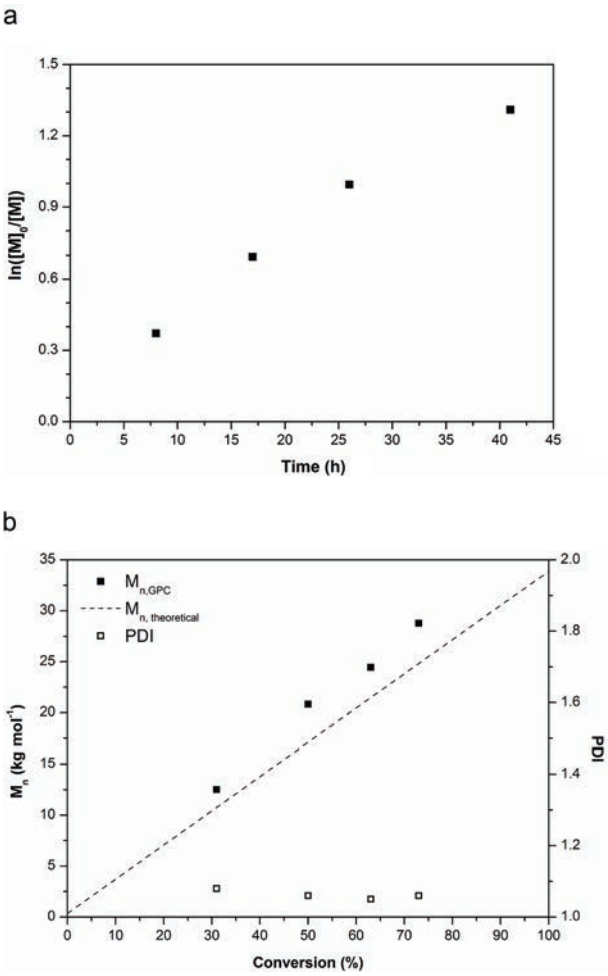

Figure 2.1 Pseudo-first order kinetic plot (a) and number average molecular weight (M_n) and the PDI, both determined by GPC, vs conversion plot (b) for the RAFT polymerization of *t*BOS in DMF at 70 °C using DIBTTC as CTA and AIBN as initiator. [*t*BOS]:[AIBN]:[DIBTTC] = 1056:1.0:5.6. [*t*BOS] = 3.8 M. The calculated M_n is indicated by the dashed line.

2.3.1.3 P4VP-*b*-P*t*BOS diblock copolymer

Four diblock copolymers, *t*BOS$_{62}$-*b*-4VP$_{28}$, *t*BOS$_{62}$-*b*-4VP$_{199}$, *t*BOS$_{146}$-*b*-4VP$_{120}$, and *t*BOS$_{146}$-*b*-4VP$_{190}$, were synthesized by chain extending the two P*t*BOS macro-CTAs, *t*BOS$_{62}$ and *t*BOS$_{146}$ described in section 3.3.1.1, with 4VP in DMF at 70 °C and using AIBN as initiator. The choice to start the polymerization of the block copolymer using tBOS is not arbitrary. The sequence of the monomer addition is very important in order to obtain block copolymers with a narrow polydispersity.[11, 29] Since a homopolymer that contains a trithio moiety is actually a RAFT agent with a very large R-group, the same requirements apply for such a macro-CTA as for small non-polymeric RAFT agents. An important requirement for a macro-CTA is that it should have a high transfer constant to the second monomer otherwise the re-initiation is not instantaneous resulting in higher polydispersities. This implies that the preparation of a diblock copolymer should be started with the least reactive monomer since that means that its radical form is more stable and therefore a better leaving group.

When comparing the polymerization of *t*BOS with 4VP shown in Chapter 5, the latter proves to be faster under the same reaction conditions and therefore the diblock copolymer was started with the polymerization of *t*BOS. Furthermore, there is a more practical reason to start with a P*t*BOS macro-CTA. Because of the highly different solubility of 4VP, *t*BOS, P4VP, and P*t*BOS, it appeared to be very difficult to find a common non-solvent for the precipitation of the diblock copolymers. The only solvent in which both P*t*BOS and P4VP precipitate is water. Because the *t*BOS monomer is not miscible with water, precipitation of a P4VP-*b*-PtBOS block copolymer in water would not result in removal of unreacted *t*BOS monomer. Using 4VP as monomer to extend the P*t*BOS macro-CTA circumvents this problem since it is soluble in water and therefore the P*t*BOS-*b*-P4VP diblock copolymers can be easily isolated.

A variation in the chain length of the P4VP blocks was realized by varying the reaction time or the 4VP concentration or both. Table 2.3 provides an overview of the reaction conditions used. Representative ^{1}H NMR spectra of the *t*BOS$_{146}$ macro-CTA and the *t*BOS$_{146}$-*b*-4VP$_{120}$ are shown in Figure 2.2. Monomer conversions were determined from the ^{1}H NMR spectra of the crude reaction mixtures.

Table 2.3 Ratio of reactants, reaction time, conversion and yield of the P*t*BOS-*b*-P4VP diblock copolymers.

Sample	4VP:AIBN:macro-CTA	V_{DMF} (mL)	Time (h)	Conv[a] (%)	Yield (%)
*t*BOS$_{62}$-*b*-4VP$_{28}$	664:1.0:5.0	4.0	18	25	47
*t*BOS$_{62}$-*b*-4VP$_{199}$	1328:1.0:5.0	3.0	18	74	69
*t*BOS$_{146}$-*b*-4VP$_{120}$	1458:1.0:4.9	3.5	20	48	64
*t*BOS$_{146}$-*b*-4VP$_{190}$	1937:1.0:4.9	3.0	< 20[b]	57	67

[a] Determined by ^{1}H NMR spectroscopy. [b] The exact reaction time is not known due to a heating plate malfunction.

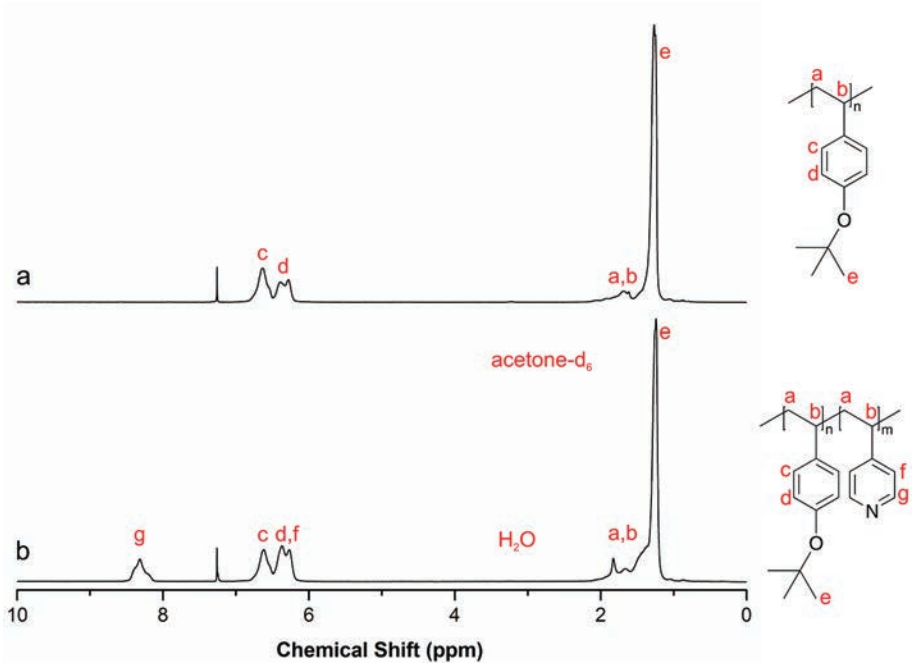

Figure 2.2 ^{1}H NMR spectra of *t*BOS$_{146}$ homopolymer (a) and the *t*BOS$_{146}$-*b*-4VP$_{120}$ diblock copolymer (b) (solvent: $CDCl_3$).

Conversion of the second monomer does not prove that a diblock copolymer is formed since free radical polymerization could occur as well due to the presence of the thermal initiator (AIBN). Gel permeation chromatography (GPC) measurements are therefore essential to prove whether proper chain extension took place. Figure 2.3 displays the

GPC chromatograms of the four P*t*BOS-*b*-P4VP diblock copolymers and the parent P*t*BOS macro-CTAs. The chromatograms depicted all show a unimodal peak which clearly demonstrates the controlled nature of the polymerizations. The curves of the diblock copolymers all show a shift to lower elution volumes because of an increase in the molecular weight proving the successful elongation of both P*t*BOS macro-CTAs. The tailing observed on the higher elution volume side of the GPC traces is caused by the presence of a small amount of deactivated polymer. This is a common observation in RAFT polymerizations since a fraction of the polymer chains is always terminated during the synthesis.[30, 31] The broadening of the curves due to the tailing causes the PDI of the block copolymers to increase to slightly higher values up to 1.17. However, this is still a narrow PDI.

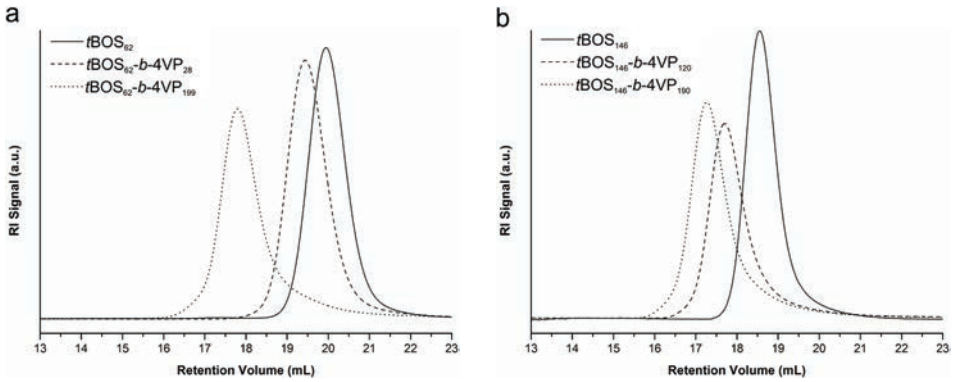

Figure 2.3 GPC chromatograms of tBOS$_{62}$-*b*-4VP$_{28}$, tBOS$_{62}$-*b*-4VP$_{199}$, and the parent macro-CTA tBOS$_{62}$ (a) and of tBOS$_{146}$-*b*-4VP$_{120}$, tBOS$_{146}$-*b*-4VP$_{190}$, and the parent macro-CTA tBOS$_{146}$ (b).

Table 2.4 lists the molecular characteristics of the P*t*BOS-*b*-P4VP diblock copolymers. The calculated molecular weight $M_{n,calc}$ is the sum of the molecular weight of the macro-CTA precursor (GPC) and the ratio of [4VP]/[macro-CTA] multiplied by the molar mass of 4VP and the conversion. The number average molecular weight of the diblock copolymers, M_n, is based on the molecular weight of the macro-CTA precursor and the block weight fractions calculated using the ^{1}H NMR spectrum of the respective diblock copolymer. To calculate the block fractions the peak area of the two aromatic protons of the pyridine ring of P4VP (8.1 - 8.5 ppm) and the peak area of the

four aromatic protons of P*t*BOS (6.2 - 6.8 ppm) are used. The latter value needs to be corrected for the two overlapping aromatic protons of the pyridine ring of P4VP. The values for the molecular weights found via this method are in agreement with the theoretical values based on the monomer conversion. The method is therefore often employed, as the molecular weight determined using GPC ($M_{n,GPC}$) is rarely correct for block copolymers since they often behave distinctly different in solution compared to their homopolymer analogues. This is clear when comparing the M_n and $M_{n,GPC}$ in Table 2.4 in which the latter value is becoming increasingly lower with increasing fraction of P4VP.

Table 2.4 Molecular characteristics of the P*t*BOS-*b*-P4VP diblock copolymers.

Sample	$M_{n,calc}$ [a] (kg mol^{-1})	$M_{n,GPC}$ [b] (kg mol^{-1})	$M_{n,calc}$ [c] (kg mol^{-1})	f_{P4VP} [d]	PDI [b]
*t*BOS$_{62}$-*b*-4VP$_{28}$	14.7	14.0	14.0	0.21	1.08
*t*BOS$_{62}$-*b*-4VP$_{199}$	33.2	28.2	31.9	0.66	1.15
*t*BOS$_{146}$-*b*-4VP$_{120}$	40.8	33.9	38.3	0.33	1.13
*t*BOS$_{146}$-*b*-4VP$_{190}$	49.5	34.3	45.7	0.44	1.17

[a] Calculated using the monomer/macro-CTA ratio, the conversion and the molecular weights of the used monomer and macro-CTA. [b] Determined by GPC (DMF). [c] Calculated using the GPC results of the P*t*BOS macro-CTA and the ratio of integrated intensities of the proton signals in ^{1}H NMR. [d] Calculated using the ratio of integrated intensities of the proton signals in ^{1}H NMR and expressed as weight fraction.

2.3.2 Self-assembly

Films cast from chloroform solutions of the four P*t*BOS-*b*-P4VP diblock copolymers were investigated using SAXS and TEM to study the bulk morphologies. The phase behavior of each diblock copolymer will be discussed separately starting with the two block copolymers based on the *t*BOS$_{62}$ macro-CTA, *t*BOS$_{62}$-*b*-4VP$_{28}$ and *t*BOS$_{62}$-*b*-4VP$_{199}$, followed by the two block copolymers based on the *t*BOS$_{146}$ macro-CTA, *t*BOS$_{146}$-*b*-4VP$_{120}$ and *t*BOS$_{146}$-*b*-4VP$_{190}$, respectively.

2.3.2.1 *t*BOS$_{62}$-*b*-4VP$_{28}$

The diblock copolymer with the lowest degree of polymerization has a composition expressed as weight fraction P4VP of f_{P4VP} = 0.21. To discuss the phase diagram the

composition should be expressed as volume fraction. The specific volume of P4VP is of the order of 0.9 cm^3 g^{-1}.[32] No data for P*t*BOS is known, however, a simple group contribution estimation indicates a slightly larger specific volume.[33] Hence, in terms of volume fractions the composition is only slightly smaller 0.19 – 0.20. For this composition the self-assembled morphology is expected to consist of hexagonally ordered cylinders assuming sufficient segregation. However, the TEM images depicted in Figure 2.4 do not show a well-ordered structure but rather a morphology of spheres in a liquid-like short-range order. Increasing the staining time from 30 min (Figure 2.4a) to 3 h (Figure 2.4b) enhanced the contrast showing the disordered spheres more clearly.

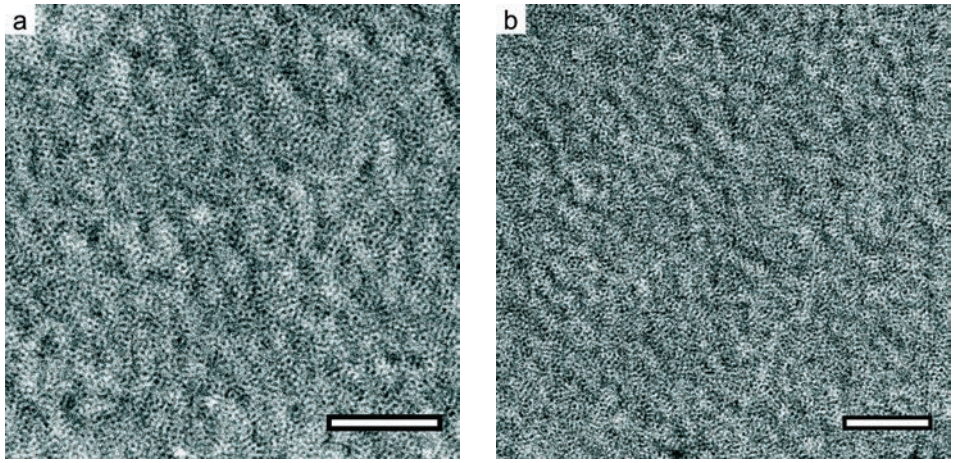

Figure 2.4 Bright-field TEM images of tBOS$_{62}$-*b*-4VP$_{28}$ after staining with iodine for 30 min (a) and 3 h (b). The dark regions correspond to the P4VP domains. Both scale bars represent 200 nm.

That we are dealing with disordered spheres is further corroborated by the absence of higher order peaks in the SAXS intensity profile shown in Figure 2.5. Apparently, the block copolymer is located near the phase boundary of the phase diagram. This result is somewhat surprising since χN of tBOS$_{60}$-*b*-4VP$_{28}$ is expected to be of the order of 55 for $N \cong 140$ (based on segments occupying a volume of 100 cm^3 mol^{-1}) and $\chi = 0.39$.[23] For blocks consisting of geometrically similar monomers, a symmetric phase diagram is predicted theoretically with the transition from the disordered state to

the bcc structure occurring at a composition of ca. 0.1 at this level of segregation, followed by a transition to the cylindrical structure for a volume fraction 0.16. However, in our case both monomers are geometrically quite different and an asymmetric phase diagram may be expected as is ,e.g., the case for PS-*b*-PI diblock copolymers.[6] Theoretically this has been addressed by Milner.[34] The essential geometric difference between P*t*BOS and P4VP is the presence of the *t*-butoxy side group in the former. In comparison with P4VP, P*t*BOS has a much larger side group and this will shift the order-order phase boundaries to higher P4VP volume fractions. In particular, the transition from P4VP spheres to P4VP cylinders will occur at a much larger P4VP volume fraction than the 0.16 predicted for a symmetric copolymer architecture. However, the observation that a disordered morphology is formed at an estimated value of $\chi N \cong 55$ remains quite puzzling and suggests that the literature value of 0.39 may well be too large.

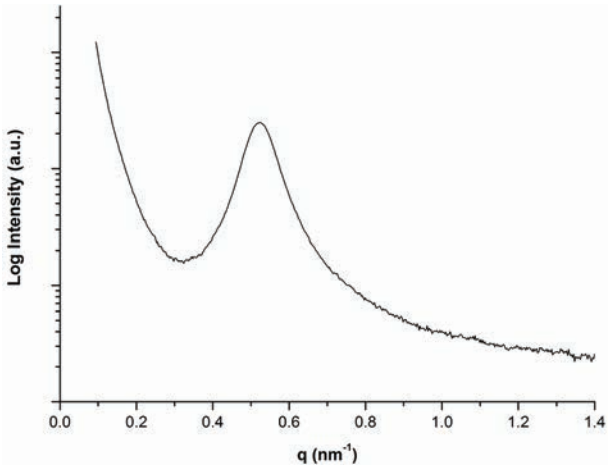

Figure 2.5 SAXS intensity profile of *t*BOS$_{62}$-*b*-4VP$_{28}$.

The *t*BOS$_{62}$-*b*-4VP$_{28}$ block copolymer was analyzed further using DSC and the resulting thermogram is presented in Figure 2.6 together with the thermograms of P4VP and P*t*BOS homopolymers. The thermograms were recorded during the second heating using a heat rate of 10 °C min^{-1}. Only one glass transition is observed for the diblock copolymer at 108 °C.

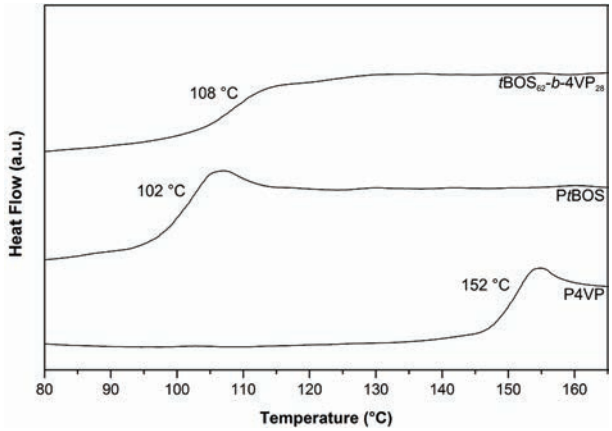

Figure 2.6 DSC thermograms recorded during the second heating at 10 °C min^{-1} of P4VP, P*t*BOS and *t*BOS$_{62}$-*b*-4VP$_{28}$. The corresponding T_g is displayed next to each transition.

Repeating the DSC measurement using a temperature-modulated program with a heating rate of 2 °C min^{-1} and a modulation of 0.50 °C every 60 s, reveals the presence of two maxima as can be seen in the derivative of the reversed heat flow (Figure 2.7). The presence of overlapping T_g's confirms that the diblock copolymer is not homogeneously mixed. The 40 °C reduction of the T_g of the P4VP block compared to the P4VP homopolymer can be explained by the small molecular weight of the P4VP block of 2.94 kg mol^{-1}, which classifies it as an oligomer rather than a true polymer. Similar or even much larger T_g depressions have been observed for ,e.g., poly(α-methyl styrene), where the limiting high molar mass T_g = 173 °C is reduced to T_g = 87 °C for a molar mass of 2.8 kg mol^{-1}.[35] Hence, the values of the two glass transition temperatures do not provide any information about the level of segregation. As far as the T_g's are concerned, the core of the disordered spheres may indeed be nearly pure P4VP as expected from the estimated level of segregation.

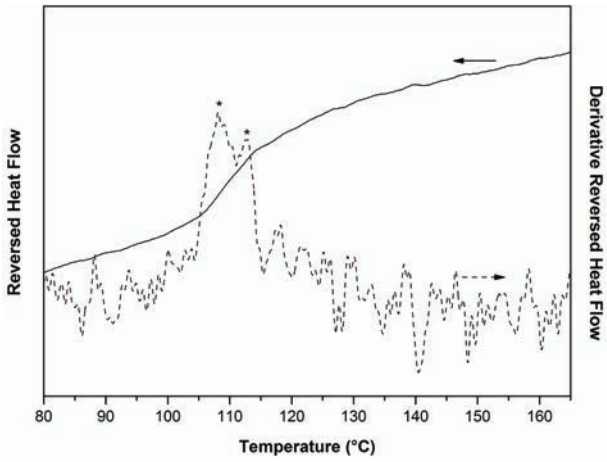

Figure 2.7 DSC thermogram displaying the reversed heat flow (solid line) and the derivative of the reversed heat flow (dotted line) recorded during the second heating at 2 °C min^{-1} modulated with 0.50 °C every 60 s. The two maxima in the derivative of the reversed heat flow (*) indicate the presence of two T_g's at 108 °C and 112 °C, respectively.

2.3.2.2 *t*BOS$_{62}$-*b*-4VP$_{199}$

Increasing the molecular weight for the *t*BOS$_{62}$ macro-CTA based block copolymer to 31.9 kg mol^{-1}, thus increasing the P4VP weight fraction to f_{P4VP} = 0.66, results as expected in a well-ordered lamellar structure of which the TEM images are shown in Figure 2.8. Both images clearly show that the stained P4VP phase is thicker than the P*t*BOS phase, as expected on the basis of the asymmetric block fractions. The lamellar morphology is present in very large domains and the lamellae extend over several microns. The domain spacing of the lamellar structure observed in TEM is found to be around 24 nm.

Figure 2.9 presents the SAXS intensity profile for the *t*BOS$_{62}$-*b*-4VP$_{199}$ diblock copolymer. The scattering peaks are in the ratio 1:2:3:4:5 as expected for a lamellar morphology and all 5 scattering peaks in the q-range investigated are indeed present confirming the well-ordered nature of the lamellar morphology. From the value of the first order peak, q = 0.256 nm^{-1}, the characteristic domain spacing D is calculated to be 25 nm in good agreement with the value found from TEM.

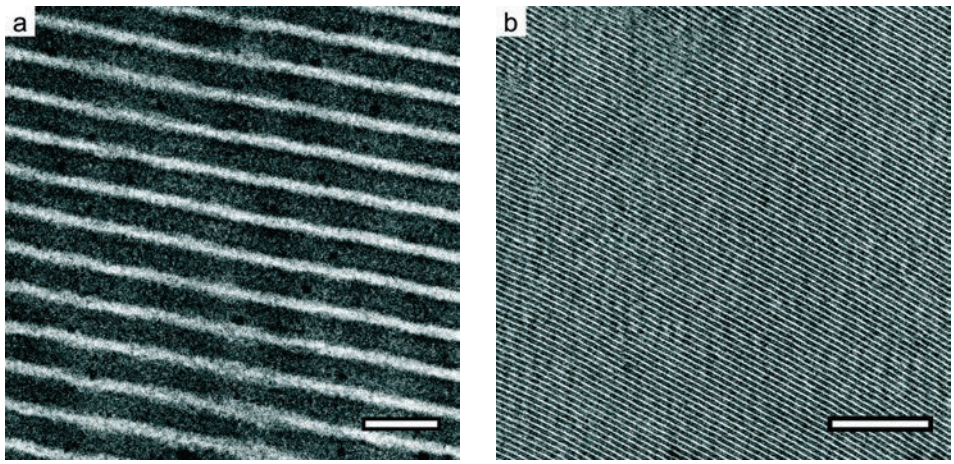

Figure 2.8 Bright-field TEM images of iodine stained samples of *t*BOS$_{62}$-*b*-4VP$_{199}$ block copolymer. The dark regions correspond to the P4VP domains. The scale bars represent 50 nm (a) and 400 nm (b), respectively.

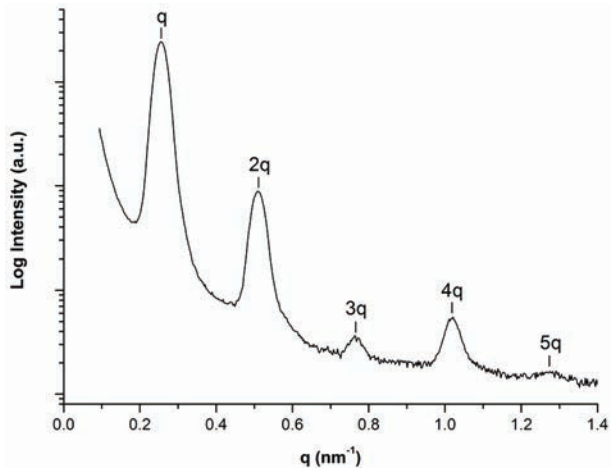

Figure 2.9 SAXS intensity profile at room temperature of the *t*BOS$_{62}$-*b*-4VP$_{199}$ diblock copolymer.

2.3.2.3 *t*BOS$_{146}$-*b*-4VP$_{120}$

The first P*t*BOS-*b*-P4VP diblock copolymer based on the *t*BOS$_{146}$ macro-CTA has a molecular weight of 38.3 kg mol^{-1} and a f_{P4VP} of 0.33. The TEM images of this block

copolymer presented in Figure 2.10 show the expected hexagonally ordered cylinders. Large domains are observed in which the cylinders are formed by the P4VP minority phase, appearing dark due to iodine staining, surrounded by a P*t*BOS matrix. The distance between the cylinder planes is determined to be 25 nm.

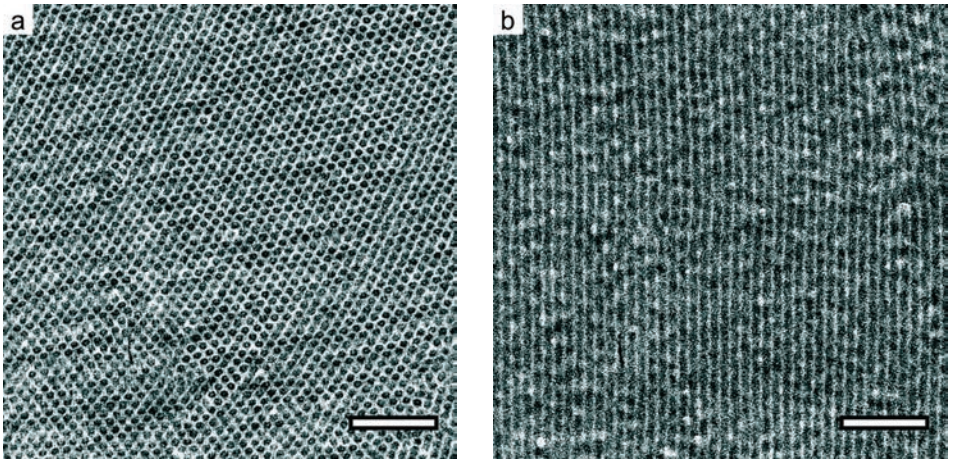

Figure 2.10 Bright-field TEM images showing (a) the cross section perpendicular to the cylinder axis and (b) the cross section parallel to the cylinder axis for iodine stained samples of tBOS$_{146}$-*b*-4VP$_{120}$ block copolymer. The dark regions correspond to the P4VP domains. Both scale bars represent 200 nm.

Figure 2.11 presents the SAXS intensity profile for the diblock copolymer. The scattering peaks observed are in the ratio 1:√4:√7:√9:√13, which is characteristic for a hexagonally packed cylindrical structure. From the value of the first order peak, q = 0.211 nm^{-1}, the characteristic domain spacing D is calculated to be 30 nm, which is somewhat larger as found from TEM.

For the TEM analysis of the block copolymer some samples were also stained using RuO_4 instead of iodine. Although the hexagonally packed cylinder morphology was observed, it is interesting to note that some areas contained a somewhat different morphology as can be seen in Figure 2.12. Probably it is a frozen in transition state and therefore a non-equilibrium morphology.

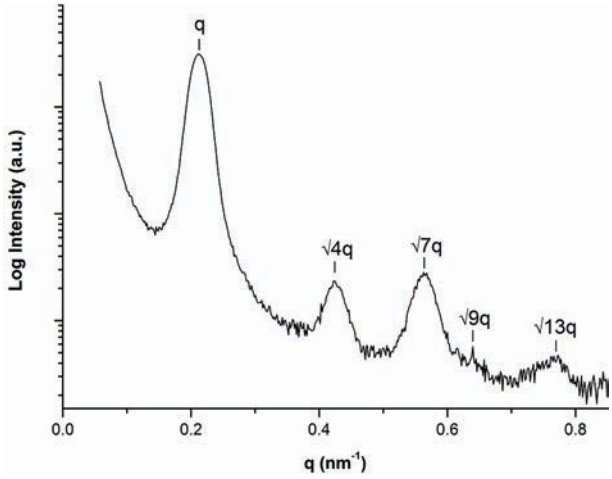

Figure 2.11 SAXS intensity profile at room temperature of *t*BOS$_{146}$-*b*-4VP$_{120}$.

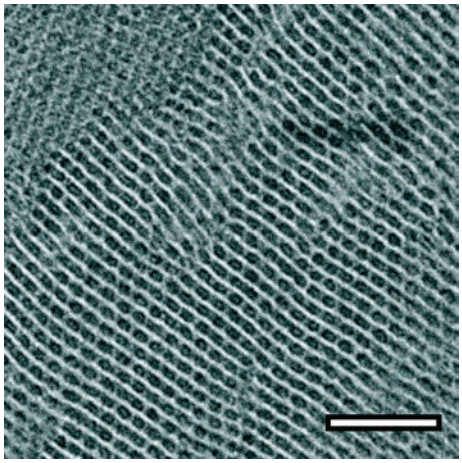

Figure 2.12 Bright-field TEM image showing a non-equilibrium morphology for the *t*BOS$_{146}$-*b*-4VP$_{120}$ blockcopolymer in which the dark areas correspond to the P4VP domains. The scale bar represents 200 nm.

2.3.2.4 *t*BOS$_{146}$-*b*-4VP$_{190}$

Further increase of the P4VP fraction resulted in a block copolymer with a molecular weight of 45.7 kg mol^{-1} and a f_{P4VP} of 0.44. Since the polymer composition is almost symmetric a lamellar morphology was expected. However, the electron micrographs presented in Figure 2.13 show that the self-assembled morphology is not a lamellar one but a bicontinuos gyroid morphology. Figures 2.13b and 2.13c show the TEM images of a sample stained with ruthenium tetroxide in which a different plane of the gyroid morphology can be observed.

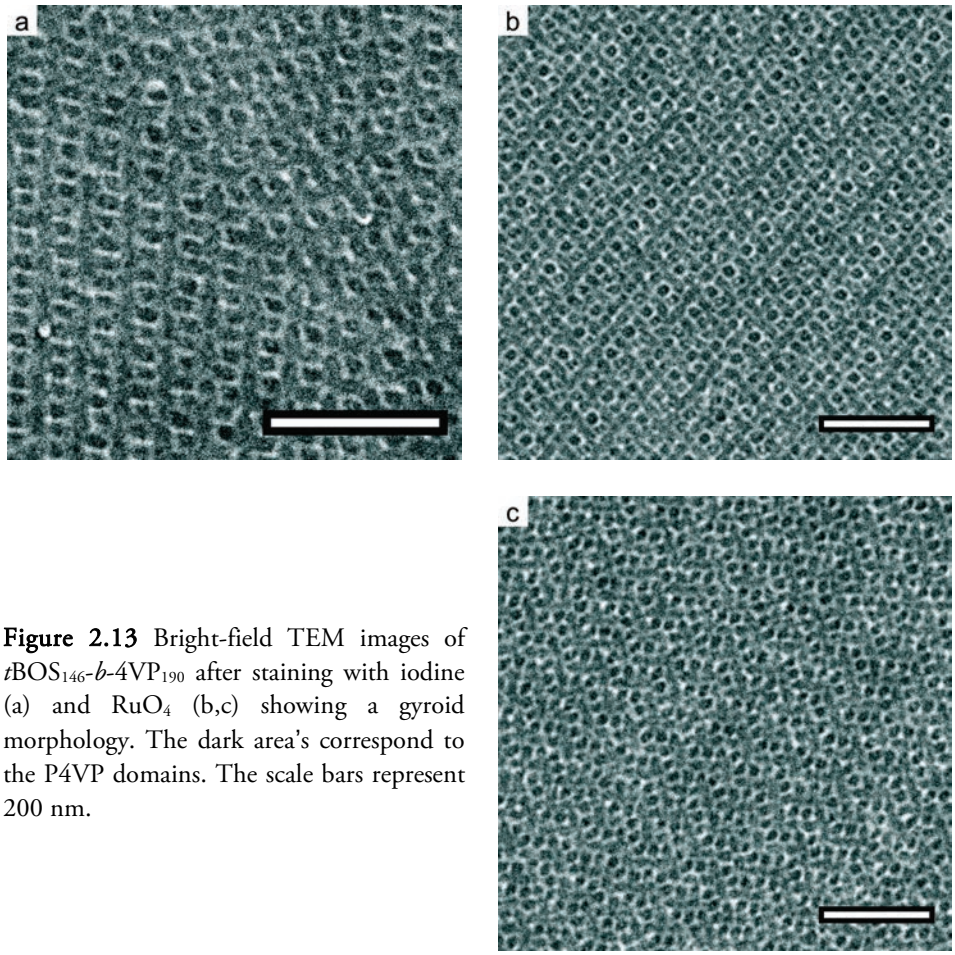

Figure 2.13 Bright-field TEM images of *t*BOS$_{146}$-*b*-4VP$_{190}$ after staining with iodine (a) and RuO_4 (b,c) showing a gyroid morphology. The dark area's correspond to the P4VP domains. The scale bars represent 200 nm.

To further prove the presence of the gyroid morphology observed in TEM, SAXS measurements were performed and the result is presented in Figure 2.14. The scattering peaks are found at a positions √6:√8:√14:√22: √50 as is characteristic for a gyroid morphology. The additional peak found at √2 suggests that the gyroid structure is slightly distorted.

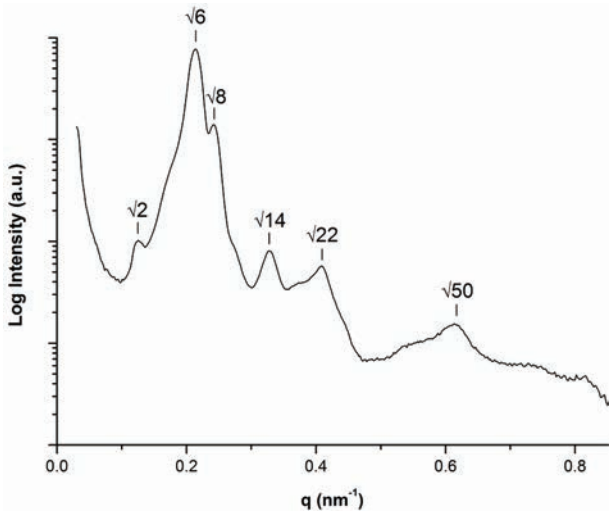

Figure 2.14 SAXS intensity profile at room temperature of *t*BOS$_{146}$-*b*-4VP$_{190}$.

Usually, the formation of a gyroid structure occurs in the intermediate to weak segregation regime and with volume fractions of the majority phase of 0.59-0.69.[36-38] However, as discussed before, we are dealing with two blocks consisting of geometrically quite different monomers where the order-order transitions shift to higher P4VP volume fractions. In this respect, the occurrence of the gyroid structure is not a big surprise. Still the gyroid structure came as a surprise given the strong segregation, $\chi N > 150$, estimated on the basis of the literature value $\chi \cong 0.39$. Still, this is not the first time the gyroid morphology has been observed in the strong segregation limit. Recently it was observed experimentally also in the strong segregation regime ($\chi N = 120$) for difluorocarbene-modified polyisoprene-*block*-poly(ethylethylene) diblock copolymers of relatively low molecular weight in which equilibration is not a crucial issue.[39] A subsequent theoretical self-consistent field

analysis demonstrated that the original conclusion of a disappearing gyroid region at higher segregations may not be correct and if it occurs, it will happen at much larger segregations than previously predicted.[7] Hence, the presence of a gyroid structure at strong segregation can no longer be excluded and our P*t*BOS-*b*-P4VP diblock copolymer could be another example. This is not without interest because the gyroid morphology is interesting for several applications that require bicontinuous morphologies with well-defined sharp phase boundaries. However, as remarked before and discussed briefly in the Conclusion, it can also not be excluded that the literature value $\chi \cong 0.39$ is too large.

2.4 Conclusion

The RAFT polymerization of *t*BOS resulted in two well-defined P*t*BOS homopolymers with a PDI of 1.09. The kinetic study of the RAFT polymerization of *t*BOS showed that the reaction is well-controlled since the number of propagating chains remained constant during the polymerization. Furthermore, the M_n increased in a linear fashion with monomer conversion while the polydispersities of the polymers ranged between 1.05 and 1.08.

Linear P*t*BOS-*b*-P4VP diblock copolymers were synthesized via chain extension of the two P*t*BOS-macroCTA's resulting in four diblock copolymers polymers: $t\text{BOS}_{62}$-*b*-4VP_{28}, $t\text{BOS}_{62}$-*b*-4VP_{199}, $t\text{BOS}_{146}$-*b*-4VP_{120}, and $t\text{BOS}_{146}$-*b*-4VP_{190} (subscripts indicate degree of polymerization).

The self-assembly of four different P*t*BOS-*b*-P4VP diblock copolymers was studied using SAXS and TEM and a number of interesting observations were made. The $t\text{BOS}_{62}$-*b*-4VP_{28} diblock copolymer with a weight fraction P4VP of 0.21 showed a disordered morphology of P4VP spheres in a liquid-like short-range order. Based on a previously reported value for the interaction parameter, $\chi \cong 0.39$, the estimated value of χN, where N is the number of segments occupying a volume of 100 cm^3 mol^{-1}, exceeds 50. For this level of segregation an ordered morphology is expected, which based on the architectural asymmetry of both monomers could well be spherical. The interaction parameter for this monomer pair was determined by a random copolymer blend study. This study showed very clearly that $\chi > 0.17$. The value of 0.39, however, is based on a single annealing experiment that suggested that macro phase separation occurred in a blend of a P($t\text{BOS}_{0.91}$-*co*-$4\text{VP}_{0.09}$) random copolymer (subsrcipt indicates weight fraction) of M_w = 61.7 kg mol^{-1} and a P*t*BOS homopolymer of M_w = 71.9 kg mol^{-1}, whereas the same random copolymer was miscible with P*t*BOS of M_w 59.9 kg mol^{-1}. Triggered by the self-assembly observed in the P*t*BOS-*b*-P4VP diblock copolymers studied we took a closer look at the results of the annealing experiments of the random copolymer blends and concluded that at this point we cannot fully exclude that the literature value of the interaction parameter is too large. Increasing the length of the 4VP block to $t\text{BOS}_{62}$-*b*-4VP_{199} results in a diblock copolymer with a weight fraction P4VP of 0.66. It forms a remarkably well-ordered lamellar structure. Likewise the $t\text{BOS}_{146}$-*b*-4VP_{120} diblock copolymer with a weight

fraction P4VP of 0.33 forms an extremely well-ordered hexagonal structure of P4VP cylinders. In both cases TEM shows large single crystal-like regions, which is further confirmed by SAXS patterns with several sharp diffraction peaks. Increasing the P4VP block of the latter block copolymer to *t*BOS$_{146}$-*b*-4VP$_{190}$ results in a weight fraction P4VP of 0.44. Surprisingly a bicontinuous gyroid morphology is observed despite the estimated strong segregation of $\chi N \cong 150$. Although the presence of the gyroid morphology at strong segregations has been observed before and this possibility has been theoretically confirmed, it remains a fact that is mainly observed at weak to intermediate segregations. This is yet another observation that suggests that the literature value of the interaction parameter may well be too large.

2.5 References

1. Bates, F. S.; Fredrickson, G. H. *Annu. Rev. Phys. Chem.* **1990,** 41, 525-557.
2. Muthukumar, M.; Ober, C. K.; Thomas, E. L. *Science* **1997,** 277, (5330), 1225-1232.
3. Park, C.; Yoon, J.; Thomas, E. L. *Polymer* **2003,** 44, (22), 6725-6760.
4. Abetz, V.; Simon, P. F. W., *Phase Behaviour and Morphologies of Block Copolymers*. Springer-Verlag Berlin: Berlin, 2005; Vol. 189, p 125-212.
5. Matsen, M. W.; Schick, M. *Phys. Rev. Lett.* **1994,** 72, (16), 2660-2663.
6. Khandpur, A. K.; Forster, S.; Bates, F. S.; Hamley, I. W.; Ryan, A. J.; Bras, W.; Almdal, K.; Mortensen, K. *Macromolecules* **1995,** 28, (26), 8796-8806.
7. Cochran, E. W.; Garcia-Cervera, C. J.; Fredrickson, G. H. *Macromolecules* **2006,** 39, (7), 2449-2451.
8. Matyjaszewski, K.; Xia, J. H. *Chem. Rev.* **2001,** 101, (9), 2921-2990.
9. Hawker, C. J.; Bosman, A. W.; Harth, E. *Chem. Rev.* **2001,** 101, (12), 3661-3688.
10. Chiefari, J.; Chong, Y. K.; Ercole, F.; Krstina, J.; Jeffery, J.; Le, T. P. T.; Mayadunne, R. T. A.; Meijs, G. F.; Moad, C. L.; Moad, G.; Rizzardo, E.; Thang, S. H. *Macromolecules* **1998,** 31, (16), 5559-5562.
11. Moad, G.; Rizzardo, E.; Thang, S. H. *Polymer* **2008,** 49, (5), 1079-1131.
12. Moad, G.; Rizzardo, E.; Thang, S. H. *Aust. J. Chem.* **2005,** 58, (6), 379-410.
13. Zamfir, M.; Patrickios, C. S.; Montagne, F.; Abetz, C.; Abetz, V.; Oss-Ronen, L.; Talmon, Y. *J. Polym. Sci. Pol. Chem.* **2012,** 50, (8), 1636-1644.
14. Vukovic, I.; ten Brinke, G.; Loos, K. *Macromolecules* **2012,** 45, (23), 9409-9418.
15. Tung, P. H.; Kuo, S. W.; Chen, S. C.; Lin, C. L.; Chang, F. C. *Polymer* **2007,** 48, (11), 3192-3200.
16. Rahman, S. S. A.; Kawaguchi, D.; Matsushita, Y. *Polymer* **2011,** 52, (1), 164-171.
17. Asari, T.; Matsuo, S.; Takano, A.; Matsushita, Y. *Polym. J.* **2006,** 38, (3), 258-263.
18. Higaki, Y.; Otsuka, H.; Takahara, A. *Polymer* **2003,** 44, (23), 7095-7101.
19. Yoshida, E.; Ema, T. *Colloid Polym. Sci.* **2011,** 289, (8), 919-923.
20. Ohno, K.; Ejaz, M.; Fukuda, T.; Miyamoto, T.; Shimizu, Y. *Macromol. Chem. Phys.* **1998,** 199, (2), 291-297.
21. Lei, Y.; Lodge, T. P. *Soft Matter* **2012,** 8, (7), 2110-2120.
22. du Sart, G. G.; Vukovic, I.; van Ekenstein, G. A.; Polushkin, E.; Loos, K.; ten Brinke, G. *Macromolecules* **2010,** 43, (6), 2970-2980.

23. du Sart, G. G. Supramolecular Triblock Copolymer Complexes. PhD Thesis, University of Groningen, 2009.
24. Alberda van Ekenstein, G. O. R.; Meyboom, R.; ten Brinke, G.; Ikkala, O. *Macromolecules* **2000,** 33, (10), 3752-3756.
25. Borsboom, M.; Bras, W.; Cerjak, I.; Detollenaere, D.; van Loon, D. G.; Goedtkindt, P.; Konijnenburg, M.; Lassing, P.; Levine, Y. K.; Munneke, B.; Oversluizen, M.; van Tol, R.; Vlieg, E. *J. Synchrot. Radiat.* **1998,** 5, 518-520.
26. Bras, W.; Dolbnya, I. P.; Detollenaere, D.; van Tol, R.; Malfois, M.; Greaves, G. N.; Ryan, A. J.; Heeley, E. *J. Appl. Crystallogr.* **2003,** 36, 791-794.
27. Nikitenko, S.; Beale, A. M.; van der Eerden, A. M. J.; Jacques, S. D. M.; Leynaud, O.; O'Brien, M. G.; Detollenaere, D.; Kaptein, R.; Weckhuysen, B. M.; Bras, W. *J. Synchrot. Radiat.* **2008,** 15, 632-640.
28. Lowe, A. B.; McCormick, C. L. *Prog. Polym. Sci.* **2007,** 32, (3), 283-351.
29. Perrier, S.; Takolpuckdee, P. *J. Polym. Sci. Pol. Chem.* **2005,** 43, (22), 5347-5393.
30. Goto, A.; Sato, K.; Tsujii, Y.; Fukuda, T.; Moad, G.; Rizzardo, E.; Thang, S. H. *Macromolecules* **2001,** 34, (3), 402-408.
31. Wong, K. H.; Davis, T. P.; Bamer-Kowollik, C.; Stenzel, M. H. *Polymer* **2007,** 48, (17), 4950-4965.
32. Zha, W. B.; Han, C. D.; Lee, D. H.; Han, S. H.; Kim, J. K.; Kang, J. H.; Park, C. *Macromolecules* **2007,** 40, (6), 2109-2119.
33. van Krevelen, D. W., *Properties of Polymers*. 3rd ed.; Elsevier Science Publishers, Amsterdam, Oxford, New York: 1990.
34. Milner, S. T. *Macromolecules* **1994,** 27, (8), 2333-2335.
35. Cowie, J. M. G.; Toporows.Pm. *Eur. Polym. J.* **1968,** 4, (5), 621-&.
36. Vukovic, I.; Punzhin, S.; Vukovic, Z.; Onck, P.; De Hosson, J. T. M.; ten Brinke, G.; Loos, K. *ACS Nano* **2011,** 5, (8), 6339-6348.
37. Hwanga, J. Y.; Huh, J.; Jung, B.; Hong, J. M.; Park, M.; Park, C. *Polymer* **2005,** 46, (21), 9133-9143.
38. Gwyther, J.; Lotze, G.; Hamley, I.; Manners, I. *Macromol. Chem. Phys.* **2011,** 212, (2), 198-201.
39. Davidock, D. A.; Hillmyer, M. A.; Lodge, T. P. *Macromolecules* **2003,** 36, (13), 4682-4685.

Chapter 3

Two-length-scale A-*b*-(B-*b*-A)$_n$-*b*-B Multiblock Copolymers

A-b-(B-b-A)$_n$-b-B multiblock copolymers composed of short middle diblock units (B-b-A)$_n$ and two long A- and B-outer blocks were successfully prepared. The multiblock copolymers consist of polystyrene (S) and poly(p-hydroxystyrene) (pHS) and were prepared through sequential anionic polymerization of styrene and 4-tert-butoxystyrene, followed by hydrolysis of the tert-butoxy group. A hexa- and an octablock copolymer with a low overall polydispersity were synthesized. The self-assembled structures were investigated using small-angle X-ray scattering (SAXS) and transmission electron microscopy (TEM). Because of the smaller number of inner blocks and their relatively small molar mass, a single periodic lamellar morphology was observed for the hexablock copolymer while, a lamellar-in-lamellar morphology with two thin layers within successive thick layers was observed for the octablock copolymer with larger middle diblock units. These observations are in excellent agreement with existing theories.

Parts of this chapter were published in: *Soft Matter* **2012,** 8, (16), 4479-4485.

3.1 Introduction

Driven by the prospects to develop nanotechnology applications, the ability of block copolymer systems to form highly ordered complex nanostructures has been in the focus of scientific attention for many years.[1-12] The self-assembly of diblock copolymers is well understood by now,[5, 6] although new developments still occur.[7, 8] Gradually, the research shifts to the study of self-assembly in copolymers with a more complex molecular architecture, such as triblock copolymers and star copolymers.[13-16] In comparison to diblock copolymers, the addition of a third block, in the case of ABC triblock copolymers, gives rise to many more morphologies. In particular, the order in which the linkage occurs is an additional parameter leading to different levels of frustration and thus strongly influencing the phase morphology.[13, 14] For ABC star terpolymers the spring of three different polymers from a single junction point is the determining factor that may result in typical two dimensional Archimedean tiling patterns, where these junction points are located on straight lines.[16]

Another development in complexity involves binary multiblock copolymers with two different intrinsic length scales.[17-21] A number of theoretical studies appeared dealing with the intricacies of the self-assembly in specific representatives of such systems, e.g., AB multiblock copolymers involving end blocks that differ in length from the blocks of the middle multiblock.[22-30] Despite the fact that only two chemically different species are involved, the presence of two different intrinsic length scales may result in hierarchical structure formation. Such a "structure-in-structure" morphology was first reported for supramolecules consisting of poly(styrene-*b*-4-vinylpyridine) diblock copolymers with relatively short side chains (pentadecyl phenol) hydrogen-bonded to the pyridine blocks.[31, 32] The molecular architecture of these supramolecules resembles that of A-*b*-(B-*graft*-C) block copolymers. It is characterized by two intrinsic length scales, that of the whole molecule and that of the repeat unit of the graft block. In the case of lamellar-in-lamellar structures, the graftlike architecture is also responsible for both lamellar structures being oriented perpendicularly with respect to each other.

An alternative way to obtain a similar two-length-scale molecular architecture consists of linear multiblock copolymers, such as C-*b*-(A-*b*-B)$_n$-*b*-C, where the middle multiblock consists of several diblocks that are much shorter than the two end blocks. Matsushita and co-workers showed the presence of a lamellar-in-lamellar morphology

in $P(IS)_4IP$ undecablock copolymers (P = poly(2-vinylpyridine), I = polyisoprene, S = polystyrene).[17]

The presence of structures at two different length scales for ternary multiblock copolymers with two intrinsic length scales does not come as a surprise. For binary multiblock copolymers this is less obvious. A Random Phase Approximation (RPA) analysis of different representatives of this class of systems revealed a very interesting double maxima behavior of the scattering function.[22] The theoretically best studied system involves the fully symmetric $A_{mN/2}$-$(B_{N/2}$-$A_{N/2})_n$-$B_{mN/2}$ multiblock copolymer. Here m denotes the relative length of both outer blocks with respect to the length $N/2$ of the blocks of the symmetric diblocks that make up the middle multiblock and n denotes number of diblocks of middle multiblock. In the weak segregation limit the behavior of the symmetric $A_{mN/2}$-$(B_{N/2}$-$A_{N/2})_n$-$B_{mN/2}$ multiblock copolymers resembles that of a symmetric ABC triblock copolymers with a non-selective middle B-block. For the multiblock, the middle $(B_{N/2}$-$A_{N/2})_n$ multiblock plays the role of the non-selective B-block in case of the ABC triblock copolymer. There are obviously subtle differences due to the difference in molecular architecture. In particular for systems near the equimaximum of the two scattering peaks, two-length-scale body-centered tetragonal mesophases become stable.[25, 26] If for a given n the end blocks are sufficiently long (m sufficiently large) first a lamellar structure will be formed due to the segregation between the two end blocks. If the segregation is further increased the relatively short diblocks of the middle multiblock will also segregate and may form "thin" lamellae inside the thicker lamellae formed by the end blocks. The presence and the number of "thin" internal layers depend on the segregation and on the number and relative length of the internal diblocks n.[29] Furthermore, on the formation of the internal layers the overall long period will increase or decrease depending on the number of diblocks n and the commensurability of the two length scales involved (i.e., m).[30]

So far the only experimental realization of this class of polymers, albeit a not fully symmetric system, was presented by Matsushita and co-workers,[18] who showed that a S-ISISISISI-S undecablock copolymer with two long polystyrene (S) end blocks and a middle multiblock consisting of short polystyrene and isoprene (I) blocks self-assembled in a lamellar-in-lamellar morphology with three successive thin I, S and I layers inside two thick S layers.

To verify the intriguing phase behavior predicted, it is of great interest to develop additional experimental model systems. To be useful, the design has to satisfy two important requirements. First of all, the value of the Flory-Huggins parameter between the two different monomers has to be large enough to preferably already induce microphase separation for diblocks of a relatively small molar mass in the order of 10,000 g·mol^{-1} or less. This will allow us to use for the middle multiblock relatively short diblocks. For the above mentioned S-ISISISISI-S multiblock copolymer of styrene and isoprene the interaction parameter value is actually somewhat smaller, $\chi_{IS} \cong 0.05$[33] (of course it is temperature dependent) and the IS diblocks used had a considerably larger molar mass of ca. 28,000 g mol^{-1}. Additionally, the multiblock copolymer should preferably be as narrow in polydispersity as possible to avoid polydispersity effects.

A combination of monomers that satisfies these requirements is styrene and *p*-hydroxystyrene. Poly(*p*-hydroxystyrene) (*p*HS) and its derivatives are of interest for, e.g., applications in photoresist materials,[34-37] removal of organic material from aqueous waste via adsorption,[38] and as light-emitting devices.[39, 40] In order to effectively polymerize *p*-hydroxystyrene, the acidic proton needs to be protected. Different kinds of protecting groups like *tert*-butyl,[41, 42] various alkylsilyl,[43-45] and *tert*-butoxycarbonyl[43] are used. The protecting groups can be easily removed via acidic cleavage. Subsequently, post-polymerization modifications of the polymer via a reaction with the phenolic group are possible.[44] Protected *p*-hydroxystyrene has been polymerized via different polymerization methods like free radical polymerization,[42, 43] nitroxide mediated polymerization,[46] cationic polymerization,[42] and anionic polymerization[41, 42, 44, 45] and combined with different comonomers like styrene,[41, 45, 47] 4-vinylpyridine,[47, 48] 4-*tert*-butylstyrene,[49, 50] and ethylene oxide[51] in both random copolymers and block copolymers. In order to obtain (multi)block copolymers with a narrow polydispersity, anionic polymerization is indicated.[18, 52-54] Anionic polymerization of diblock copolymers of styrene and 4-*tert*-butoxystyrene have been synthesized starting both from styrene[55] as from 4-*tert*-butoxystyrene.[56] This indicates that the stability of the anion is relatively the same and sequential anionic polymerization is possible. Finally, the interaction parameter between both species is expected to be quite large. The only value available in the literature is $\chi_{S,pHS} \cong 0.68$.[56] However, this value is based on a

solubility parameter estimation and should merely be considered as an order of magnitude.

In this chapter the preparation of two-length-scale symmetric multiblock copolymers of *p*HS and S is presented and the self-assembly of the hexablock and octablock copolymer is discussed. The latter A-*b*-(B-*b*-A)$_3$-*b*-B consists of six short inner blocks and two long outer blocks. Because of the symmetry its self-assembled structure will be lamellar with possibly 0, 2, 4 or 6 "thin" internal layers (Figure 3.1a). In contrast, the lamellar state of the corresponding A-*b*-(B-*b*-A)$_3$-*b*-B-*b*-A, with two chemically identical long A end blocks resembling the system studied experimentally by Matsushita and co-workers[18] and theoretically in our group,[29] will have 1, 3, 5 or 7 "thin" internal layers (Figure 3.1b).

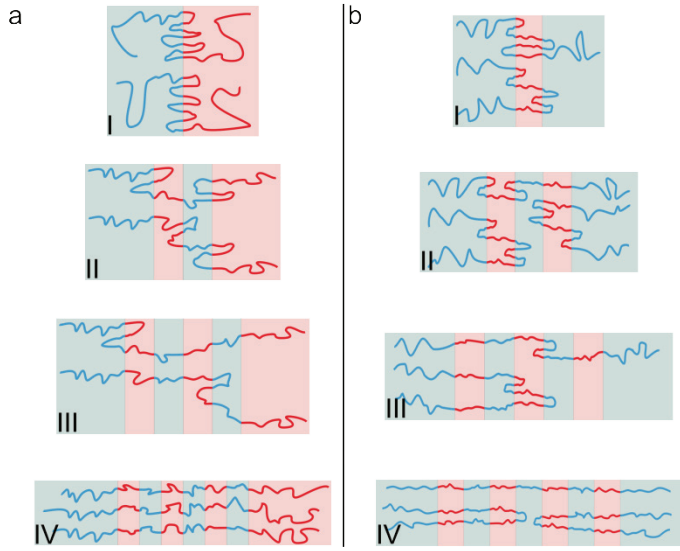

Figure 3.1 Possible lamellar self-assembled structures with (a) 0, 2, 4 and 6 thin internal layers respectively for a symmetric A-*b*-(B-*b*-A)$_3$-*b*-B octablock copolymer consisting of six short inner blocks and two long outer blocks and with (b) 1, 3, 5 and 7 thin inner layers respectively for an asymmetric A-*b*-(B-*b*-A)$_3$-*b*-B-*b*-A nonablock copolymer.

3.2 Experimental

3.2.1 Materials

Styrene (S, Acros, 99%) was dried overnight under nitrogen atmosphere over finely ground CaH_2 and condensed at room temperature (10^{-6} mbar) into a flask containing dibutyl magnesium. After stirring overnight, a second condensation into a storage ampule was performed. The purified styrene was stored at -18 °C under nitrogen atmosphere. 4-*tert*-butoxystyrene (*t*BOS, Aldrich, 99%) was distilled twice under reduced pressure from finely ground CaH_2 and stored under nitrogen at -18 °C. *sec*-Butyllithium (*s*-BuLi, Acros, 1.3 M solution in cyclohexane/hexane (92/8)) was used without further purification. Tetrahydrofuran (THF, Acros, 99.9%) was reacted with *tert*-butyllithium for 1 h at -78 °C under nitrogen atmosphere during which a yellow color indicated that the solvent was suitable for anionic polymerization. It was condensed at room temperature into the polymerization flask and subjected to three freeze-pump-thaw cycles. Methanol (MeOH, Lab-Scan, 99.8%) was degassed by nitrogen gas flow for 1h at room temperature. 1,4-Dioxane (Acros, 99+%), hydrochloric acid (HCl, Merck, 37%) and osmium(VII)-tetroxide (OsO_4, Acros, 99.9+%) were used as received.

3.2.2 Sequential anionic polymerization of S-*b*-(*t*BOS-*b*-S)$_n$-*b*-*t*BOS

S-*b*-(*t*BOS-*b*-S)$_n$-*b*-*t*BOS multiblock copolymers composed of multiple short inner diblocks and two long end blocks were synthesized through a multi-step sequential anionic polymerization in THF at -78 °C using *s*-BuLi as initiator; the synthesis is presented in Scheme 1. All anionic polymerizations were performed under nitrogen atmosphere in a round-bottomed flask attached to a high-vacuum line. Solvent was condensed into the reaction vessel. Initiator and monomers were transferred to the reaction vessel via a degassed stainless steel needle and syringe.

At room temperature 500 mL of THF was condensed into a 1000 mL flask and after three freeze-pump-thaw cycles the THF was titrated with *s*-BuLi until the solution turned slightly yellow. The solution was cooled down to -78 °C and the calculated amount of styrene was added, followed by the calculated amount of *sec*-BuLi to initiate the polymerization; a bright yellow-orange color appeared. After 30 min of reaction time an aliquot of the polystyrene was isolated for analysis by dispersing the sample in

degassed methanol. Subsequently, the calculated amount of 4-*tert*-butoxystyrene was added and the reaction mixture was reacted for another 30 min. Upon the addition of 4-*tert*-butoxystyrene the color changed immediately to bright yellow. Alternating, calculated amounts of styrene and 4-*tert*-butoxystyrene were added to obtain the desired multiblock copolymer; each block was reacted for 30 min while the temperature of the reaction mixture was kept at -78 °C. The addition of each block was accompanied by the corresponding color change. The color changes happened immediately upon addition of the respective other monomer proving that the rate of reinitiation is very fast as it is required for a living anionic polymerization. The polymerization was terminated by the addition of 1 mL of degassed methanol. The reaction mixture was concentrated to ca. 100 mL and precipitated in 10-fold excess of water. After filtration, the crude product was dried overnight under vacuum at 40 °C. The crude product was dissolved in 80 mL of $CHCl_3$ and reprecipitated in a 10-fold excess of methanol, followed by filtration. The obtained white powder was dried under vacuum overnight at 40 °C.

^{1}H NMR (acetone-d_6, 300 MHz): δ = 1.21 - 1.42 (br s, CH_3), 1.42 - 1.78 (br m, CH_2), 1.78 - 2.18 (br m, CH), 6.34 - 6.93 (br m, ArH), 6.93 - 7.33 (br m, ArH) ppm.

3.2.3 Hydrolysis of S-*b*-(*t*BOS-*b*-S)$_n$-*b*-*t*BOS

The *t*BOS blocks in the resulting S-*b*-(*t*BOS-*b*-S)$_n$-*b*-*t*BOS multiblock copolymer were hydrolyzed to obtain a S-*b*-(*p*HS-*b*-S)$_n$-*b*-*p*HS multiblock copolymer, as depicted in Scheme 1.

S-*b*-(*t*BOS-*b*-S)$_n$-*b*-*t*BOS multiblock copolymer was dissolved in dioxane and a 5-fold excess of concentrated HCl was added. Hydrolysis was carried out overnight at 80 °C under nitrogen atmosphere. The reaction mixture was concentrated and precipitated in a 10-fold excess of water. After neutralization with 5 wt% NaOH solution to a pH value of 6-7, the crude product was filtered and dried overnight under vacuum at 40 °C. The crude product was dissolved in THF and reprecipitated in a 10-fold excess of hexanes, filtered and dried under vacuum overnight at 40 °C to obtain a white solid.

^{1}H NMR (acetone-d_6, 300 MHz): δ = 1.15 - 1.76 (br m, CH_3), 1.76 - 2.18 (br m, CH), 6.23 - 6.89 (br m, ArH), 6.89 - 7.33 (br m, ArH), 7.58 - 8.46 (br s, ArOH) ppm.

3.2.4 Sample preparation

S-*b*-(*p*HS-*b*-S)$_n$-*b*-*p*HS multiblock copolymer films were cast from either THF or dioxane. The solvent was slowly evaporated and the sample was annealed in a saturated vapor for at least one week. Subsequently the film was placed in an oven for 30 min at 140 °C.

3.2.5 Characterization

Gel permeation chromatography (GPC) measurements were performed in THF at 25 °C (1 mL min^{-1}) on a Spectra-Physics AS 1000, equipped with PLGel 5 μm 30 cm mixed-C columns. Universal calibration was applied using a Viscotek H502 viscometer and Shodex RI-71 refractive index detector. The GPC was calibrated using narrow disperse polystyrene standards (Polymer Laboratories).

^{1}H nuclear magnetic resonance (^{1}H NMR) spectra were recorded on a 300 MHz Varian VXR at room temperature, using acetone-d_6 as solvent unless noted differently. Attenuated total reflection infrared (ATR-IR) spectrometry was performed at room temperature on a Bruker IFS 88.

Bright-field transmission electron microscopy (TEM) was performed on a JEOL-1200EX transmission electron microscope operating at an accelerating voltage of 120 kV. To prepare TEM samples, ultrathin sections (ca. 80 nm) of a solvent-cast block copolymer film embedded in epoxy resin (Epofix, Eletron Microscopy Sciences) were microtomed using a Leica Ultracut UCT-ultramicrotome and a Diatome diamond knife at room temperature, placed on copper grids and vapor stained with OsO_4 to obtain contrast during TEM measurements.

Small-angle X-ray scattering (SAXS) measurements were performed at the Dutch-Belgian Beamline (DUBBLE) at the European Synchrotron Radiation Facility (ESRF) in Grenoble, France.[57-59] The sample-to-detector distance was about 8 m, while the X-ray wavelength was 1.24 Å (E = 10 keV). Standard corrections for sample absorption and background subtraction have been performed. The data were normalized with respect to the incident beam intensity in order to correct for primary beam intensity fluctuations. The scattering patterns from silver behenate (AgBe) were used for the calibration of the wave vector scale of the scattering curve. The scattering vector q is defined as $q = (4\pi/\lambda)\ sin\ \theta$, where θ is half of the scattering angle. The samples were heated shortly to 200 °C before collecting the data at room temperature.

3.3 Results and discussion

3.3.1 Synthesis of S-*b*-(*p*HS-*b*-S)$_n$-*b*-*p*HS multiblock copolymers

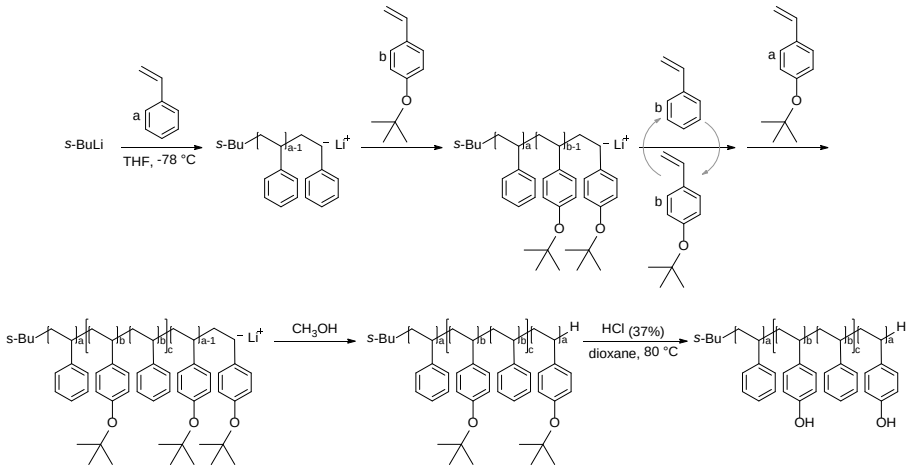

Scheme 3.1 Synthesis of a S-*b*-(*p*HS-*b*-S)$_n$-*b*-*p*HS multiblock copolymer via sequential anionic polymerization of styrene and *tert*-butoxystyrene and subsequent hydrolysis of the *tert*-butoxy group.

S-*b*-(*p*HS-*b*-S)$_n$-*b*-*p*HS multiblock copolymers with a two-length-scale molecular architecture were prepared through a multistep sequential living anionic polymerization of S-*b*-(*t*BOS-*b*-S)$_n$-*b*-*t*BOS multiblock copolymers followed by hydrolysis of the *tert*-butoxy group (Scheme 3.1).

A lot of research has been conducted on the synthesis of block copolymers of styrene and protected hydroxystyrene via living anionic polymerization.[41, 42, 44, 45] In order to obtain *p*HS blocks with a narrow polydispersity, protection of the phenol groups prior to anionic polymerization is required, to avoid termination of the living chain ends. Therefore, *tert*-butoxystyrene was used since it is commercially available and the *tert*-butyl ether can be hydrolyzed under relative mild conditions. Furthermore, styrene and *tert*-butoxystyrene are able to be polymerized sequentially.

Table 3.1 Molecular characteristics of the S-*b*-(*t*BOS-*b*-S)$_n$-*b*-*t*BOS multiblock copolymers.

# of blocks	M_n inner blocks [a] (kg mol^{-1})		M_n outer blocks [a] (kg mol^{-1})		M_n total [b] (kg mol^{-1})	PDI [c]
	S	*t*BOS	S	*t*BOS		
6	2.9	4.3	29.7	42.6	86.7	1.02 [a]
8	8.7	12.7	26.0	38.1	128.3	1.02 [a]

[a,b] On the basis of initiator/monomer ratio and the molecular weight of the polystyrene precursor. [c] Determined by GPC (THF).

A hexablock copolymer and an octablock copolymer were successfully synthesized. The corresponding molecular parameters, together with the results from GPC analysis, are presented in Table 3.1. Figure 3.2 compares the GPC chromatograms of the two multiblock copolymers synthesized, both indicating a narrow molecular weight distribution. The polydispersity index (PDI) values for the hexablock- and the octablock copolymer, determined by universal calibration, are 1.09 and 1.25 respectively.

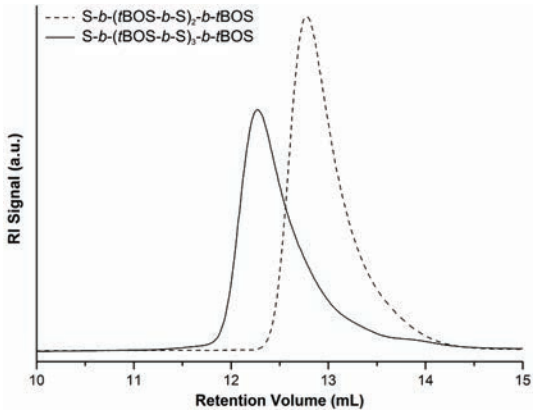

Figure 3.2 GPC chromatograms of the hexablock (dashed line) and the octablock (solid line) copolymers.

The corresponding FTIR spectra of the S-*b*-(*p*HS-*b*-S)$_n$-*b*-*p*HS multiblock copolymers after hydrolysis (Figure 3.3b for n = 6) display a broad peak at 3340 cm^{-1} that is

initially absent (Figure 3.3a). This indicates the successful conversion from *tert*-butoxy to hydroxyl groups.

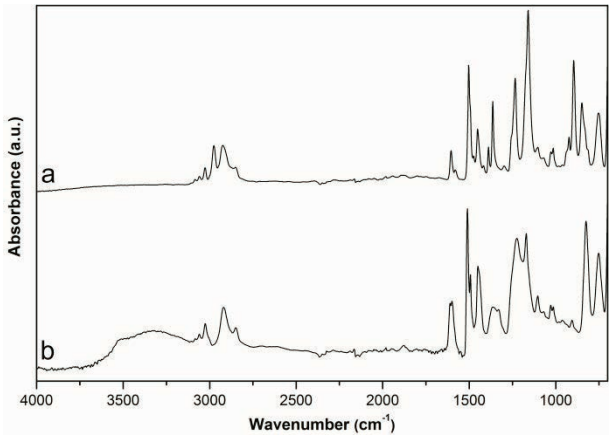

Figure 3.3 FTIR spectra of the octablock copolymer (a) before and (b) after hydrolysis.

Hydrolysis was also studied by ^{1}H NMR spectroscopy. Figure 3.4 displays a for the multiblock copolymers typical ^{1}H NMR spectra before (a) and after hydrolysis (b). The large chemical shift around 1.31 ppm, corresponding to the *tert*-butyl protons in the initial S-*b*-(*t*BOS-*b*-S)$_n$-*b*-*t*BOS multiblock copolymer, completely disappears in the spectrum of the deprotected S-*b*-(*p*HS-*b*-S)$_n$-*b*-*p*HS multiblock copolymer indicating that the hydrolysis was completed. A broad peak located around 8.0 ppm, corresponding to phenol protons, appears after the acidic cleavage thus proving the successful hydrolysis of the ester groups.

The compositions of the S-*b*-(*p*HS-*b*-S)$_n$-*b*-*p*HS multiblock copolymers were determined using the relative intensities of the aromatic protons of styrene and *p*-hydroxystryrene (6.1-7.4 ppm), and the results are presented in Table 3.2.

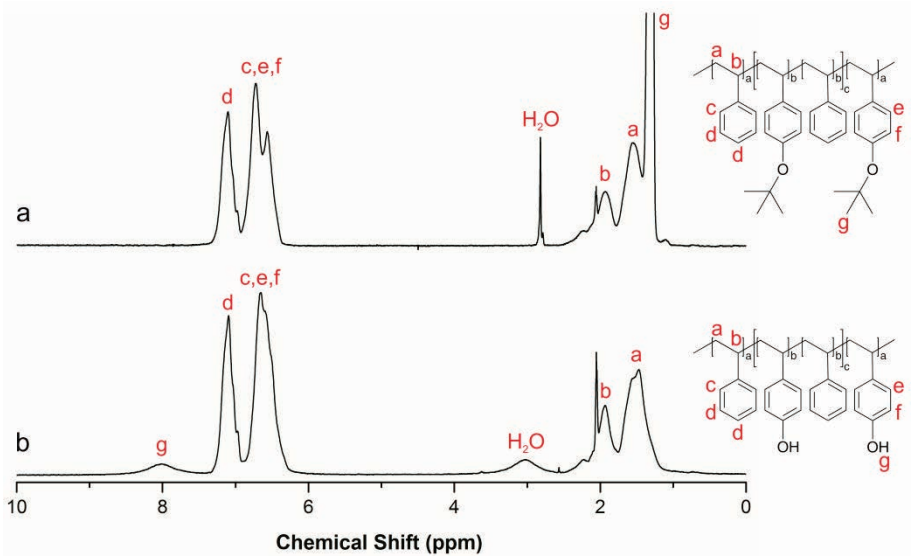

Figure 3.4 ^{1}H NMR spectra of a multiblock copolymer in acetone-d6 (a) before and (b) after hydrolysis.

Table 3.2 Molecular characteristics of the S-*b*-(*p*HS-*b*-S)$_n$-*b*-*p*HS multiblock copolymers.

# of blocks	M_n inner blocks [a] (kg mol^{-1})		M_n outer blocks [a] (kg mol^{-1})		M_n total [b] (kg mol^{-1})	weight fraction *p*HS [c]
	S	*p*HS	S	*p*HS		
6	2.9	2.9	29.7	29.0	70.3	0.48
8	8.7	8.7	26.0	26.0	104.2	0.47

[a,b] On the basis of the molecular weight of the *t*BOS precursor. [c] Determined by ^{1}H NMR.

3.3.2 Morphology

To study the microphase separation, solvent-cast films of the multiblock copolymers were prepared and the structure was investigated using small-angle X-ray scattering (SAXS) and transmission electron microscopy (TEM).

3.3.2.1 Hexablock copolymer

Figure 3.5 shows the SAXS intensity profile for the S-*b*-(*p*HS-*b*-S)$_2$-*b*-*p*HS hexablock copolymer. The scattering peaks are at the ratio 1:2:3 indicating a lamellar ordered structure. From the value of the first order peak q = 0.171 nm^{-1}, the characteristic domain spacing D is calculated to be 37 nm.

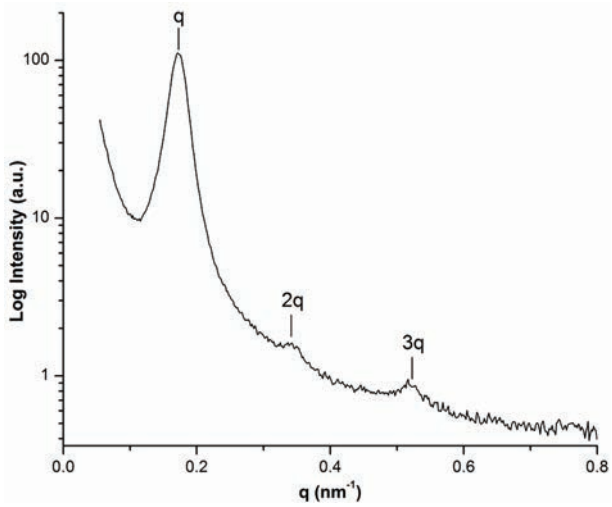

Figure 3.5 SAXS intensity profile for a S-*b*-(*p*HS-*b*-S)$_2$-*b*-*p*HS hexablock copolymer, where M_n (outer blocks) = 29,000 g mol^{-1} and M_n (inner blocks) = 2,900 g mol^{-1}.

Figure 3.6 shows TEM images of thin film sections of the S-*b*-(*p*HS-*b*-S)$_2$-*b*-*p*HS hexablock copolymer stained with OsO_4. After staining the *p*HS phase appears dark and the lamellar structure can clearly be seen. The distance between the lamellar planes is 36 to 39 nm. Furthermore, it is clear from Figure 3.6 that there are no separate thin layers present originating from the short inner blocks. This implies that the short blocks of the middle multiblock either organize at the interface as schematically illustrated in Figure 3.1a$_I$ for the octablock copolymer system, or, alternatively, are too

short to microphase separate and are simply distributed throughout the layers formed by the long outer blocks. Since $\chi_{S,pHS} \cong 0.68$, implying $\chi N > 30$ for N being the length of the middle diblock, the last possibility can be dismissed. Lamellar-in-lamellar self-assembly of A-*b*-(B-*b*-A)$_n$-*b*-B two-length-scale multiblock copolymers has not yet been analyzed theoretically in the strong segregation limit. The first experimental realization of two-length-scale multiblock copolymers concerned a S-ISISISISI-S undecablock copolymer system,[18] which prompted a theoretical strong segregation analysis of the corresponding A-*b*-(B-*b*-A)$_n$-*b*-B-*b*-A system.[29] It was demonstrated that the extra entropy due to different ways of organizing loops and bridges in the case of internal structures alone is not sufficient to make the hierarchical structure formation favorable. The presence of strongly anisotropic stretching of the long end blocks in the outer thick A-layers due to the presence of many loops of the short middle A-blocks, which necessarily accompanies structure formation without thin layers (cf. Figure 3.1a$_I$), gives an additional unfavorable free energy contribution that is essential for internal domain formation. Although the theoretical predictions reported in the literature[29] were restricted to $n \geq 3$, it was shown that for certain values of the characteristic parameters (relative length of internal blocks, value of the interaction parameter) no additional internal structure formation should take place for the smallest values of $n = 3$ and 4 considered. As already mentioned in the Introduction and illustrated in Figure 3.1b, for A-*b*-(B-*b*-A)$_3$-*b*-B-*b*-A the number of thin layers is 1, 3, 5 or 7 compared to 0, 2, 4 or 6 for our octablock copolymer. According to the analysis presented in reference 29, for molar masses of the outer and inner blocks as for our hexablock copolymer and a Flory-Huggins interaction parameter equal to 0.68,[54] the number of internal layers for A-*b*-(B-*b*-A)$_3$-*b*-B-*b*-A would have been the minimal number 1. Hence, even though the reported theoretical analysis addresses a slightly different system, the fact that for our hexablock copolymer no internal layers are observed, which is the minimum in this case, is in excellent agreement with these findings.

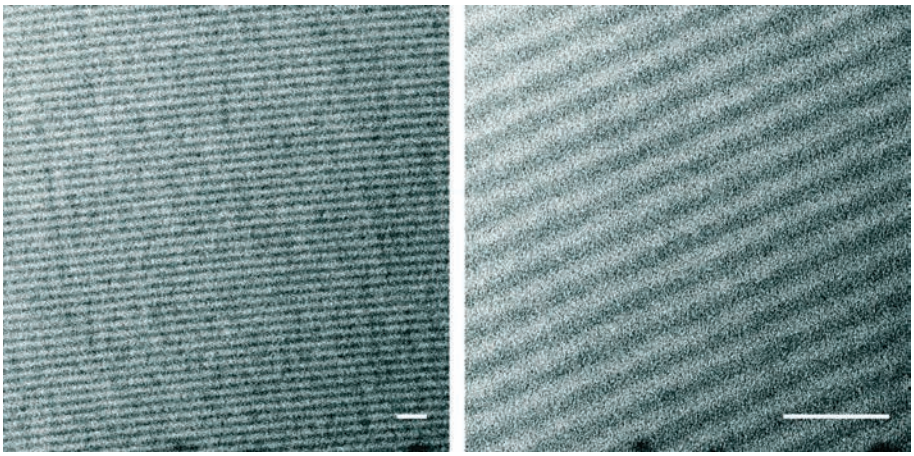

Figure 3.6 Bright-field TEM images of a S-*b*-(*p*HS-*b*-S)$_2$-*b*-*p*HS hexablock copolymer, where M_n (outer blocks) = 29,000 g mol^{-1} and M_n (inner blocks) = 2,900 g mol^{-1}, stained with OsO_4. Both scale bars represent 100 nm.

3.3.2.2 Octablock copolymer

Figure 3.7 shows the SAXS intensity profile for the S-*b*-(*p*HS-*b*-S)$_3$-*b*-*p*HS octablock copolymer. The scattering peaks are at a ratio of 1:2:3:4:5:6 indicating a lamellar ordered structure. From the value of the first order peak the domain spacing is calculated to be 80 nm, which is much larger than would be expected on the basis of microphase separation between the outer blocks alone. It indicates that the inner blocks of the octablock copolymer, which are considerably longer than those of the hexablock copolymer considered above, are now microphase separated as well. Of course, if both type of layers are parallel only the overall periodicity will show up in SAXS. The lamellar-in-lamellar morphology is confirmed by the TEM images presented in Figure 3.8. It shows that the self-assembled state consists of two large layers separated by two thin inner layers, which corresponds to the situation schematically presented in Figure 3.1a$_{II}$.

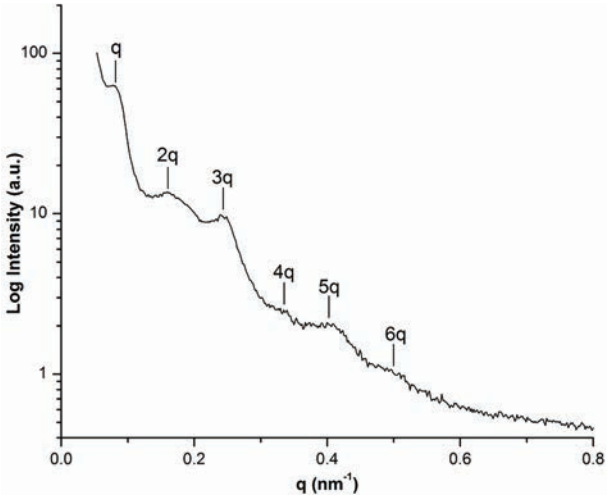

Figure 3.7 SAXS intensity profile for an S-*b*-(*p*HS-*b*-S)$_3$-*b*-*p*HS octablock copolymer, where M_n (outer blocks) = 26,000 g mol^{-1} and M_n (inner blocks) = 8,700 g mol^{-1}.

The two A-*b*-(B-*b*-A)$_n$-*b*-B multiblock copolymers considered differ in two aspects. The octablock contains an additional short diblock and these middle diblocks have a considerable larger molar mass than those of the hexablock. According to the reported theoretical predictions,[29] both aspects favor internal structure formation for the octablock in comparison to the hexablock copolymer. The former because of the entropic contribution associated with the many different conformations (loops and bridges, see Figure 3.1a$_{II}$) and the latter because of the larger block incompatibility. Larger block lengths lead to additional chain stretching (cf. simple diblocks) and additional chain stretching is at some point relieved by additional layer formation. For the block lengths involved and a χ-parameter value of 0.68, the corresponding A-*b*-(B-*b*-A)$_3$-*b*-B-*b*-A multiblock copolymer system considered theoretically is predicted to have 3 internal layers (Figure 3.1b$_{II}$), which again nicely corresponds to the 2 internal layers observed in the S-*b*-(*p*HS-*b*-S)$_3$-*b*-*p*HS octablock.

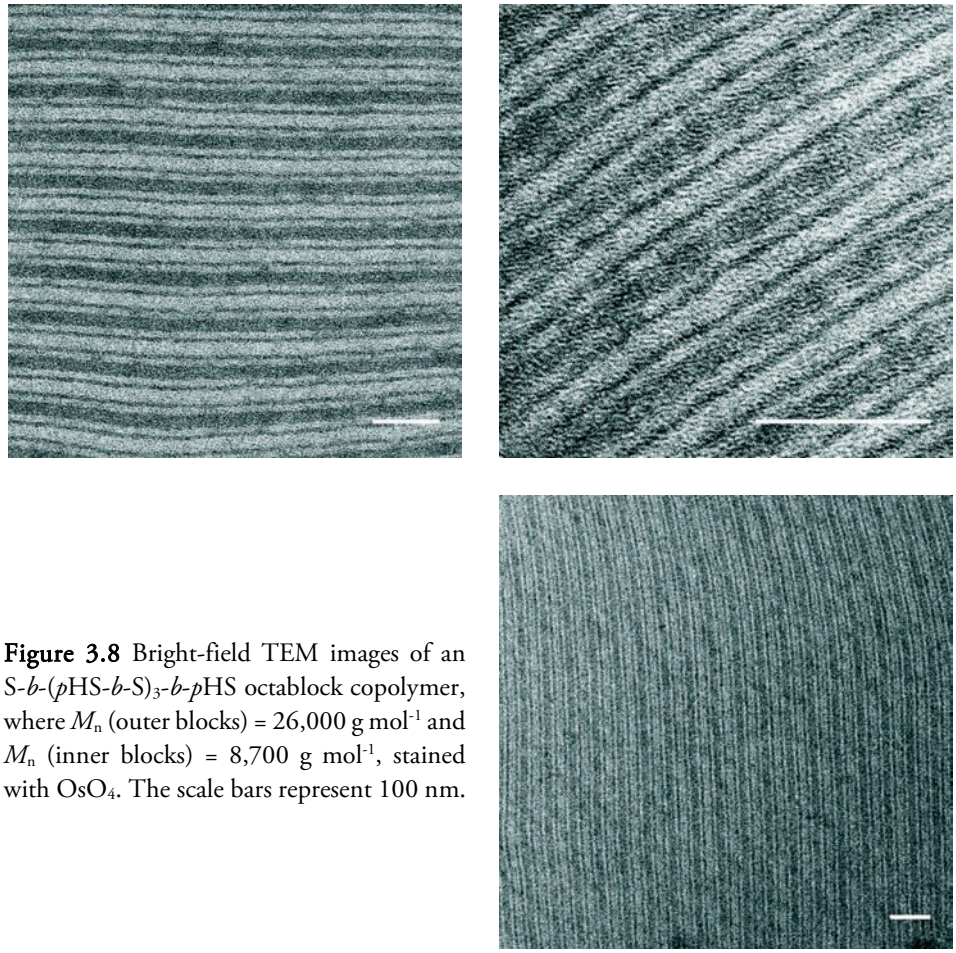

Figure 3.8 Bright-field TEM images of an S-*b*-(*p*HS-*b*-S)$_3$-*b*-*p*HS octablock copolymer, where M_n (outer blocks) = 26,000 g mol^{-1} and M_n (inner blocks) = 8,700 g mol^{-1}, stained with OsO_4. The scale bars represent 100 nm.

3.4 Conclusion

A hexablock copolymer and an octablock copolymer, both with a large polystyrene and a large poly-*p*-hydroxystyrene end block, and 2 resp. 3 short inner S-*b*-*p*HS diblocks, have been successfully synthesized. Using TEM and SAXS the morphology of both polymers was investigated. For the hexablock a single periodic lamellar morphology was observed. The absence of additional "thin" layers is because of the small number of inner blocks and the relatively small molar mass of the inner blocks. The octablock showed a lamellar-in-lamellar morphology where two thin layers formed by the inner blocks are present inside the two thick layers formed by the end blocks. Both results are in excellent agreement with the theoretical predictions for a comparable A-*b*-(B-*b*-A)$_n$-*b*-B-*b*-A two-length-scale binary multiblock copolymer system.[26]

3.5 References

1. Leibler, L. *Macromolecules* **1980,** 13, (6), 1602-1617.
2. Semenov, A. N. *Sov. Phys. JETP* **1985,** 61, 733-742.
3. Bates, F. S.; Fredrickson, G. H. *Annu. Rev. Phys. Chem.* **1990,** 41, 525-557.
4. Matsen, M. W.; Schick, M. *Phys. Rev. Lett.* **1994,** 72, (16), 2660-2663.
5. Matsen, M. W.; Bates, F. S. *Macromolecules* **1996,** 29, (4), 1091-1098.
6. Hamley, I. W., *The physics of block copolymers*. Oxford University Press: 1998.
7. Tyler, C. A.; Morse, D. C. *Phys. Rev. Lett.* **2005,** 94, (20), 208302.
8. Takenaka, M.; Wakada, T.; Akasaka, S.; Nishitsuji, S.; Saijo, K.; Shimizu, H.; Kim, M. I.; Hasegawa, H. *Macromolecules* **2007,** 40, (13), 4399-4402.
9. Bates, F. S.; Fredrickson, G. H. *Phys. Today* **1999,** 52, (2), 32-38.
10. Abetz, V.; Simon, P. F. W. *Adv. Polym. Sci.* **2005,** 189, 125-212.
11. Park, C.; Yoon, J.; Thomas, E. L. *Polymer* **2003,** 44, (22), 6725-6760.
12. Hamley, I. W. *Angew. Chem.-Int. Edit.* **2003,** 42, (15), 1692-1712.
13. Bailey, T. S. Morphological behavior spanning the symmetric AB and ABC block copolymer states. Thesis, University of Minnesota, 2001.
14. Epps, T. H.; Cochran, E. W.; Hardy, C. M.; Bailey, T. S.; Waletzko, R. S.; Bates, F. S. *Macromolecules* **2004,** 37, (19), 7085-7088.
15. Matsushita, Y. *Macromolecules* **2007,** 40, (4), 771-776.
16. Hayashida, K.; Dotera, T.; Takano, A.; Matsushita, Y. *Phys. Rev. Lett.* **2007,** 98, (19), 195502.
17. Masuda, J.; Takano, A.; Nagata, Y.; Noro, A.; Matsushita, Y. *Phys. Rev. Lett.* **2006,** 97, (9), 098301.
18. Nagata, Y.; Masuda, J.; Noro, A.; Cho, D. Y.; Takano, A.; Matsushita, Y. *Macromolecules* **2005,** 38, (24), 10220-10225.
19. Masuda, J.; Takano, A.; Suzuki, J.; Nagata, Y.; Noro, A.; Hayashida, K.; Matsushita, Y. *Macromolecules* **2007,** 40, (11), 4023-4027.
20. Fleury, G.; Bates, F. S. *Macromolecules* **2009,** 42, (5), 1691-1694.
21. Fleury, G.; Bates, F. S. *Macromolecules* **2009,** 42, (10), 3598-3610.
22. Nap, R. J.; Kok, C.; ten Brinke, G.; Kuchanov, S. I. *Eur. Phys. J. E* **2001,** 4, (4), 515-519.
23. Smirnova, Y. G.; ten Brinke, G.; Erukhimovich, I. Y. *Polym. Sci. Ser. A* **2005,** 47, (5), 430-435.
24. Kuchanov, S.; Pichugin, V.; Ten Brinke, G. *e-Polymers* **2006,** 12, 1-31.
25. Kuchanov, S.; Pichugin, V.; Ten Brinke, G. *Europhys. Lett.* **2006,** 76, (5), 959-964.

26. Nap, R.; Sushko, N.; Erukhimovich, I.; ten Brinke, G. *Macromolecules* **2006,** 39, (19), 6765-6770.
27. Smirnova, Y. G.; ten Brinke, G.; Erukhimovich, I. Y. *J. Chem. Phys.* **2006,** 124, (5), 054907.
28. Kriksin, Y. A.; Erukhimovich, I. Y.; Khalatur, P. G.; Smirnova, Y. G.; ten Brinke, G. *J. Chem. Phys.* **2008,** 128, (24), 244903.
29. Klymko, T.; Subbotin, A.; ten Brinke, G. *J. Chem. Phys.* **2008,** 129, (11), 114902.
30. Kriksin, Y. A.; Erukhimovich, I. Y.; Smirnova, Y. G.; Khalatur, P. G.; ten Brinke, G. *J. Chem. Phys.* **2009,** 130, (20), 204901.
31. Ruokolainen, J.; Makinen, R.; Torkkeli, M.; Makela, T.; Serimaa, R.; ten Brinke, G.; Ikkala, O. *Science* **1998,** 280, (5363), 557-560.
32. Ruokolainen, J.; ten Brinke, G.; Ikkala, O. *Adv. Mater.* **1999,** 11, (9), 777-780.
33. Mori, K.; Okawara, A.; Hashimoto, T. *J. Chem. Phys.* **1996,** 104, (19), 7765-7777.
34. Macdonald, S. A.; Willson, C. G.; Frechet, J. M. J. *Accounts Chem. Res.* **1994,** 27, (6), 151-158.
35. Iwayanagi, T.; Kohashi, T.; Nonogaki, S.; Matsuzawa, T.; Douta, K.; Yanazawa, H. *IEEE Trans. Electron Devices* **1981,** 28, (11), 1306-1310.
36. Cho, H.; Kim, J.; Patil, P.; Kim, J. Y.; Kim, T. H. *J. Appl. Polym. Sci.* **2007,** 103, (6), 3560-3566.
37. Uhrich, K. E.; Reichmanis, E.; Heffner, S. A.; Kometani, J. M.; Nalamasu, O. *Chem. Mat.* **1994,** 6, (3), 287-294.
38. Kawabata, N.; Taketani, Y. *Bull. Chem. Soc. Jpn.* **1980,** 53, (10), 2986-2989.
39. Aguiar, M.; Hu, B.; Karasz, F. E.; Akcelrud, L. *Macromolecules* **1996,** 29, (9), 3161-3166.
40. Aguiar, M.; Karasz, F. E.; Akcelrud, L. *Macromolecules* **1995,** 28, (13), 4598-4602.
41. Tung, P. H.; Kuo, S. W.; Chan, S. C.; Hsu, C. H.; Wang, C. F.; Chang, F. C. *Macromol. Chem. Phys.* **2007,** 208, (16), 1823-1831.
42. Conlon, D. A.; Crivello, J. V.; Lee, J. L.; Obrien, M. J. *Macromolecules* **1989,** 22, (2), 509-516.
43. Uhrich, K. E.; Reichmanis, E.; Heffner, S. A.; Kometani, J. M. *Macromolecules* **1994,** 27, (18), 4936-4940.
44. Ito, H.; Knebelkamp, A.; Lundmark, S. B.; Nguyen, C. V.; Hinsberg, W. D. *J. Polym. Sci. Pol. Chem.* **2000,** 38, (13), 2415-2427.

45. Zhao, J. Q.; Pearce, E. M.; Kwei, T. K.; Jeon, H. S.; Kesani, P. K.; Balsara, N. P. *Macromolecules* **1995,** 28, (6), 1972-1978.
46. Ohno, K.; Ejaz, M.; Fukuda, T.; Miyamoto, T.; Shimizu, Y. *Macromol. Chem. Phys.* **1998,** 199, (2), 291-297.
47. du Sart, G. G.; Vukovic, I.; van Ekenstein, G. A.; Polushkin, E.; Loos, K.; ten Brinke, G. *Macromolecules* **2010,** 43, (6), 2970-2980.
48. Kuo, S. W.; Tung, P. H.; Chang, F. C. *Macromolecules* **2006,** 39, (26), 9388-9395.
49. Rahman, S. S. A.; Kawaguchi, D.; Matsushita, Y. *Polymer* **2011,** 52, (1), 164-171.
50. Rahman, S. S. A.; Kawaguchi, D.; Matsushita, Y. *Macromolecules* **2011,** 44, (8), 2799-2807.
51. Mountrichas, G.; Pispas, S. *J. Polym. Sci. Pol. Chem.* **2007,** 45, (24), 5790-5799.
52. Matsushita, Y.; Mogi, Y.; Mukai, H.; Watanabe, J.; Noda, I. *Polymer* **1994,** 35, (2), 246-249.
53. Wu, L. F.; Cochran, E. W.; Lodge, T. P.; Bates, F. S. *Macromolecules* **2004,** 37, (9), 3360-3368.
54. Smith, S. D.; Spontak, R. J.; Satkowski, M. M.; Ashraf, A.; Heape, A. K.; Lin, J. S. *Polymer* **1994,** 35, (21), 4527-4536.
55. Han, S. H.; Kim, J. K.; Pryamitsyn, V.; Ganesan, V. *Macromolecules* **2011,** 44, (12), 4970-4976.
56. Zhu, K. J.; Chen, S. F.; Ho, T.; Pearce, E. M.; Kwei, T. K. *Macromolecules* **1990,** 23, (1), 150-154.
57. Bras, W.; Dolbnya, I. P.; Detollenaere, D.; van Tol, R.; Malfois, M.; Greaves, G. N.; Ryan, A. J.; Heeley, E. *J. Appl. Crystallogr.* **2003,** 36, 791-794.
58. Borsboom, M.; Bras, W.; Cerjak, I.; Detollenaere, D.; van Loon, D. G.; Goedtkindt, P.; Konijnenburg, M.; Lassing, P.; Levine, Y. K.; Munneke, B.; Oversluizen, M.; van Tol, R.; Vlieg, E. *J. Synchrot. Radiat.* **1998,** 5, 518-520.
59. Nikitenko, S.; Beale, A. M.; van der Eerden, A. M. J.; Jacques, S. D. M.; Leynaud, O.; O'Brien, M. G.; Detollenaere, D.; Kaptein, R.; Weckhuysen, B. M.; Bras, W. *J. Synchrot. Radiat.* **2008,** 15, 632-640.

Chapter 4

Comb Copolymer Complexes of Poly(*p*-hydroxystyrene) and 4-Alkylpyridine Amphiphiles

The self-assembly of the hydrogen-bonded complex between poly(p-hydroxystyrene) (PpHS) and 4-alkylpyridine amphiphiles is discussed. Anionic polymerization of tBOS followed by hydrolysis of the tert-butoxy group resulted in a PpHS homopolymer. Three different 4-alkylpyridine amphiphiles were synthesized by first converting primary alcohols to alkyl iodides and subsequently coupling the alkyl iodides to 4-picoline. Via this route, 4-heptadecylpyridine (HDPy), 4-nonadecylpyridine (NDPy) and 4-heneicosylpyridine (HEPy) were synthesized successfully. The formation of a hydrogen-bonded complex between the 4-alkylpyridines and PpHS is studied using infrared spectroscopy. The disappearance of the band at 3300 cm^{-1} and the shifts of the bands at 1415 cm^{-1} and 993 cm^{-1} indicate that the formation hydrogen-bonded complex between PpHS and HEPy is nearly complete when stoichiometric amounts are used. Furthermore, the hydrogen-bonding appears to be quite stable at higher temperatures. The results of the investigation of the supramolecular complexes via differential scanning calorimetry (DSC), small-angle X-ray scattering (SAXS) and wide angle X-ray scattering (WAXS) are perfectly in agreement with each other and indicate that the formation of an ordered lamellar morphology depends on the length of the alkyl tail of the amphiphile and the amphiphile mole fraction x.

4.1 Introduction

The combination of supramolecular principles with block copolymer self-assembly has proven to be a very promising concept in nanotechnology.[1-6] In particular, comb-shaped supramolecules formed by amphiphilic side chains noncovalently attached to a linear polymer backbone, have been studied in depth theoretically as well as experimentally. Physical interactions, such as ionic interactions,[7, 8] coordination bonding,[9] and hydrogen-bonding,[4] can be used to prepare such supramolecular structures. Of these, hydrogen-bonding appears to be the most promising as it results in materials that can be manipulated relatively easily by external stimuli, temperature in particular.[1, 10] Besides homopolymers,[1, 11] di-,[1] and triblock copolymers [12] have been used so far. When the hydrogen-bonding between the amphiphilic side chains and the polymer backbone is strong enough, the supramolecular systems behave like their copolymer analogues. However, thanks to the thermoreversibility of the hydrogen-bond, the system's ability to self-assemble and form structures is greatly improved through the increased mobility compared to covalently bonded systems.

The characteristic length scale of the self-assembled structures as well as the structure itself can easily be manipulated varying the amount of low molecular component. After the self-assembled structure desired is obtained there is the additional possibility to remove the low molecular weight amphiphiles by dissolving in a suitable solvent.[13] This concept has been extensively pursued by Stamm and co-workers using PS-*b*-P4VP diblock copolymers in combination with 2-(4-hydroxybenzeneazo)benzoic acid to create nanoporous thin films.[14, 15] In our group PDP-based supramolecular block copolymer bulk samples exhibiting a large-length-scale bicontinuous gyroid morphology were likewise used to create continuous nanoporous polymeric structures, which were used as templates to produce, e.g., metallic nickel nanofoams.[16, 17]

The systematic study of bulk phase behavior of comb-shaped supramolecules was pioneered by the groups of Ikkala and Ten Brinke.[1, 4, 11, 18-22] Self-assembly in the melt of complexes consisting of pentadecylphenol (PDP) or nonadecylphenol (NDP) hydrogen-bonded to poly-4-vinylpyridine (P4VP) were studied meticulously. Infrared studies (IR) showed that the hydrogen-bonding is fairly complete for stoichiometric compositions (i.e., one PDP molecule per pyridine group), when the temperature is below 100 °C.[22, 23] Temperature dependent small-angle X-ray scattering (SAXS)

showed that under stoichiometric conditions there is an order-disorder transition (ODT) at about 65 °C when cooling from a high-temperature isotropic state.[11] The resulting microphase separated lamellar morphology consists of non-polar alkyl tails segregated from the polar P4VP/phenol complex. The alkyl tails crystallize around room temperature. If the temperature is increased above the ODT a characteristic correlation hole peak is present at a position and with a height depending on the fraction of hydrogen bonds.[24] The combination of block copolymers of P4VP and polystyrene (PS) with NDP and PDP resulted in structures-in-structure morphologies, which were systematically imaged by transmission electron microscopy (TEM).[25]

Recently, *tert*-butoxystyrene (*t*BOS) was used in our group in the synthesis of P*t*BOS-*b*-PS-*b*-P4VP triblock copolymers[12] and PS-*b*-(P*t*BOS-*b*-PS)$_n$-*b*-P*t*BOS multiblock copolymers (Chapter 3).[26] In order to obtain self-assembled structures with the latter multiblock copolymers, the *tert*-butyl ether was hydrolyzed to result in poly(*p*-hydroxystyrene) (P*p*HS) so that PS-*b*-(P*p*HS-*b*-PS)$_n$-*b*-P*p*HS multiblock copolymers were obtained. Because *p*-hydroxystyrene has a much more unfavorable interaction with styrene than *tert*-butoxystyrene, the PS-*b*-(P*p*HS-*b*-PS)$_n$-*b*-P*p*HS multiblock copolymers synthesized showed interesting two-length-scale phase behavior.[26] Because P*p*HS can also be used as a proton donor for hydrogen-bonding a third length scale may conceptually be introduced if P*p*HS is combined with suitable amphiphiles such as, e.g., alkylpyridine amphiphiles. In that case a supramolecular system is obtained that is similar to the P4VP/PDP hydrogen-bonded complexes described above. The subtle difference in this case is that the pyridine group is now part of the amphiphile whereas the phenol group is attached to the backbone of the polymer, as depicted in Scheme 4.1. If this concept works, the use of PS-*b*-P*p*HS diblock copolymers will result in all the possibilities discussed before for the PS-*b*-P4VP systems, except that after removing the alkylpyridine amphiphiles interesting nanoporous systems may be obtained with pores covered with hydroxyl rather than pyridine groups.

In this chapter, the P*p*HS/4-alkylpyridine system is investigated using homopolymer P*p*HS. Therefore, a P*t*BOS homopolymer was synthesized anionically and after hydrolysis a P*p*HS homopolymer was obtained (Scheme 4.2).

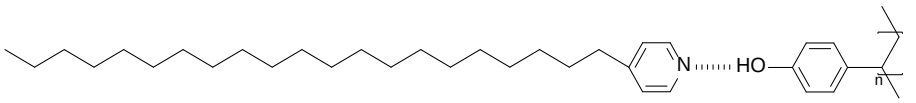

Scheme 4.1 Schematics of the hydrogen-bonding between poly(*p*-hydroxystyrene) and 4-henicosylpyridine.

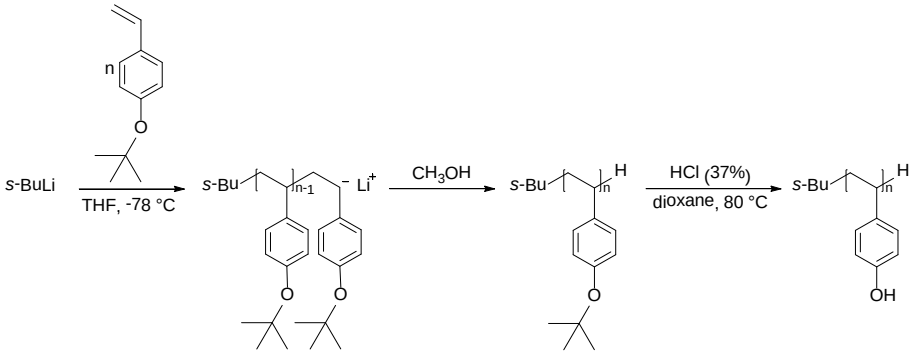

Scheme 4.2 Synthesis of P*p*HS homopolymer via anionic polymerization of *tert*-butoxystyrene and subsequent hydrolysis of the *tert*-butoxy group.

Furthermore, three different 4-alkylpyridine amphiphiles **3** were synthesized by first converting primary alcohols **1** to alkyl iodides **2** and subsequent coupling to 4-picoline (Scheme 4.3). Via this route, 4-heptadecylpyridine (HDPy), 4-nonadecylpyridine (NDPy) and 4-heneicosylpyridine (HEPy) were synthesized.

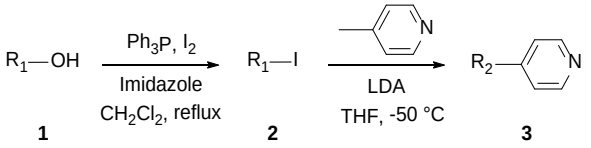

Scheme 4.3 Synthesis of alkyl iodides (**2**) and 4-alkylpyridine amphiphiles (**3**).

The hydrogen-bonding between the pyridine group of HEPy and the phenol group of P*p*HS was investigated via FTIR spectroscopy in which the samples varied in

amphiphile mole fraction x (x = 0.5, 1.0, and 1.5). Here, x represents the ratio between the pyridine groups of the amphiphile and the phenol groups of the polymer. The different supramolecular complexes formed between P*p*HS and HDPy (x = 1.0), NDPy (x = 1.0), and HEPy (x = 0.5, 1.0, and 1.5) were investigated with differential scanning calorimetry (DSC) and simultaneous small angle X-ray scattering SAXS and wide angle X-ray scattering (WAXS) during cooling from the melt. The results are compared with the thoroughly investigated P4VP/PDP supramolecular system and the differences observed are discussed.

4.2 Experimental

4.2.1 Materials

Iodine (I_2, Boom, 99.5%), triphenylphosphine (PPh_3, Merck, 99%), imidazole (Aldrich, 99%), sodium thiosulphate pentahydrate ($Na_2S_2O_3 \cdot 5H_2O$, Merck, 99.5%), 1-hexadecanol (Sigma-Aldrich, 99%), 1-octadecanol (Acros, 95%), 1-eicosanol (Acros, 98%), dichloromethane (CH_2Cl_2, Lab-Scan, 98%), ethyl acetate (Acros, 99%), hexane (Lab-Scan, 99%), diisopropylamine (Acros, 99%), *n*-butyllithium (*n*-BuLi, Aldrich, 2.5 M solution in hexane), *sec*-butyllithium (*s*-BuLi, Aldrich, 1.4 M solution in cyclohexane) and 4-picoline (Acros, 98%), ammonium chloride (NH_4Cl, Acros, 99%), diethyl ether (Lab-Scan, 99.5%), hydrochloric acid (HCl, Merck, 37%), 1,4-dioxane (Acros, 99+%), acetone (Lab-Scan, 99.5%) were used as received. Tetrahydrofuran (THF, Acros, 99.9%) used in the synthesis of 4-alkylpyridine amphiphiles was reacted with *sec*-butyllithium for 30 min at -50 °C under nitrogen atmosphere during which a yellow color indicated that the solvent was dry. Tetrahydrofuran (THF, Acros, 99.9%) used in the anionic polymerization was reacted with *tert*-butyllithium for 1 h at -78 °C under dry nitrogen atmosphere during which a yellow color indicated that the solvent was suitable for anionic polymerization. It was condensed at room temperature into the polymerization flask and subjected to three freeze-pump-thaw cycles. 4-*tert*-Butoxystyrene (*t*BOS, Aldrich, 99%) was distilled twice under reduced pressure from finely ground CaH_2 and stored under nitrogen at -18 °C. Methanol (MeOH, Lab-Scan, 99.8%) was degassed by nitrogen gas flow for 1h at room temperature.

4.2.2 General procedure for the synthesis of alkyl iodides

The synthesis of the alkyl iodides was carried out in oven-dried glassware under a nitrogen atmosphere. A colorless solution of triphenylphosphine (13.53 g, 51.6 mmol) in 380 mL of anhydrous CH_2Cl_2 was slowly added to iodine (13.17 g, 51.9 mmol) at room temperature under a nitrogen atmosphere. This mixture was stirred for approximately 15 min in which a color change was observed from colorless to dark brown. Subsequently, imidazole (7.05 g, 103.5 mmol) was added which resulted in an orange suspension containing yellow imidazole crystals. After stirring for 15 min, a solution of the appropriate alcohol (41.2 mmol) in 100 mL of anhydrous CH_2Cl_2 was added and the reaction mixture was heated at reflux temperature for 20 h. The CH_2Cl_2 was removed under reduced pressure and the residue was diluted with 450 mL of ethyl acetate giving a yellow-brown solution. A solution of $Na_2S_2O_3 \cdot 5H_2O$ (18.00 g, 72.5 mmol) in 125 mL of H_2O was added to reduce the remaining iodine. The now colorless organic layer was separated, washed with three portions of brine (160 mL), dried over Na_2SO_4, filtered and concentrated in vacuo to yield a sticky white/yellow solid. The product was extracted by stirring the solid in hexane (250 mL) for 1 h. The solids were removed by filtration and the filtrate concentrated in vacuo yielding the alkyl iodides (39.5 mmol, 96% yield) as off-white solids. All the alkyl iodides were obtained with yields above 90% and were stored at 6 °C, protected from light, until further use.

Hexadecyl iodide: (13.9 g, 96% yield) ^{1}H NMR ($CDCl_3$, 300 MHz): δ = 0.88 (t, CH_3), 1.1 - 1.5 (br m, CH_2), 1.82 (m, CH_2), 3.20 (t, CH_2) ppm.
Octadecyl iodide: (14.1 g, 91% yield) ^{1}H NMR ($CDCl_3$, 300 MHz): δ = 0.88 (t, CH_3), 1.1 - 1.5 (br m, CH_2), 1.82 (m, CH_2), 3.19 (t, CH_2) ppm.
Eicosyl iodide: (15.8 g, 94% yield) ^{1}H NMR ($CDCl_3$, 300 MHz): δ = 0.88 (t, CH_3), 1.1 - 1.5 (br m, CH_2), 1.82 (m, CH_2), 3.19 (t, CH_2) ppm.

4.2.3 General procedure for the synthesis of 4-alkylpyridine amphiphiles

The synthesis of 4-alkylpyridine amphiphiles was carried out in oven-dried glassware under a nitrogen atmosphere. A solution of diisopropylamine (4.11 g, 40.6 mmol) in 250 mL of dry THF was cooled to -50 °C under a nitrogen atmosphere. Subsequently,

17.0 mL of *n*-BuLi solution (2.5 M in hexane, 42.5 mmol) was added dropwise and the reaction mixture was stirred for an additional 30 min at -50 °C. Then, under careful temperature control, 4-picoline (3.67 g, 39.5 mmol) was added dropwise to the reaction mixture resulting in an orange-red solution that was stirred for another 30 min at -50 °C. Next, a solution of the appropriate alkyl iodide (39.5 mmol) in 50 mL of dry THF was added dropwise at -50 °C. The turbid bright orange-red reaction mixture was stirred for an additional 60 min at -50 °C and at room temperature overnight. While heating up to room temperature the reaction mixture became a clear bright orange-red solution and overnight the color changed from bright orange-red to black. The reaction was quenched with 250 mL of a saturated NH_4Cl solution, the organic layer was separated and the aqueous layer extracted with three portions of diethyl ether (75 mL). The combined organic fractions were washed twice with H_2O (100 mL), twice with brine (175 mL), dried over Na_2SO_4, filtered and concentrated in vacuo to yield a viscous yellow oils that crystallized to a yellow-brown solids at room temperature. The crude product was dissolved in 100 mL of diethyl ether and cooled to 0 °C using an ice bath. Subsequently, 10 mL of concentrated hydrochloric acid (12 M, 0.12 mol) was added and the reaction mixture was stirred for 60 min during which a white precipitate was formed. The solids were isolated by filtration and were recrystallized from 100 mL of 1,4-dioxane yielding a white solid. The white solid was washed thoroughly with diethyl ether and added to 100 mL sodium hydroxide solution (2.5 M in water, 250 mmol). After stirring for 1 h, 100 mL of THF was added to dissolve the white solid. The organic layer was separated and the aqueous layer extracted with two portions of THF (75 mL). The combined organic fractions were dried over Na_2SO_4, filtered and concentrated in vacuo to provide a pale yellow oil. The oil was recrystallized from 400 mL of acetone at -20 °C yielding the 4-alkylpyridine amphiphiles as white solids (17.5 mmol, 44% yield). All the 4-alkylpyridine amphiphiles were obtained with yields around 45%.

4-Heptadecylpyridine: (5.56 g, 44% yield) ^{1}H NMR ($CDCl_3$, 300 MHz): δ = 0.88 (t, CH_3), 1.1 - 1.4 (br m, CH_2), 1.62 (t, CH_2), 2.61 (t, CH_2), 7.14 (t, ArH), 8.48 (t, ArH) ppm.

4-Nonadecylpyridine: (6.06 g, 47% yield) ^{1}H NMR ($CDCl_3$, 300 MHz): δ = 0.88 (t, CH_3), 1.1 - 1.4 (br m, CH_2), 1.62 (t, CH_2), 2.61 (t, CH_2), 7.14 (t, ArH), 8.48 (t, ArH) ppm.
4-Heneicosylpyridine: (7.42 g, 51% yield) ^{1}H NMR ($CDCl_3$, 300 MHz): δ = 0.88 (t, CH_3), 1.1 - 1.4 (br m, CH_2), 1.62 (t, CH_2), 2.61 (t, CH_2), 7.14 (t, ArH), 8.48 (t, ArH) ppm.

4.2.4 Anionic polymerization of P*t*BOS

P*t*BOS Homopolymer was synthesized through anionic polymerization in THF at -78 °C using *s*-BuLi as initiator. The anionic polymerization was performed under dry nitrogen atmosphere in a round-bottomed flask attached to a high-vacuum line. Solvent was condensed into the reaction vessel. Initiator and monomers were transferred to the reaction vessel via a degassed stainless steel needle and syringe.
At room temperature 500 mL of THF was condensed into a 1000 mL flask and after three freeze-pump-thaw cycles the THF was titrated with *s*-BuLi until the solution turned slightly yellow. The solution was cooled down to -78 °C and *tert*-butoxystyrene (9.36 g, 53.1 mmol) was added, followed by 0.24 mL of *s*-BuLi solution (1.4 M in cyclohexane, 0.34 mmol) to initiate the polymerization; a bright yellow color appeared. After 1 h of reaction time the polymerization was terminated by the addition of 1 mL of degassed methanol. The reaction mixture was concentrated to *ca*. 100 mL and precipitated in 10-fold excess of MeOH. After filtration, the crude product was dried overnight under vacuum at 40 °C. The crude product was dissolved in 80 mL of $CHCl_3$ and reprecipitated in a 10-fold excess of methanol, followed by filtration. The obtained white powder was dried under vacuum overnight at 40 °C (9.16 g, 97.9% yield). The molecular weights and polydispersities were determined by GPC in DMF.

P*t*BOS: M_n = 28.5 kg mol^{-1}, M_w = 29.0 kg mol^{-1}, PDI = 1.02; ^{1}H NMR (acetone-d_6, 300 MHz): δ = 1.1 - 1.45 (br s, CH_3), 1.45 - 1.76 (br m, CH_2), 1.76 - 1.98 (br m, CH), 6.3 - 7.0 (br m, ArH) ppm.

4.2.5 Hydrolysis of P*t*BOS

P*t*BOS (1.0 g, M_n = 28.5 kg mol^{-1}, 0.035 mmol) was dissolved in 50 mL of dioxane and 5 mL of concentrated HCl was added. Hydrolysis was carried out overnight at 80 °C under nitrogen atmosphere. The reaction mixture was concentrated and

precipitated in a 10-fold excess of water. After neutralization with 5 wt% NaOH solution to a pH value of 6-7, the crude product was filtered and dried overnight under vacuum at 40 °C. The crude product was dissolved in THF and reprecipitated in a 10-fold excess of hexanes, filtered and dried under vacuum overnight at 40 °C to obtain a white solid (0.58 g, 85% yield). The molecular weights were calculated using the GPC results of the P*t*BOS precursor.

P*p*HS: M_n = 19.5 kg mol^{-1}, M_w = 19.9 kg mol^{-1}, PDI = 1.02; ^{1}H NMR (acetone-d_6, 300 MHz): δ = 1.15 - 1.75 (br m, CH_3), 1.75 - 2.00 (br m, CH), 6.2 - 6.82 (br m, ArH), 7.7 - 8.3 (br s, ArOH) ppm.

4.2.6 Sample preparation

P*p*HS/4-alkylpyridine supramolecular complexes were obtained by dissolving 100 mg P*p*HS homopolymer together with the calculated amount of the desired 4-alkylpyridine in THF so that a 1.5% (w/w) solution was obtained. The clear solution was stirred for 24 h at room temperature and subsequently cast in a Petri dish, which was then placed into an atmosphere saturated with THF so that the solvent was allowed to evaporate slowly. After at least a week of solvent annealing and after all the solvent had evaporated, the Petri dish was heated to 130 °C for 20 min.

4.2.7 Characterization

Gel permeation chromatography (GPC) measurements were performed in dimethylformamide with 0.01M LiBr on a Viscotek GPCMAX equipped with model 302 TDA detectors, using 2 columns (PSS-Gram-1000/30, 10 μm, 30 cm). Molar mass calculations were done using triple detection (lightscattering-, viscosity- and refractive index detector).

^{1}H nuclear magnetic resonance (^{1}H NMR) spectra were recorded on a 300 MHz Varian VXR at room temperature, using $CDCl_3$ or $(CD_3)_2CO$ as solvent.

Attenuated total reflection (ATR) infrared measurements were performed using a Specac Golden Gate accessory with heated diamond top-plate on a Bruker IFS88 spectrometer equipped with a MCT-A detector at resolution 4 cm^{-1}.

Differential scanning calorimetry was performed using a DSC Q1000 (TA Instruments) by heating the samples to 130 °C and cooling to -20 °C at a rate of 5 °C min^{-1}. The second cycle (cooling) was used for data analysis.

Simultaneous small-angle X-ray scattering (SAXS) and wide-angle X-ray scattering (WAXS) measurements were performed at the Dutch-Belgian Beamline (DUBBLE) station BM26B of the European Synchrotron Radiation Facility (ESRF) in Grenoble (France).[27-29] The sample-to-detector distance was ca. 2 m with a wavelength of 1.033 Å. A Dectris-Pilatus 1M detector with a resolution of 981 × 1043 pixels and a pixel size of 172 × 172 μm has been employed to record the 2D-SAXS scattering patterns. A Dectris-Pilatus 300K-W detector with a resolution of 1475 x 195 pixels and a pixel size of 172 × 172 μm has been employed to record the 2D-WAXS scattering patterns. Standard corrections for sample absorption and background subtraction have been performed. The data were normalized with respect to the incident beam intensity in order to correct for primary beam intensity fluctuations. The scattering patterns from silver behenate (AgBe) were used for the calibration of the wave vector scale of the scattering curve. The scattering vector q is defined as $q = (4\pi/\lambda)\ sin\ \theta$, where θ is half of the scattering angle. The SAXS- and WAXS intensity profiles were acquired as function of temperature during cooling from the melt with 5 °C·min^{-1} from 120 °C to 0 °C using an acquisition time of 30 s for each frame.

Additional SAXS measurements were performed using a Bruker NanoStar instrument. A ceramic fine-focus X-ray tube, powered with a Kristalloflex K760 generator at 35 kV and 40 mA, has been used in point focus mode. The primary X-ray flux is collimated using cross coupled Göbel mirrors and a pinhole of 0.3 mm in diameter providing a Cu K_α radiation beam with a full width at half-maximum of about 0.4 mm at the sample position. The sample-detector distance was ca. 0.64 m. The scattering intensity was registered by a Hi-Star position-sensitive area detector (Siemens AXS) in the q-vector range of 0.1 - 2.0 nm. The SAXS intensity profiles were acquired at specific temperatures. The samples were kept 2 min at each temperature before a measurement of 30 min was started.

4.3 Results and discussion

4.3.1 Synthesis of alkyl iodides

The alkyl iodides **2**, hexadecyl iodide, octadecyl iodide, and eicosyl iodide, were synthesized via substitution of the hydroxide functionality of the corresponding primary alcohols **1** with an iodide group using iodine, triphenylphosphine, and imidazole, as described in literature.[30-32] During the first part of the reaction the iodine-PPh_3 complex is formed, after which imidazole and the alcohol **1** are added. Imidazole is added both to catalyze the reaction and to neutralize the hydroiodic acid (HI) that is formed during the reaction. Figure 4.1 presents the typical ^{1}H NMR spectra of a primary alcohol (a), a crude alkyl iodide (b) and a purified alkyl iodide (c). The chemical shift at 3.64 and 1.57 ppm of the protons on the two carbon atoms next to the hydroxyl group (Figure 4.1a) shift after the reaction to 3.19 and 1.82 ppm, respectively (Figures 4.1b and 4.1c), indicating the successful formation of the alkyl iodide.

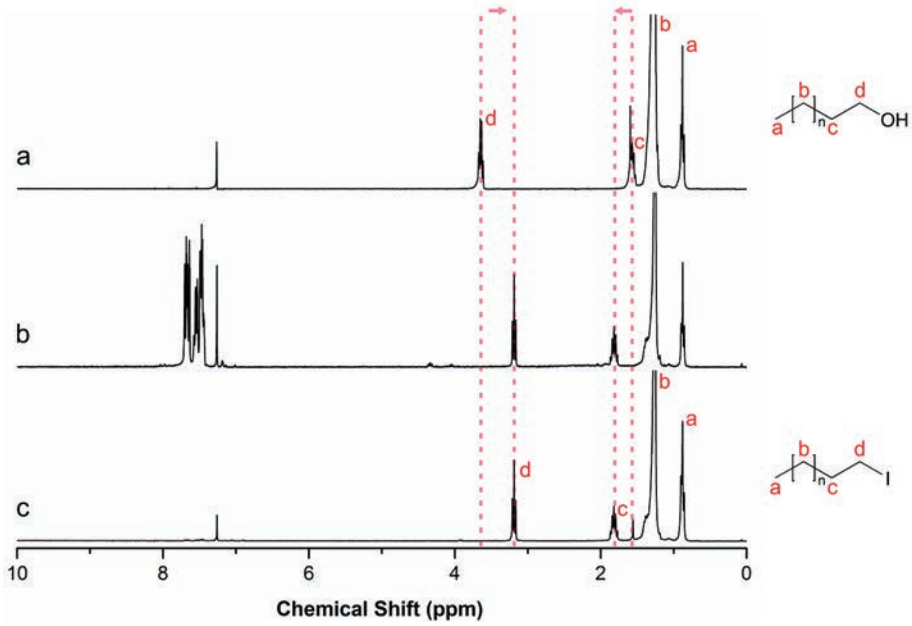

Figure 4.1 Representative ^{1}H NMR spectra of a primary alcohol (a), a crude alkyl iodide (b), and a purified alkyl iodide (c) (solvent: $CDCl_3$).

The chemical shift from the aromatic protons between 7.4 - 7.7 ppm (Figure 4.1b) indicates that there is a large quantity of Ph_3PO present in the crude alkyl iodide. Since Ph_3PO is poorly soluble in non-polar solvents in which alkyl iodides readily dissolve, hexane was used to extract the alkyl iodides from the crude product. Evaporation of hexane resulted in the pure alkyl iodides as product (Figure 4.1c) in good yield (yields above 90%).

To further confirm that all the starting material had reacted, FTIR was used. Figure 4.2 presents a typical FTIR-spectrum of the alcohol starting material (a) and the purified alkyl iodide (Figure 4.2b). The characteristic band of the vibration of the hydroxyl functional group, 3100 - 3700 cm^{-1}, has disappeared completely in the FTIR-spectrum of the product, confirming the complete reaction of the starting material.

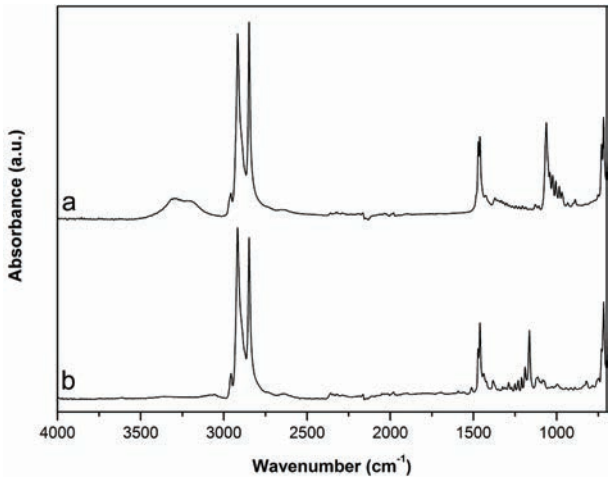

Figure 4.2 Representative infrared spectra recorded at room temperature of a primary alcohol (a) and a purified alkyl iodide (b).

4.3.2 Synthesis of 4-alkylpyridine amphiphiles

The 4-alkylpyridine amphiphiles **3**, 4-heptadecylpyridine (HDPy), 4-nonadecylpyridine (NDPy), and 4-heneicosylpyridine (HEPy), were synthesized via substitution of the iodide functionality of the corresponding alkyl iodide **2** with 4-picoline as described by Hulst et al.[33] During the first part of the reaction the base

lithium diisopropylamine (LDA) is formed via the abstraction of the most acidic proton of diisopropylamine using *n*-BuLi. According to the literature this step can be done at 0 °C,[33] but it was decided to do this step at -50 °C in order to prevent the solvent THF to act as an acid. Subsequently, 4-picoline is added to the reaction mixture upon which the most acidic proton of 4-picoline, located at the methyl position since the formed anion can be stabilized via resonance, is abstracted by LDA. Finally, the alkyl iodide is added to the reaction mixture. A S_N2 substitution reaction will take place in which the iodo functionality (a very good leaving group) of the alkyl iodide is substituted by the 4-picoline anion (very strong nucleophile) formed in the previous step.

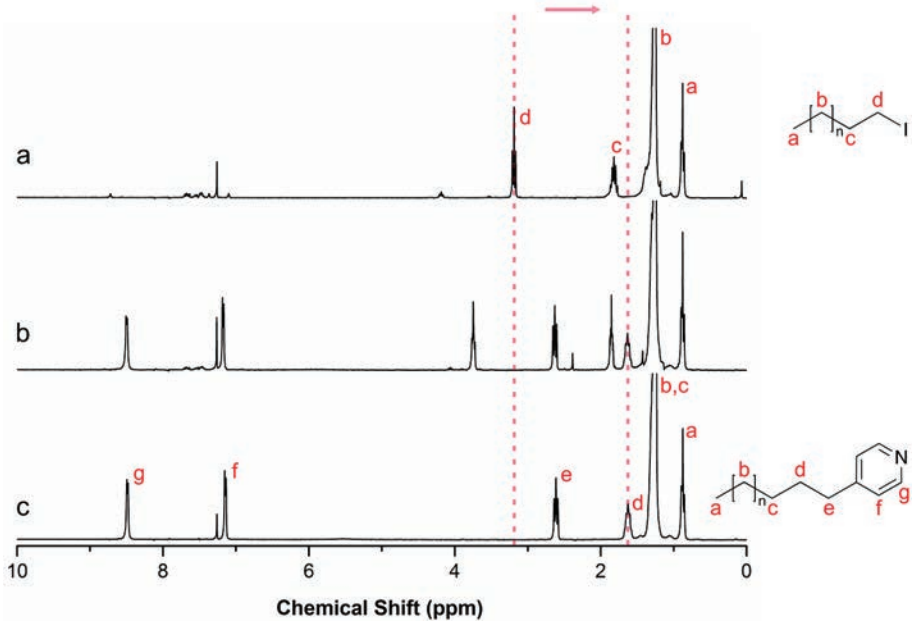

Figure 4.3 Representative ^{1}H NMR spectra of an alkyl iodide (a) and 4-alkylpyridine before (b) and after (c) purification (solvent: $CDCl_3$).

The ^{1}H NMR spectra of the alkyl iodide substrate together with the product obtained after the reaction are shown in Figures 4.3a and 4.3b, respectively. The chemical shift at 3.19 ppm, originating from the protons on the carbon next to the iodide, shifts to 1.62 ppm in the product. Furthermore, the protons of the methyl group of 4-picoline

having a chemical shift at 2.35 ppm (spectrum not shown) which shifts to 2.61 ppm in the product. Both shifts, together with the appearance of the chemical shifts at 8.49 and 7.14 ppm of the protons of the pyridine group, indicate a successful coupling of the alkyl iodide to the methyl group of 4-picoline resulting in a 4-alkylpyridine amphiphile **3**. As can be seen in Figure 4.3b, the product still contains a lot of impurities after the reactions. To purify the product a method described by Bizzotto et al. was used.[34] This method uses the basic character of the nitrogen atom in the 4-alkylpyridine by protonating the position using a strong acid like hydrochloric acid. The hydrochloric salt that is obtained can be recrystallized and washed with non-polar solvents in order to remove any impurities. Finally, the proton is abstracted again using a strong base like sodium hydroxide, resulting in a purified product (Figure 4.3c). Although the described purification works very well, the yield is reasonably low (yields around 45%).

4.3.3 Synthesis of P*p*HS homopolymer

P*p*HS homopolymer was prepared through a living anionic polymerization of P*t*BOS homopolymer followed by hydrolysis of the *tert*-butoxy group. A lot of research has been conducted on the synthesis of protected hydroxystyrene via living anionic polymerization.[35-37] In order to obtain P*p*HS with a narrow polydispersity, protection of the phenol groups prior to anionic polymerization is required, to avoid termination of the living chain ends. Therefore, *tert*-butoxystyrene was used since it is commercially available and the *tert*-butyl ether can be hydrolyzed under relative mild conditions. P*t*BOS homopolymer was successfully synthesized and the results from GPC analysis are presented in Table 4.1.

Table 4.1 Molecular characteristics of the P*t*BOS and P*p*HS homopolymers.

	M_n [a] (kg mol^{-1})	M_w [a] (kg mol^{-1})	PDI [a]
P*t*BOS	28.5 [a]	29.0 [a]	1.02 [a]
P*p*HS	19.5 [b]	19.9 [b]	1.02 [a]

[a] Determined by GPC (DMF). [b] Calculated on the basis of the P*t*BOS precursor.

Figure 4.4 shows the GPC chromatogram of P*t*BOS, indicating a narrow molecular weight distribution. The polydispersity index (PDI) value, determined by universal calibration, is 1.02.

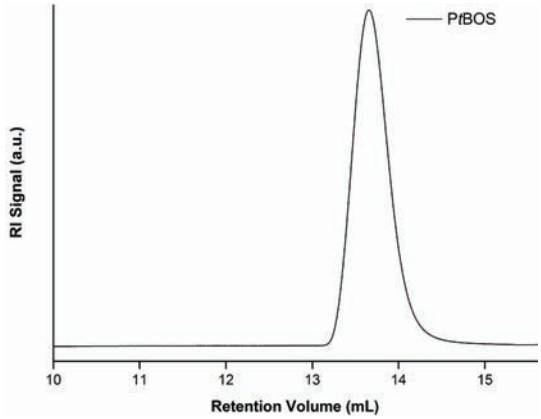

Figure 4.4 GPC chromatogram of the P*t*BOS homopolymer.

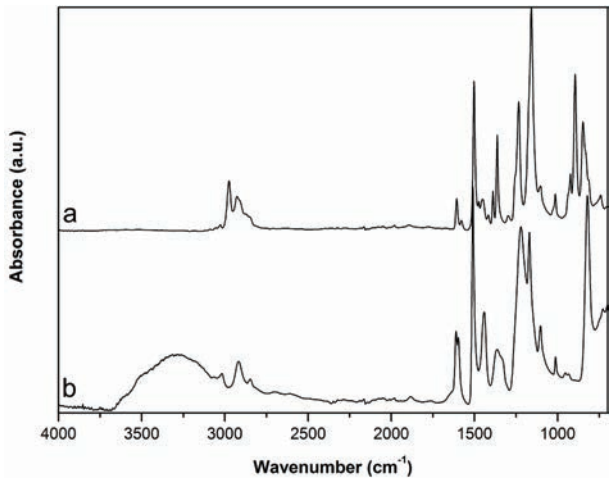

Figure 4.5 Infrared spectra recorded at room temperature of P*t*BOS (a) and P*p*HS (b).

Hydrolysis of the *tert*-butyl ether results in a P*p*HS homopolymer with a M_n of 19.5 kg mol^{-1} (Table 5). The corresponding FTIR spectrum of P*p*HS (Figure 4.5b) after hydrolysis displays a broad peak at 3300 cm^{-1} that is initially absent (Figure 4.5a). This indicates the successful conversion from *tert*-butoxy to hydroxyl groups.

Hydrolysis was also studied using ^{1}H NMR spectroscopy. Figure 4.6 displays the ^{1}H NMR spectra before (a) and after hydrolysis (b). The large chemical shift around 1.31 ppm corresponding to the *tert*-butyl protons in the initial P*t*BOS homopolymer completely disappears in the spectrum of the deprotected P*p*HS homopolymer indicating that the hydrolysis was completed. A broad peak located around 8.0 ppm, corresponding to phenol protons, appears after the acidic cleavage further proving the successful hydrolysis of the ester groups.

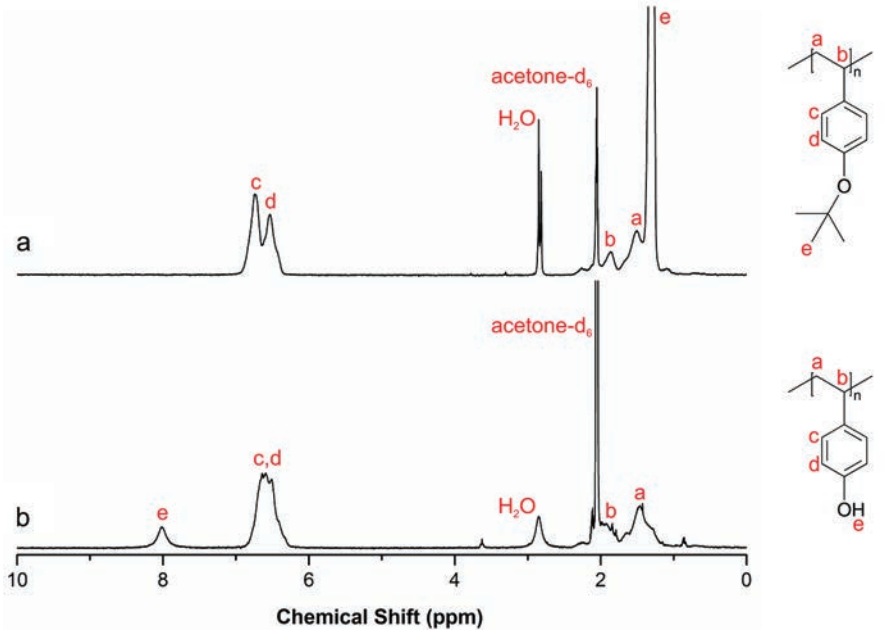

Figure 4.6 ^{1}H NMR spectra of P*t*BOS (a) and P*p*HS (b) (solvent: acetone-d_6).

4.3.4 Supramolecular comb copolymer complex

4.3.4.1 Infrared spectroscopy

The hydrogen-bonded supramolecular complex between poly(*p*-hydroxystyrene) (P*p*HS) and 4-heneicosylpyridine (HEPy), schematically shown in Scheme 4.1, was analyzed using FTIR spectroscopy. FTIR studies of PDP hydrogen-bonded to P4VP containing homopolymers and diblock copolymers show that the most affected bands are the hydroxyl stretching vibrations of PDP around 3360 cm^{-1} and the stretching modes of the pyridine ring of P4VP at 1597, 1415, and 993 cm^{-1}. The broad band around 3360 cm^{-1} is reduced significantly upon formation of the hydrogen-bonded complex. Shifts to higher frequencies are observed for the stretching modes of the pyridine ring reflecting the electronic redistributions caused by the formation of stronger bonds. In the 'mirrored' system, the hydrogen bonds are also formed between pyridine and phenol groups and therefore it is expected that the same shifts can also be observed here.

Figure 4.7 presents the FTIR spectra measured at room temperature of P*p*HS, HEPy, and P*p*HS(HEPy)$_x$, in which the amphiphile mole fraction x is 0.5, 1.0, and 1.5, respectively. The broad band of the hydroxyl stretching vibrations of P*p*HS around 3300 cm^{-1} is clearly visible in the FTIR spectrum of pure P*p*HS. A significant decrease of the hydroxyl stretching band is observed for x = 0.5 indicating a decrease in self-associated hydrogen bonds between the hydroxyl groups of P*p*HS. After increasing x to 1.0 or 1.5 the hydroxyl stretching band disappeared almost completely, indicating that upon mixing of P*p*HS with HEPy the intramolecular hydrogen bonds were broken.

The stretching modes of the pyridine ring of P4VP at 1597, 1415, and 993 cm^{-1} are also visible in the spectra of HEPy at 1601, 1415 and 993 cm^{-1}, respectively. However, the band found at 1601 cm^{-1} cannot be used to prove successful hydrogen-bonding since it is overlapped by two bands at 1610 and 1597 cm^{-1} from P*p*HS, rendering it difficult to analyze. Therefore, only the bands at 1415 and 993 cm^{-1} are used to analyze hydrogen-bonding interactions between the hydroxyl group of P*p*HS and the pyridine group of HEPy. Figure 4.8a presents the scale-expanded FTIR spectra of P*p*HS, HEPy, and P*p*HS(HEPy)$_x$ (x = 0.5, 1.0, and 1.5) in the range 1440-1390 cm^{-1}. Pure HEPy has an absorption band at 1415 cm^{-1}, while P*p*HS shows no absorption in this region.

Since there is no overlapping absorption of P*p*HS, a shift of about +6 cm^{-1} can be clearly observed, indicating the pyridine groups are participating in hydrogen-bonding.[18]

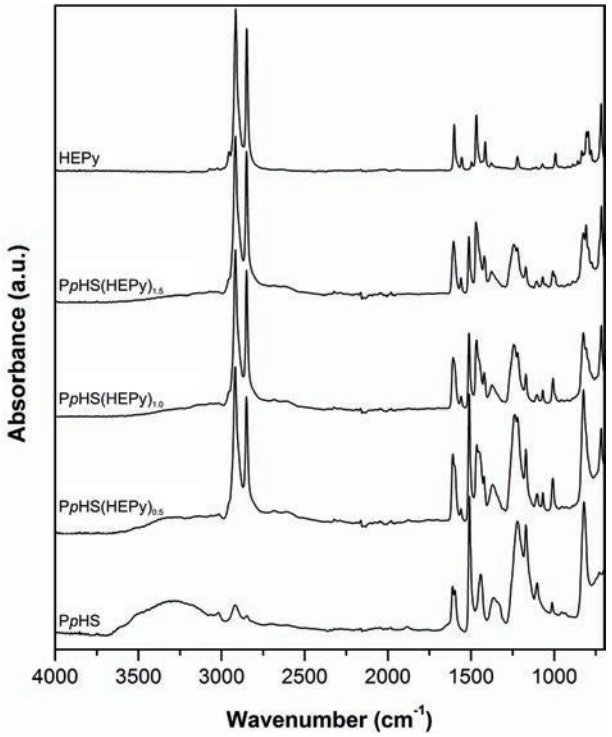

Figure 4.7 Infrared spectra at room temperature of P*p*HS, HEPy, and P*p*HS(HEPy)$_x$ (x = 0.5, 1.0, 1.5).

Figure 4.8b presents the scale-expanded FTIR spectra in the range 1030-970 cm^{-1}. HEPy has an absorption band at 993 cm^{-1} which shifts to 1008 cm^{-1} upon hydrogen-bonding. P*p*HS has an absorption band at 1013 cm^{-1}, partly overlapping the new band at 1008 cm^{-1}. All three P*p*HS(HEPy)$_x$ spectra show that there is hydrogen-bonding between the pyridine group and the hydroxyl group. For x = 0.5 the free pyridine absorption has disappeared completely. However, for x = 1.0 and 1.5 there is also an absorption band visible at wavenumbers slightly higher than 993 cm^{-1}

reflecting the presence of pyridine groups which are not hydrogen-bonded. For x = 1.5 this is as expected since there are more pyridine groups than hydroxyl groups. A small number of free pyridine groups for x = 1.0 simply reflects the reversibility of the hydrogen-bonding. For the reversed P4VP(PDP)$_{1.0}$ system free pyridine groups are not clearly observed.[18] Apparently the competition with the self-associated P*p*HS hydrogen-bonding reduces the P*p*HS-HEPy hydrogen-bonding somewhat compared to the P4VP-PDP system.

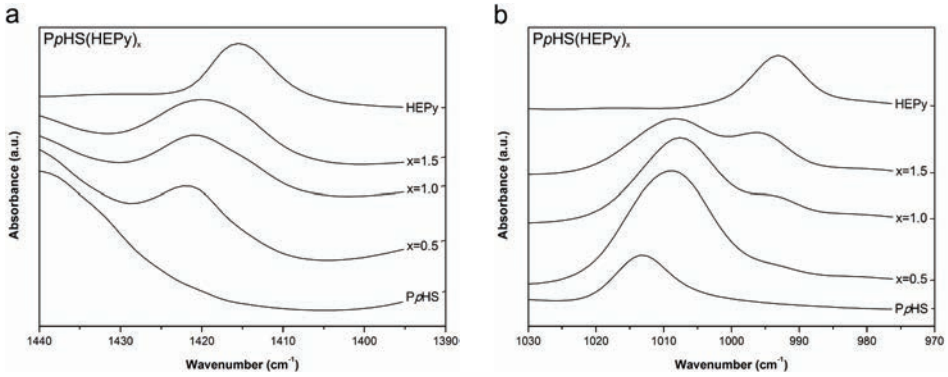

Figure 4.8 Infrared spectra at room temperature of PpHS, HEPy, and P*p*HS(HEPy)$_x$ (x = 0.5, 1.0, 1.5) in the 1440-1390 cm^{-1} region (a) and the 1030-970 cm^{-1} region (b).

To study the effect of temperature on the hydrogen-bonding FTIR spectra as function of temperature were recorded. First, the behavior of the pure components was investigated. Figure 4.9 presents the scale-expanded FTIR spectra at different temperatures in the range 1440 - 1390 cm^{-1} (a) and 1030 - 970 cm^{-1} (b) for HEPy. In both regions shown there is a very slight shift of the bands to lower frequencies visible, 1415 cm^{-1} at 25 °C to 1413 cm^{-1} at 190 °C and 993 cm^{-1} at 25 °C to 992 cm^{-1} at 190 °C indicating a slight weakening of the bonds at higher temperatures.
For P*p*HS no shift is observed in both regions when the temperature is increased, as can be seen in Figure 4.10.

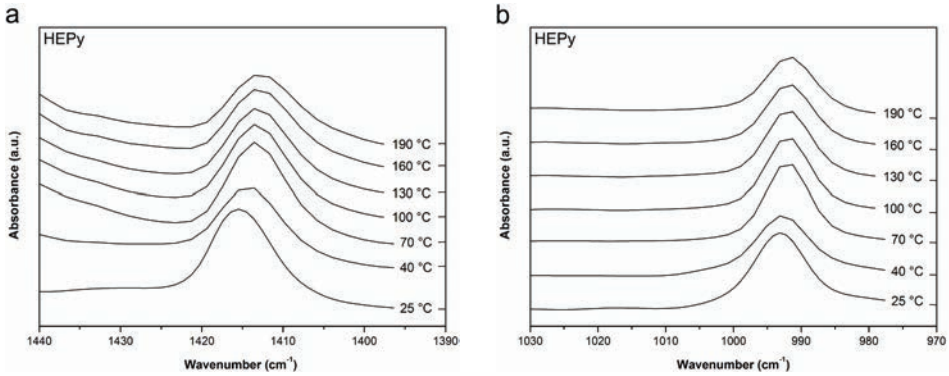

Figure 4.9 Infrared spectra at different temperatures of HEPy in the 1440-1390 cm^{-1} region (a) and the 1030-970 cm^{-1} region (b).

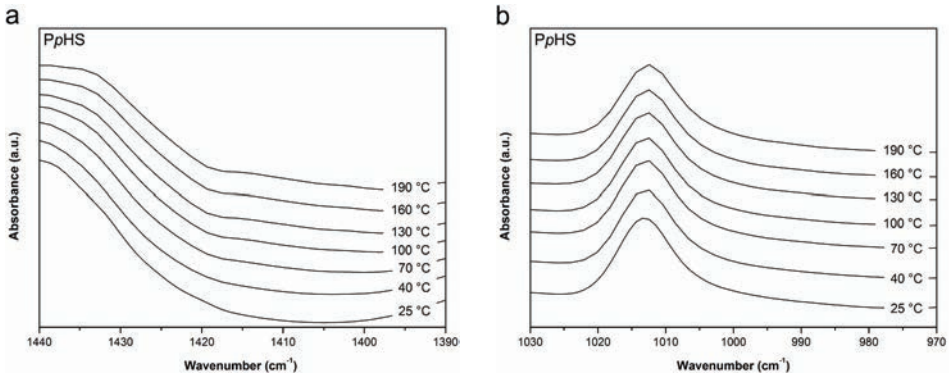

Figure 4.10 Infrared spectra at different temperatures of P*p*HS in the 1440-1390 cm^{-1} region (a) and the 1030-970 cm^{-1} region (b).

Figure 4.11 presents the FTIR spectra obtained during temperature scans from 25 °C up to 190 °C for P*p*HS(HEPy)$_x$ complexes. In the region between 1440 - 1390 cm^{-1} (Figures 4.11a, c, e) all spectra show a decrease in intensity of the band around 1421 cm^{-1} when the temperature is increased and a gradual increase in intensity of the band at 1415 cm^{-1} above 100 °C. The band at 1415 cm^{-1} is already more pronounced at lower temperatures for higher amphiphile mole fractions. This is caused by the increased amount of free pyridine already present in the system. However, when

looking closely to the spectra of x = 1.0 and x = 1.5 there is a small band at 1421 cm^{-1} visible at elevated temperatures corresponding to the hydrogen-bonded alkylpyridines. In the region between 1030 - 970 cm^{-1} (Figures 4.11 b, d, f) the band at 1008 cm^{-1} decreases in intensity above 100 °C in all spectra and shifts to 1005 cm^{-1}. For x = 0.5 a band at 993 cm^{-1} is becoming visible at 40 °C. When the temperature is increased further, the band increases in intensity and shifts to 992 cm^{-1} as was also observed in the FTIR spectra for pure HEPy. For x = 1.0 and 1.5 a band at 993 and 996 cm^{-1} respectively, is already present at room temperature reflecting the presence of free alkylpyridine in the system. In both cases there is a shift to 992 cm^{-1} upon heating to 40 °C and the band increases in intensity at higher temperatures.

To obtain a direct comparison of the different amphiphile mole fractions at specific temperatures, the spectra of P*p*HS, P*p*HS(HEPy)$_x$, and HEPy at 40, 100, and 190 °C are presented in Figure 4.12. The region between 1440 - 1390 cm^{-1} at 40, 100 and 190 °C is presented in Figures 4.12a, c, e, respectively. At 40 °C virtually all the pyridine is still hydrogen-bonded for x = 0.5 since there is only a band at 1421 cm^{-1}. For x = 1.5 there is a band visible at 1414 cm^{-1} reflecting the presence of free amphiphiles. For x = 1.0 the band at 1414 cm^{-1} is hardly visible. At 100 °C the intensity of the band at 1414 cm^{-1} is increasing for al mole fractions although it is still hardly visible for x = 0.5. While the band at 1414 cm^{-1} is increasing, the band at 1421 cm^{-1} is decreasing in intensity. When heated to 190 °C there is almost no band visible at 1421 cm^{-1} while there is a band at 1413 cm^{-1} for the free pyridine ring.

The region between 1030 - 970 cm^{-1} at 40, 100 and 190 °C is presented in Figures 4.12b, d, f, respectively. At 40 °C for all three amphiphile mole fractions a band is clearly visible around 1006 cm^{-1} while a band at 993 cm^{-1} indicates the presence of free pyridine. When increasing the temperature the band at 1006 cm^{-1} decreases and the band at 993 cm^{-1} increases and shifts to 992 cm^{-1}.

The results presented in Figure 4.11 and Figure 4.12 clearly show that the hydrogen-bonding of alkylpyridine amphiphiles to the polymer backbone is quite stable up to temperatures of about 100 °C and is only slowly decreasing when the temperature is increased further.

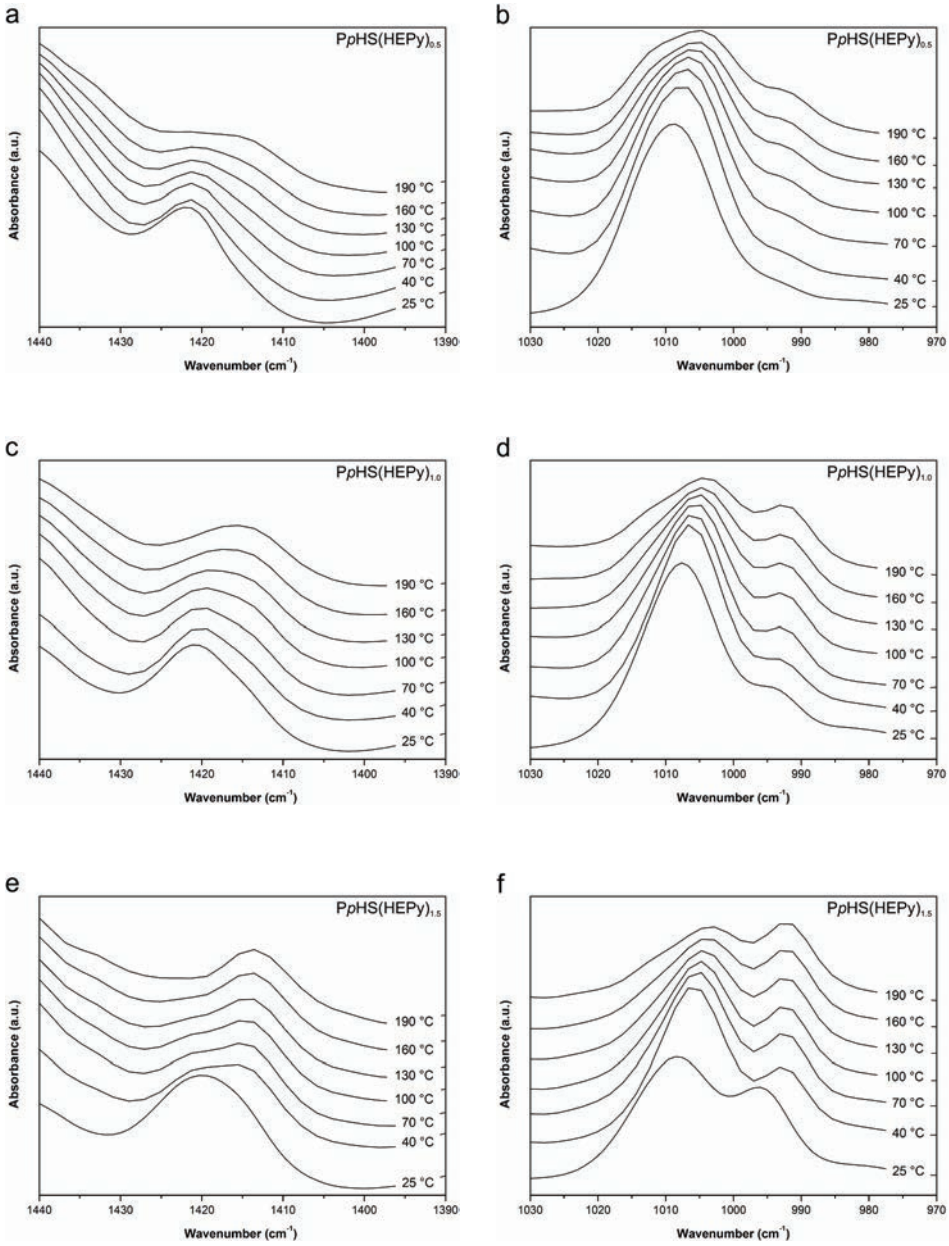

Figure 4.11 Infrared spectra at different temperatures of P*p*HS(HEPy)$_x$ (x = 0.5, 1.0, 1.5) in the 1440-1390 cm^{-1} region (a, c, and e) and the 1030-970 cm^{-1} region (b, d, and f).

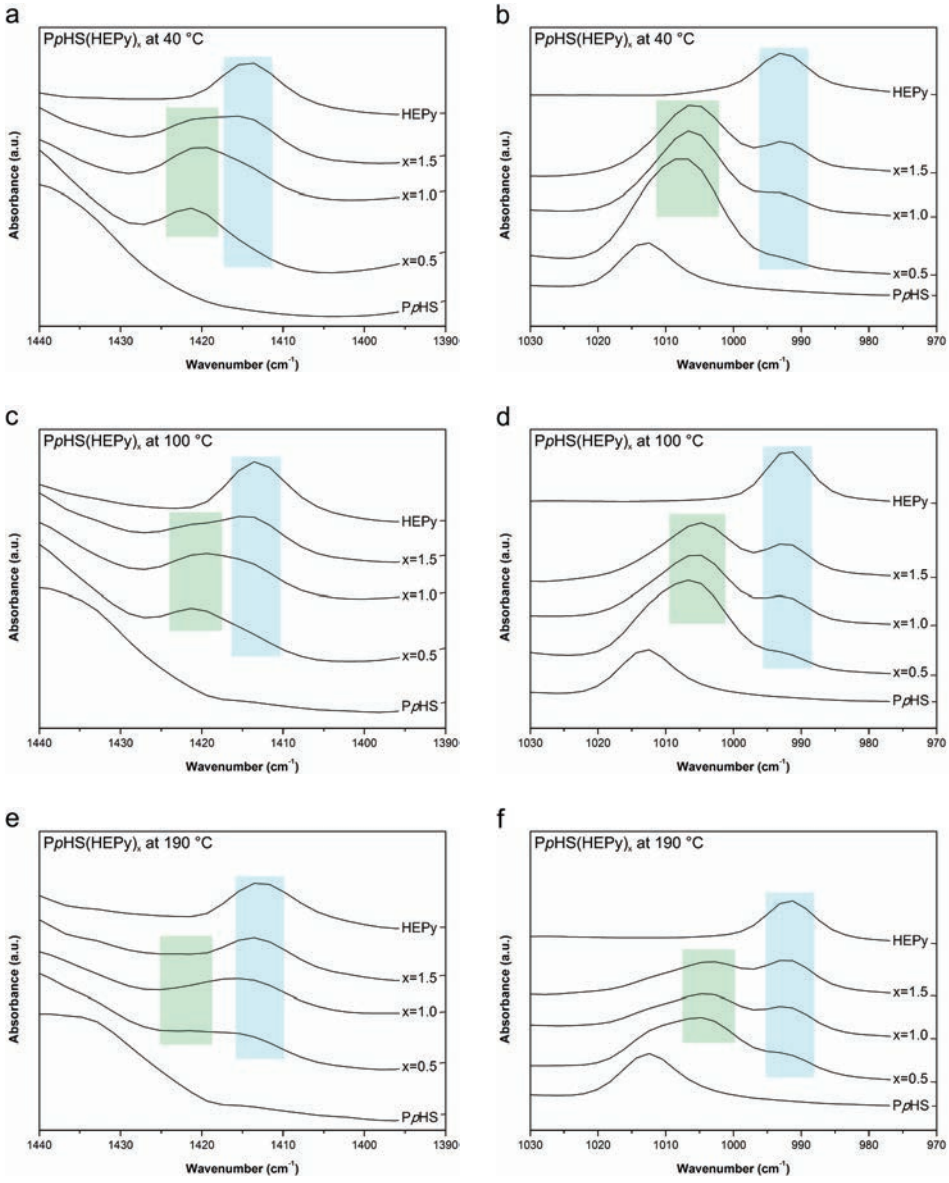

Figure 4.12 Infrared spectra of P*p*HS(HEPy)$_x$ (x = 0.5, 1.0, 1.5) in the 1440-1390 cm^{-1} region and the 1030-970 cm^{-1} region recorded at 40 °C (a and b), 100 °C (c and d), 190 °C (e and f). The bands originating from the pyridine ring of the hydrogen-bonded alkylpyridines are marked green, while the bands of the free pyridine ring are marked blue.

4.3.4.2 Differential scanning calorimetry

The DSC thermograms of the P*p*HS/4-alkylpyridine complexes were recorded during cooling from the melt with 5 °C min^{-1} from 120 °C to -10 °C after keeping the samples at 130 °C for 5 min. The results are presented in Figure 4.13 and an overview of all the crystallization temperatures (T_c) is listed in Table 4.2.

The observed crystallization temperatures of P*p*HS(HDPy)$_{1.0}$, P*p*HS(NDPy)$_{1.0}$, and P*p*HS(HEPy)$_{1.0}$ are 3.7 °C, 22.3 °C, and 34.5 °C, respectively. Increasing the length of the alkyl tail of the 4-alkylpyridine, results in crystallization at a higher temperature, as expected. The values of P*p*HS(NDPy)$_{1.0}$ and P*p*HS(HEPy)$_{1.0}$ supramolecular complexes are similar to the crystallization temperatures of pure NDPy (T_c = 22.7 °C) and HEPy (T_c = 33.0 °C) indicating that the alkyl tails are phase separated from the polymer backbone. In contrast, P*p*HS(HDPy)$_{1.0}$ has a significantly lower crystallization temperature compared to pure HDPy which crystallizes at 14.9 °C. The lowering of the T_c for this supramolecular complex is an indication that in this case the shorter alkyl tails are still mixed with the polymer backbones when the crystallization occurs, i.e., melting point depression.

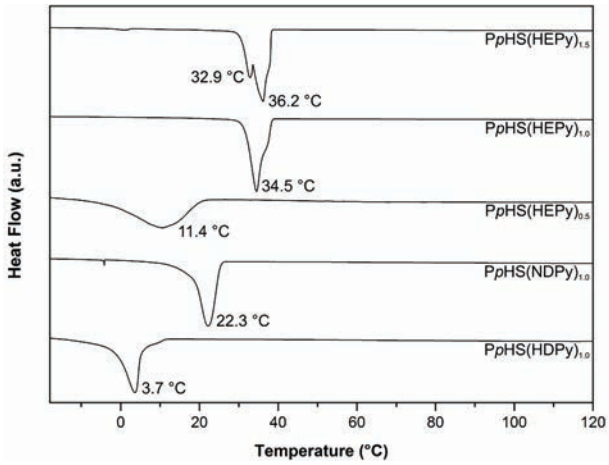

Figure 4.13 DSC thermograms recorded during cooling at 5 °C min^{-1} of P*p*HS(HDPy)$_{1.0}$, P*p*HS(NDPy)$_{1.0}$, P*p*HS(HEPy)$_{0.5}$, P*p*HS(HEPy)$_{1.0}$, and P*p*HS(HEPy)$_{1.5}$. The corresponding T_c is displayed next to each transition.

Variation of x in P*p*HS(HEPy)$_x$ results in two distinctly different thermograms for x = 0.5 and 1.5 compared to x = 1.0. The thermogram of P*p*HS(HEPy)$_{0.5}$ shows a broad crystallization peak centered around 11.4 °C, which is significantly lower and broader than the crystallization peak observed for P*p*HS(HEPy)$_{1.0}$ at 34.5 °C. The lower T_c of the alkyl tails of P*p*HS(HEPy)$_{0.5}$ is also an indication for the absence of a phase separated morphology. The broadening of the peak is due to the difference in composition throughout the sample. In contrast, the thermogram of P*p*HS(HEPy)$_{1.5}$ shows two maxima during crystallization. This can be explained by the amount of the 4-alkylpyridine amphiphile in the system, which is much more than can be hydrogen-bonded to P*p*HS. This excess of HEPy can macrophase separate from the supramolecular complex and therefore have a slightly different T_c.

Table 4.2 Crystallization temperatures of the 4-alkylpyridines and the P*p*HS/4-alkylpyridine supramolecular complexes.

Sample	T_c [a] (°C)
HDPy	14.9
P*p*HS(HDPy)$_{1.0}$	3.7
NDPy	22.7
P*p*HS(NDPy)$_{1.0}$	22.3
HEPy	33.0
P*p*HS(HEPy)$_{0.5}$	11.4
P*p*HS(HEPy)$_{1.0}$	34.5
P*p*HS(HEPy)$_{1.5}$	32.9; 36.2[b]

[a] Determined by DSC measurement in which the maximum of the exothermic peak is presented as T_c. [b] The two values represent the two maxima found in the crystallization peak of P*p*HS(HEPy)$_{1.5}$.

In all the supramolecular complexes no signal corresponding to a separate ODT becomes visible at higher temperatures in contrast to what is observed for P4VP(PDP)$_x$ supramolecular complexes.[11] Apparently, in the P*p*HS/4-alkylpyridine systems ordering and crystallization of the alkyl side chains occur simultaneously.

4.3.4.3 Small angle X-ray scattering

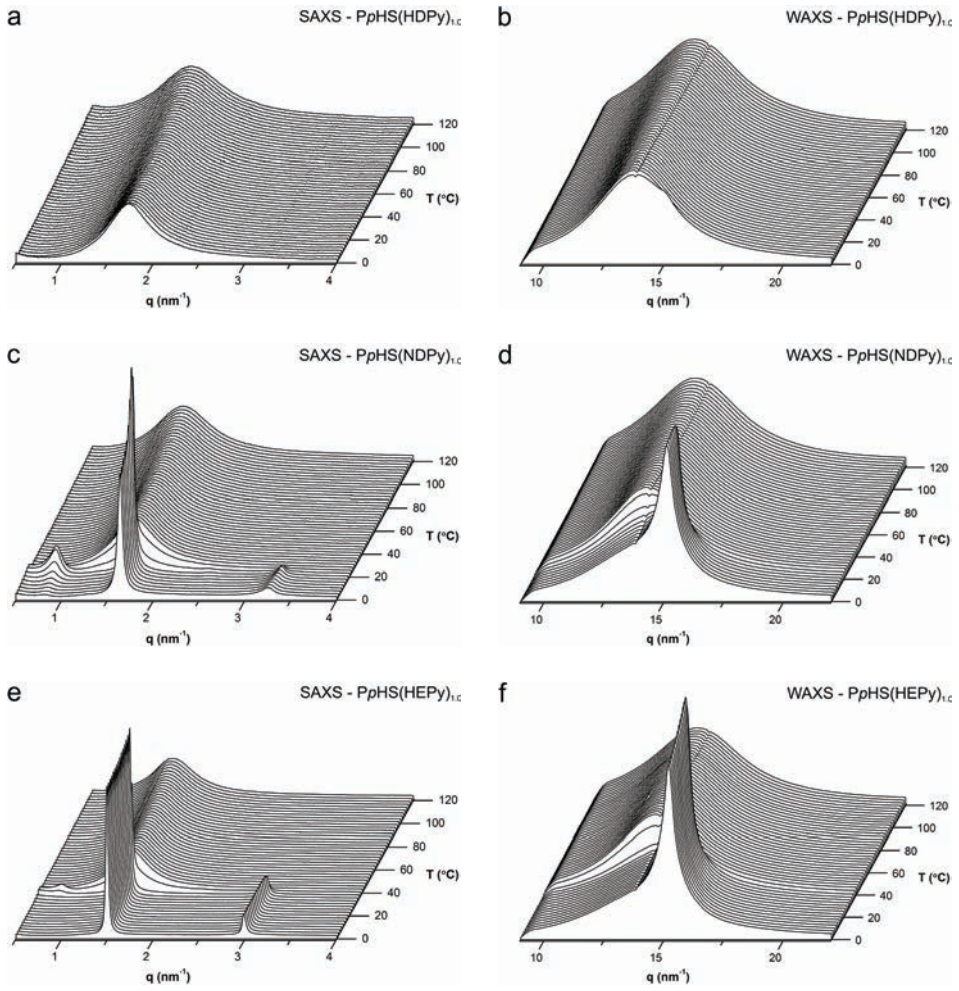

Figure 4.14 SAXS and WAXS intensity profiles of P*p*HS(HDPy)$_{1.0}$ (a, b), P*p*HS(NDPy)$_{1.0}$ (c, d), and P*p*HS(HEPy)$_{1.0}$ (e, f) during cooling with 5 °C min^{-1} from the melt at 120 °C.

Simultaneous SAXS and WAXS measurements were used to investigate the self-assembly of the P*p*HS/4-alkylpyridine systems in more detail. Figure 4.14 presents the SAXS (Figures 4.14a, c, e) and WAXS (Figures 4.14b, d, f) intensity profiles as

function of temperature during cooling from the melt with 5 °C min^{-1} from 120 °C to 0 °C for P*p*HS(HDPy)$_{1.0}$, P*p*HS(NDPy)$_{1.0}$ and P*p*HS(HEPy)$_{1.0}$, respectively.

The SAXS intensity profile obtained during a temperature scan for P*p*HS(HDPy)$_{1.0}$, given in Figure 4.14a, show no ODT nor is a self-assembled structure formed due to crystallization of the amphiphiles. Only a characteristic correlation hole peak is present. The absence of a peak of the crystallized alkyl tails of HDPy in the WAXS (Figure 4.14b) further supports this observation.

The SAXS and WAXS intensity profiles of P*p*HS(NDPy)$_{1.0}$ and P*p*HS(HEPy)$_{1.0}$ (Figures 14.4c to 14.4f) show a clearly different result. In both cases an ordered state is formed with SAXS scattering peaks in the ratio 1:2 indicating a lamellar structure and WAXS peaks indicating crystallization. Since WAXS and SAXS peaks occur at the same temperature, the crystallization of the hydrocarbon tails of the amphiphiles occurs together with the ODT to a lamellar structure. This is quite different from the P4VP/3-alkyl phenol systems (e.g., pentadecylphenol and nonadecylphenol), where an ODT to an ordered melt state occurs on cooling at elevated temperatures well above the alkyl tail crystallization temperatures. We believe that this difference must somehow be related to the hydrogen-bonding of the P*p*HS polymers, thereby reducing the number of hydrogen bonds between P*p*HS and 4-alkylpyridine in the mixture.

In both the SAXS intensity profiles of P*p*HS(NDPy)$_{1.0}$ and P*p*HS(HEPy)$_{1.0}$ in Figures 4.14c and 4.14e an extra peak appears at half the q value compared to the main peak. For P*p*HS(NDPy)$_{1.0}$ there is even a very weak scattering peak at q = 2.5 nm^{-1} visible when a logarithmic scale is used. This third order peak disappears when the first order peak becomes less intense at lower temperatures. The presence of a scattering peak at half the q-value of the main peak indicates the presence of a larger length scale. This may be caused by the alkyl chains that organize into an end-to-end double-layer structure as opposed to the interdigitating one-layer structure mainly formed (Figure 4.15).[19]

The end-to-end double layer structure disappears in both cases at temperatures below the crystallization temperature, indicating that there is still enough mobility for these chains to rearrange into a preferred interdigitating one-layer lamellar morphology. The end-to-end double layer structure is always observed for P*p*HS(NDPy)$_{1.0}$, but not for P*p*HS(HEPy)$_{1.0}$ where it depends strongly on the cooling rate. To see this effect in more detail, two new samples were measured at very low cooling rates. Figure 4.16a

and 4.16b show the SAXS intensity profiles for a temperature scan of P*p*HS(NDPy)$_{1.0}$ (25 °C → 35 °C → 25 °C) and of P*p*HS(HEPy)$_{1.0}$ (35 °C → 50 °C → 35 °C). The samples were kept 2 min at each temperature before a measurement was started. The measuring time at each temperature was 30 min. The observed T_c's are higher compared to the ones found in Figure 4.14 reflecting the decrease in the cooling rate. Figure 4.16a shows that the new P*p*HS(NDPy)$_{1.0}$ sample has only a very small peak indicating the presence of a larger length scale. Mainly an interdigitated one-layer structure is present. However, after cooling down from the melt, to remove the thermal history, a second peak at a lower q value is appearing indicating the formation of an end-to-end double layer structure. Figure 4.16b shows that at these very low cooling rates P*p*HS(HEPy)$_{1.0}$ is only forming an interdigitating one-layer structure even after cooling down from the melt.

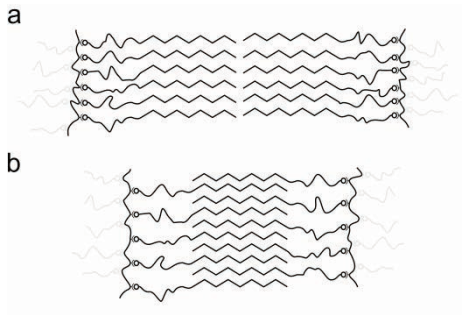

Figure 4.15 Schematic representation of the end-to-end double-layer structure (a) and the interdigitating one-layer structure (b).

The domain spacing d of the lamellar morphology for P*p*HS(NDPy)$_{1.0}$ is 7.7 nm when the end-to-end double layer is formed and 3.8 nm when the interdigitated lamellar morphology is formed. The interdigitated lamellar morphology of P*p*HS(HEPy)$_{1.0}$ has a domain spacing of 4.2 nm. The increase in size of the interdigitating structures of P*p*HS(HEPy)$_{1.0}$ compared to P*p*HS(NDPy)$_{1.0}$ nicely reflects the longer alkyl tail of HEPy compared to NDPy.

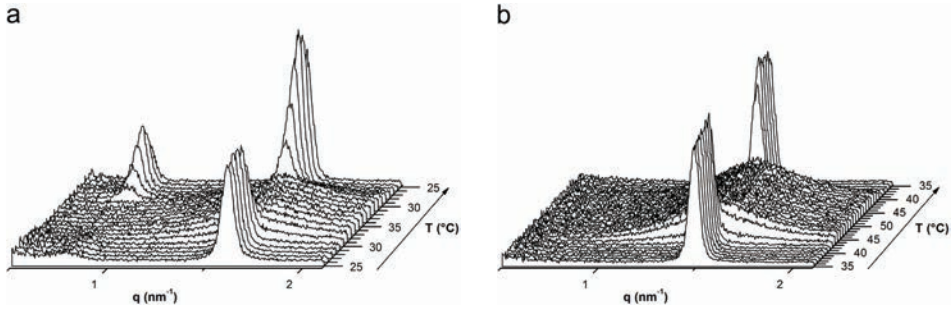

Figure 4.16 SAXS intensity profiles of P*p*HS(NDPy)$_{1.0}$ (a) and P*p*HS(HEPy)$_{1.0}$ (b) during a heat-cool cycle in which each frame was measured over a 30 min time interval in order to observe the influence of cooling speed on the formation of the end-to-end double layer structure.

To investigate the influence of the amphiphile mole fraction on the structure formed, SAXS and WAXS intensity profiles of P*p*HS(HEPy)$_x$ (x = 0.5, 1.0, and 1.5) were recorded. The SAXS and WAXS intensity profiles as function of temperature during cooling from the melt with 5 °C min^{-1} from 120 °C to 0 °C are presented in Figure 4.17. For P*p*HS(HEPy)$_{0.5}$, as confirmed by IR spectroscopy, the system is hydrogen-bonded and a correlation hole peak is visible in the SAXS intensity profile (Figure 4.17a). At lower temperatures the correlation hole peak shifts slightly to higher q values, but there is no self-assembled lamellar structure formed. Also in the WAXS intensity profile of P*p*HS(HEPy)$_{0.5}$ there is no peak due to the crystallization of the alkyl tails of the HEPy (Figure 4.17b).

The SAXS and WAXS intensity profiles of P*p*HS(HEPy)$_{1.0}$ were already presented in Figures 4.14c and 4.14d but are shown again in Figures 4.17c and 4.17d in order to compare the results directly with P*p*HS(HEPy)$_{0.5}$ and P*p*HS(HEPy)$_{1.5}$ (Figures 4.17d, e). Both x = 1.0 and 1.5 show identical intensity profiles in which the crystallization of the amphiphiles occurs at ca. 37 °C. The first and second order diffraction peaks of P*p*HS(HEPy)$_{1.5}$ are at slightly higher q values compared to P*p*HS(HEPy)$_{1.0}$, indicating a small decrease in the domain spacing of the lamellar morphology for x = 1.5; P*p*HS(HEPy)$_{1.0}$: d = 4.2 nm, P*p*HS(HEPy)$_{1.5}$: d = 4.1 nm. To accommodate the extra alkylpyridine in the lamellar morphology the polymer backbone extends itself and thus decreasing the long period (Figure 4.18).[38]

Furthermore, a very weak extra scattering peak and its second order peak can be seen in Figure 4.17e at q' = 1.86 nm^{-1} and 2q' = 3.72 nm^{-1}, respectively. This corresponds to a lamellar morphology with a domain spacing of d' = 3.4 nm. In the WAXS intensity profile there is also a scattering peak appearing at a larger q value than the main one supporting the SAXS result (Figure 4.17f).

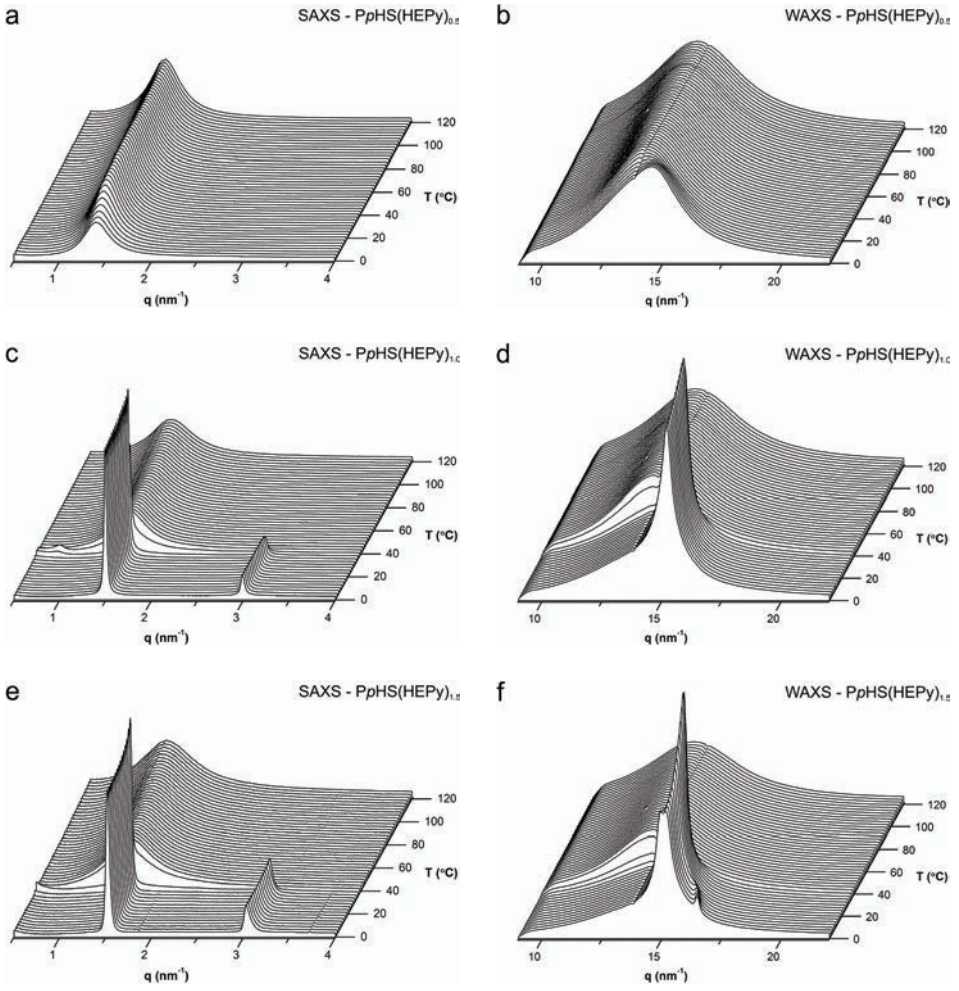

Figure 4.17 SAXS and WAXS intensity profiles of P*p*HS(HEPy)$_{0.5}$ (a, b), P*p*HS(HEPy)$_{1.0}$ (c, d), and P*p*HS(HEPy)$_{1.5}$ (e, f) during cooling with 5 °C min^{-1} from the melt at 120 °C.

The appearance of the extra scattering peaks suggests that there are areas present in the system in which non-hydrogen-bonded HEPy amphiphiles are forming separate lamellar structures after crystallization. This is in contrast with P4VP-PDP systems in which an excess of PDP is added, e.g., P4VP(PDP)$_{1.5}$, in which an interdigitated state is formed in such a way that there are phenol groups in the middle of the crystalline layer.[19] However, in the case of PDP there is intermolecular hydrogen-bonding between the phenol groups of PDP in the middle of this crystalline layer governing the formation of such a structure. The fact that this is not observed in P*p*HS(HEPy)$_{1.5}$ is due to the absence of the possibility of hydrogen-bonding.

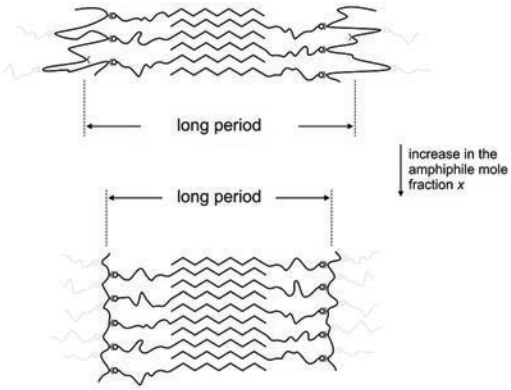

Figure 4.18 Schematic representation of the decrease in domain spacing due to the extending of the polymer backbone to accommodate the extra alkylpyridine.

4.4 Conclusion

Anionic polymerization of *t*BOS followed by hydrolysis of the *tert*-butoxy group resulted in a P*p*HS homopolymer with a molecular weight of 19.5 kg mol^{-1}. Three different 4-alkylpyridine amphiphiles were synthesized by first converting primary alcohols to alkyl iodides and subsequently coupling the alkyl iodides to 4-picoline. Via this route, 4-heptadecylpyridine (HDPy), 4-nonadecylpyridine (NDPy) and 4_heneicosylpyridine (HEPy) were synthesized successfully.

The formation of a hydrogen-bonded complex between 4-alkylpyridines and P*p*HS was followed via FTIR. The disappearance of the band at 3300 cm^{-1} and the shifts of the bands at 1415 cm^{-1} and 993 cm^{-1} indicate that at room temperature the formation of a hydrogen-bonded complex between P*p*HS and HEPy is nearly complete when stoichiometric amounts are used. However, the presence of a small band at 993 cm^{-1} indicates that a small but significant fraction of pyridine groups is still free. The competition with the intramolecular P*p*HS hydrogen-bonding seems to reduce the P*p*HS-HEPy hydrogen-bonding somewhat compared to the "reversed" P4VP-PDP system.

DSC, SAXS and WAXS are used to investigate possible structure formation in the P*p*HS/4-alkylpyridine complexes. When the alkyl tail is to short, as in the case of P*p*HS$(HDPy)_{1.0}$, no ordered structure is formed upon cooling. When the length of the alkyl tail is increased to 19 and 21 carbon atoms to obtain NDPy and HEPy respectively, ordered structures are observed where the order-disorder transition and the crystallization of the alkyl tails occur quasi simultaneously.

The DSC thermograms of P*p*HS$(NDPy)_{1.0}$ and P*p*HS$(HEPy)_{1.0}$ also show that the crystallization of the alkyl tails occurs at similar temperatures as for the pure amphiphiles, supporting the idea that the alkyl tails are already phase separated from the polymer backbone. Subsequent SAXS measurements show that upon cooling a lamellar ordered structure is obtained in which the domain spacing is dependent on the length of the alkyl tail. Although in both cases the main structure is formed by crystallization of the alkyl chains of the amphiphile in an interdigitated form, the P*p*HS$(NDPy)_{1.0}$ complex has also a fraction present that is crystallizing in an end-to-end double layer. Lowering the temperature to 0 °C reduces this fraction drastically.

Lowering x to 0.5, P*p*HS(HEPy)$_{0.5}$, shows a strong decrease in the T_c suggesting that, even though the alkyl tail is sufficiently long, ordered structures are no longer formed due to the lowering of the amphiphile mole fraction. SAXS and WAXS measurements support this observation since upon cooling no sharp scattering peaks can be observed. When x is increased to 1.5, P*p*HS(HEPy)$_{1.5}$, the results from the DSC show an exothermic crystallization peak that has two maxima centered around the T_c of pure HEPy. This indicates that the excess of HEPy has macrophase separated and shows a slightly different crystallization temperature. The SAXS and WAXS intensity profiles shows a similar pattern as obtained with P*p*HS(HEPy)$_{1.0}$, although the structure formed has a slightly smaller domain spacing. This reduction is due to the increased amount of amphiphiles resulting in the stretching of the polymer chains. On closer inspection of the SAXS results a second structure can be observed with the first and second order scattering peaks at higher scattering vectors. Also in the WAXS intensity profile an extra peak is appearing at higher scattering factors when the temperature is lowered sufficiently. The structure seems to be originating from the excess of HEPy that is not incorporated in the complex and is crystallizing separately and thus forming a separate lamellar structure, confirming the results found with the DSC.

4.5 References

1. Ruokolainen, J.; Makinen, R.; Torkkeli, M.; Makela, T.; Serimaa, R.; ten Brinke, G.; Ikkala, O. *Science* **1998,** 280, (5363), 557-560.
2. Lehn, J. M. *Polym. Int.* **2002,** 51, (10), 825-839.
3. Kato, T.; Mizoshita, N.; Kishimoto, K. *Angew. Chem.-Int. Edit.* **2006,** 45, (1), 38-68.
4. Ikkala, O.; ten Brinke, G. *Science* **2002,** 295, (5564), 2407-2409.
5. ten Brinke, G.; Ruokolainen, J.; Ikkala, O., Supramolecular Materials Based On Hydrogen-Bonded Polymers. In *Hydrogen Bonded Polymers*, Springer Berlin Heidelberg: Berlin, 2007; Vol. 207, pp 113-177.
6. Pollino, J. M.; Weck, M. *Chem. Soc. Rev.* **2005,** 34, (3), 193-207.
7. Bazuin, C. G.; Tork, A. *Macromolecules* **1995,** 28, (26), 8877-8880.
8. Faul, C. F. J.; Antonietti, M. *Adv. Mater.* **2003,** 15, (9), 673-683.
9. Valkama, S.; Lehtonen, O.; Lappalainen, K.; Kosonen, H.; Castro, P.; Repo, T.; Torkkeli, M.; Serimaa, R.; ten Brinke, G.; Leskela, M.; Ikkala, O. *Macromol. Rapid Commun.* **2003,** 24, (9), 556-560.
10. Valkama, S.; Kosonen, H.; Ruokolainen, J.; Haatainen, T.; Torkkeli, M.; Serimaa, R.; Ten Brinke, G.; Ikkala, O. *Nat. Mater.* **2004,** 3, (12), 872-876.
11. Ruokolainen, J.; Torkkeli, M.; Serimaa, R.; Komanschek, B. E.; Ikkala, O.; ten Brinke, G. *Phys. Rev. E* **1996,** 54, (6), 6646-6649.
12. du Sart, G. G.; Vukovic, I.; van Ekenstein, G. A.; Polushkin, E.; Loos, K.; ten Brinke, G. *Macromolecules* **2010,** 43, (6), 2970-2980.
13. Maki-Ontto, R.; de Moel, K.; de Odorico, W.; Ruokolainen, J.; Stamm, M.; ten Brinke, G.; Ikkala, O. *Adv. Mater.* **2001,** 13, (2), 117-121.
14. Sidorenko, A.; Tokarev, I.; Minko, S.; Stamm, M. *J. Am. Chem. Soc.* **2003,** 125, (40), 12211-12216.
15. Tokarev, I.; Krenek, R.; Burkov, Y.; Schmeisser, D.; Sidorenko, A.; Minko, S.; Stamm, M. *Macromolecules* **2005,** 38, (2), 507-516.
16. du Sart, G. G.; Vukovic, I.; Vukovic, Z.; Polushkin, E.; Hiekkataipale, P.; Ruokolainen, J.; Loos, K.; ten Brinke, G. *Macromol. Rapid Commun.* **2011,** 32, (4), 366-370.
17. Vukovic, I.; Punzhin, S.; Vukovic, Z.; Onck, P.; De Hosson, J. T. M.; ten Brinke, G.; Loos, K. *ACS Nano* **2011,** 5, (8), 6339-6348.
18. Ruokolainen, J.; ten Brinke, G.; Ikkala, O.; Torkkeli, M.; Serimaa, R. *Macromolecules* **1996,** 29, (10), 3409-3415.
19. Luyten, M. C.; van Ekenstein, G.; ten Brinke, G.; Ruokolainen, J.; Ikkala, O.; Torkkeli, M.; Serimaa, R. *Macromolecules* **1999,** 32, (13), 4404-4410.

20. Luyten, M. C.; van Ekenstein, G.; Wildeman, J.; ten Brinke, G.; Ruokolainen, J.; Ikkala, O.; Torkkeli, M.; Serimaa, R. *Macromolecules* **1998,** 31, (26), 9160-9165.
21. Ruokolainen, J.; Torkkeli, M.; Serimaa, R.; Komanschek, E.; ten Brinke, G.; Ikkala, O. *Macromolecules* **1997,** 30, (7), 2002-2007.
22. Ruokolainen, J.; Tanner, J.; Ikkala, O.; ten Brinke, G.; Thomas, E. L. *Macromolecules* **1998,** 31, (11), 3532-3536.
23. Eichhorn, K. J.; Fahmi, A.; Adam, G.; Stamm, M. *J. Mol. Struct.* **2003,** 661, 161-170.
24. Huh, J.; Ikkala, O.; ten Brinke, G. *Macromolecules* **1997,** 30, (6), 1828-1835.
25. Ruokolainen, J.; ten Brinke, G.; Ikkala, O. *Adv. Mater.* **1999,** 11, (9), 777-780.
26. Faber, M.; Voet, V. S. D.; ten Brinke, G.; Loos, K. *Soft Matter* **2012,** 8, (16), 4479-4485.
27. Borsboom, M.; Bras, W.; Cerjak, I.; Detollenaere, D.; van Loon, D. G.; Goedtkindt, P.; Konijnenburg, M.; Lassing, P.; Levine, Y. K.; Munneke, B.; Oversluizen, M.; van Tol, R.; Vlieg, E. *J. Synchrot. Radiat.* **1998,** 5, 518-520.
28. Bras, W.; Dolbnya, I. P.; Detollenaere, D.; van Tol, R.; Malfois, M.; Greaves, G. N.; Ryan, A. J.; Heeley, E. *J. Appl. Crystallogr.* **2003,** 36, 791-794.
29. Nikitenko, S.; Beale, A. M.; van der Eerden, A. M. J.; Jacques, S. D. M.; Leynaud, O.; O'Brien, M. G.; Detollenaere, D.; Kaptein, R.; Weckhuysen, B. M.; Bras, W. *J. Synchrot. Radiat.* **2008,** 15, 632-640.
30. Caputo, R.; Cassano, E.; Longobardo, L.; Palumbo, G. *Tetrahedron Lett.* **1995,** 36, (1), 167-168.
31. Capone, S.; Walde, P.; Seebach, D.; Ishikawa, T.; Caputo, R. *Chem. Biodivers.* **2008,** 5, (1), 16-30.
32. Wiley, G. A.; Rein, B. M.; Hershkowitz, R. L. *Tetrahedron Lett.* **1964,** 5, (36), 2509-2513.
33. Hulst, R.; Muizebelt, I.; Oosting, P.; van der Pol, C.; Wagenaar, A.; Smisterova, J.; Bulten, E.; Driessen, C.; Hoekstra, D.; Engberts, J. *Eur. J. Org. Chem.* **2004**, (4), 835-849.
34. Bizzotto, D.; McAlees, A.; Lipkowski, J.; McCrindle, R. *Langmuir* **1995,** 11, (8), 3243-3250.
35. Tung, P. H.; Kuo, S. W.; Chen, S. C.; Lin, C. L.; Chang, F. C. *Polymer* **2007,** 48, (11), 3192-3200.
36. Conlon, D. A.; Crivello, J. V.; Lee, J. L.; Obrien, M. J. *Macromolecules* **1989,** 22, (2), 509-516.

37. Zhao, J. Q.; Pearce, E. M.; Kwei, T. K.; Jeon, H. S.; Kesani, P. K.; Balsara, N. P. *Macromolecules* **1995,** 28, (6), 1972-1978.
38. TenBrinke, G.; Ruokolainen, J.; Ikkala, O. *Europhys. Lett.* **1996,** 35, (2), 91-95.

Chapter 5

Supramolecular Double-Comb Diblock Copolymers

Hierarchical self-assembly of supramolecular double-comb diblock copolymer complexes, based on a diblock copolymer in which both blocks can participate in the hydrogen-bonding with short amphiphiles, is discussed. A symmetric poly(4-vinylpyridine)-b-poly(N,N-dimethylacrylamide) (P4VP-b-PDMA) diblock copolymer was synthesized via reversible addition-fragmentation chain transfer (RAFT) polymerization. Supramolecular double-comb complexes were prepared by hydrogen-bonding of 3-pentadecylphenol (PDP) to both blocks, as confirmed by infrared spectroscopy. The self-assembled structures were studied using small-angle X-ray scattering (SAXS), wide-angle X-ray scattering, and transmission electron microscopy (TEM). Self-assembly of the supramolecular complex containing a stoichiometric amount of PDP resulted in a lamellar-in-lamellar structure in which the large length scale is formed by the phase separation between the supramolecular blocks of the supramolecular complex. Both domains contain a smaller lamellar morphology of a different short length scale periodicity, orientated perpendicular with respect to the large length scale lamellar structure. Because of the difference in periodicity, the two short length scales can be distinguished clearly in SAXS and TEM.

Parts of this chapter were published in: *Macromolecules* **2013,** 46, (2), 500-517.

5.1 Introduction

Nanostructures formed by self-assembly of block copolymers are of interest for potential use in nanotechnological applications.[1-3] The ability to fine-tune the morphology and the dimension of the self-assembled structures are two important assets of this approach. Lamellar, cylindrical, spherical, and even more complex microstructures with a domain spacing in the nanometer scale can be obtained by adjusting the volume fraction, molecular weight, and the interaction between the blocks. One method that has been employed successfully to further tune the self-assembled structures is based on a combination of block copolymers with supramolecular principles. Extensive research has been conducted theoretically as well as experimentally on a special class of supramolecular complexes formed by noncovalently attaching low molecular weight amphiphiles to homopolymers and block copolymers, thus forming molecules with a comb-shaped molecular architecture.[4-8] An important advantage of the supramolecular approach is that it offers a straightforward control on the morphology by altering the volume fraction and interaction between the blocks by simply varying the amount of amphiphile added. Furthermore, after formation of the desired morphology, the amphiphiles can be removed using a selective solvent in order to fabricate nanotemplates.[9, 10]

One well-established example involves the formation of comb-shaped supramolecules via hydrogen-bonding of 3-pentadecylphenol (PDP) to a poly(4-vinylpyridine) (P4VP) backbone.[11] Formation of comb-coil supramolecular block copolymers in which the comb is formed by the P4VP-PDP complex while the coil is formed by polystyrene (PS) results in the formation of self-assembled hierarchical phase separated structures in which a small length scale structure formed by P4VP-PDP is formed within a large length scale structure of P4VP-PS.[12]

To extend this supramolecular concept even further, one can think of diblock copolymers where both blocks act as hydrogen-bonding acceptors. Addition of, e.g., PDP, to such a block copolymer would ultimately result in a double-comb system in which PDP is hydrogen-bonded to both sides of the diblock copolymer. This will result in a complex system where the distribution of the amphiphiles over both blocks will depend on the hydrogen-bonding strength and where in the self-assembled state potentially three different length scales may be present: a large length scale

corresponding to the separation between the two comb-shaped supramolecular blocks and two short length scales due to the self-assembly within the latter two domains. These two short length scales will in general not be exactly the same, and one of the challenges concerns the adaptation of the overall structure to the presence of these three different length scales. Recently, Markov et al. published results of theoretical modeling and computer simulations on a comparable, but simplified, system.[13] The simulations were performed using a double-comb block copolymer in which the side chains were covalently linked to both blocks of the polymer backbone. Specific interactions between the blocks of the block copolymer as well as the interactions between the side chains and the polymer backbone resulted in the formation of a range of lamellar, cylindrical, and spherical microphase separated structures. Hierarchical structures were found in the fully microphase separated systems. The possibility that the two short length scales involved in the microphase separation between the side chains and the polymer backbones might be different was, however, not considered. It is precisely this possibility together with the distribution of side chains over the two blocks that makes the experimental realization of such a system of considerable interest. So far only one experimental double-comb system has been described in the literature. It concerns the case where different liquid crystalline side chains are covalently attached to a polymer backbone.[14] The difference between the side chains resulted in the formation of hierarchical lamellar nanostructures in which the semicrystalline side chains were orientated perpendicular to the lamellar interface.

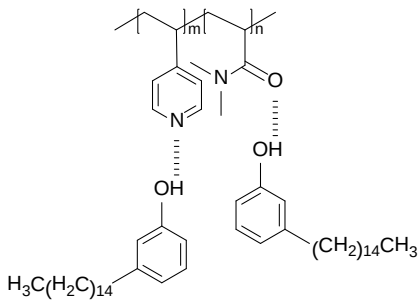

Scheme 5.1 Schematic representation of PDP hydrogen-bonded to a P4VP-*b*-PDMA diblock copolymer.

In this chapter the synthesis and self-assembly of a poly(4-vinylpyridine)-*block*-poly(*N,N*-dimethylacrylamide) (P4VP-*b*-PDMA) diblock copolymer and its supramolecular complex with PDP, schematically shown in Scheme 5.1, will be discussed. P4VP and PDMA were synthesized using reversible addition-fragmentation chain transfer (RAFT) polymerization (Scheme 5.2) in which *S*-dodecyl-*S'*-(isobutyric acid) trithiocarbonate (DIBTTC) was used as the chain transfer agent (CTA). The advantage of using RAFT polymerization is the high monomer compatibility and a good control over M_n and PDI. Furthermore, successful controlled polymerization of 4VP as well as DMA via RAFT is already reported in the literature.[15-17] The P4VP-*b*-PDMA diblock copolymer was prepared by polymerization of DMA using trithiocarbonate end-capped P4VP as macro-chain-transfer agent (macro-CTA). The self-assembly study presented focuses on the structures formed by [P4VP-*b*-PDMA](PDP)$_x$ supramolecular double-comb complexes in which the amphiphile ratio x represents the number of PDP molecules per functional group. Amphiphile ratios of 1.0 and 0.5 are used.

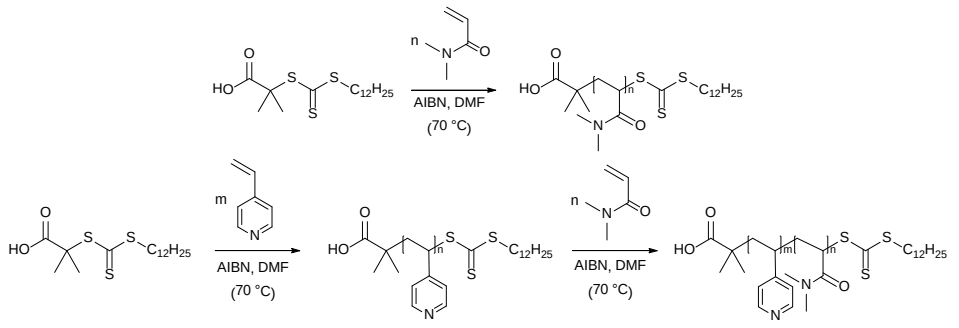

Scheme 5.2 Synthetic pathway for the RAFT polymerization of PDMA, P4VP, and P4VP-*b*-PDMA.

5.2 Experimental

5.2.1 Materials

α,α'-Azobis(isobutyronitrile) (AIBN, Fluka, 98+%) was recrystallized twice from methanol (0.14 g mL^{-1} at maximum 40 °C) at -18 °C, dried in a vacuum desiccator, and stored under nitrogen. 4-Vinylpyridine (4VP, Acros, 95%) was stirred over calcium hydride for 24 h and condensed at a high-vacuum line (10^{-6} mbar) into a flask containing freshly cut sodium. After stirring overnight at room temperature, it was condensed a second time into an ampule, subjected to three freeze-pump-thaw cycles and stored under nitrogen at -18 °C. *N,N*-Dimethylacrylamide (DMA, Acros, 99%) was distilled twice under reduced pressure (60 °C at 0.02 mbar) from finely ground calcium hydride, subjected to three freeze-pump-thaw cycles, and stored under nitrogen at -18 °C. *S*-Dodecyl-*S'*-(isobutyric acid) trithiocarbonate (DIBTTC, Aldrich, 98%), toluene (Lab-Scan, 99.5%), *N,N*-dimethylformamide (DMF, Acros, 99.8%, extra dry over Molecular Sieve, AcroSeal), dichloromethane (CH_2Cl_2, Lab-Scan, 98%), hexane (Lab-Scan, 99%), diethyl ether (Lab-Scan, 99.5%), and chloroform ($CHCl_3$, Lab-Scan, 99.5+ %) were used as received. 3-Pentadecylphenol (PDP, Aldrich, 98%) was recrystallized twice from petroleum ether.

5.2.2 Synthesis of P4VP

To a 50 mL round-bottom flask equipped with a Teflon stirring bar was added DIBTTC (41.1 mg, 0.113 mmol), AIBN (2.63 mg, 0.0160 mmol), and 4.5 mL of DMF. Next 4VP (4 mL, 37.3 mmol) was added via a syringe, and the flask was connected to a high-vacuum line. Subsequently, the bright yellow solution was subjected to freeze-pump-thaw cycles (10^{-6} mbar) until no more gas release was observed. After backfilling with nitrogen, the flask was closed and submerged in a thermostated oil bath at 70 °C. After a reaction time of 21 h the polymerization was stopped by quenching the reaction mixture in liquid nitrogen. The obtained viscous dark yellow/orange reaction mixture was diluted by adding 4 mL of DMF and subsequently the polymer was precipitated in a 10-fold excess of toluene. The yellow/orange solid was isolated via filtration over a pore size 3 glass filter and dried under vacuum overnight at 40 °C. Next, the solid was dissolved in CH_2Cl_2 to a concentration of about 0.3 g mL^{-1} and reprecipitated in a 10-fold excess of toluene.

The solid was isolated via filtration over a pore size 3 glass filter and dried under vacuum overnight at 40 °C yielding P4VP as a yellow/orange solid (2.57 g, 66% yield). The product was stored in a vacuum oven at 40 °C until further use.

P4VP: M_n= 24.7 kg mol^{-1}, PDI = 1.20. ^{1}H NMR ($CDCl_3$, 300 MHz): δ = 1.0 - 2.0 (br m, CH and CH_2), 6.0 - 6.7 (br m, ArH), 8.0 - 8.7 (br m, ArH) ppm.

5.2.3 Synthesis of PDMA

To a 50 mL round-bottom flask equipped with a Teflon stirring bar was added DIBTTC (30.7 mg, 0.084 mmol), AIBN (1.95 mg, 0.0119 mmol), and 3 mL of DMF. Next, DMA (3 mL, 29.1 mmol) was added via a syringe and the flask was connected to a high vacuum line. Subsequently, the bright yellow solution was subjected to freeze-pump-thaw cycles (10^{-6} mbar) until no more gas release was observed. After backfilling with nitrogen the flask was closed and submerged in a thermostated oil bath at 70 °C. After a reaction time of 14 h the polymerization was stopped by quenching the reaction mixture in liquid nitrogen. The obtained viscous bright yellow reaction mixture was diluted by adding 6 mL of CH_2Cl_2, and subsequently the polymer was precipitated in a 10-fold excess of hexane/diethyl ether 50:50 (v/v). The pale yellow solid was isolated via filtration over a pore size 3 glass filter and dried under vacuum overnight at 40 °C. Next, the solid was dissolved in CH_2Cl_2 to a concentration of about 0.3 g mL^{-1} and reprecipitated in a 10-fold excess of hexane. The solid was isolated via filtration over a pore size 3 glass filter and dried under vacuum overnight at 40 °C yielding PDMA as a pale yellow solid (2.17 g, 75% yield). The product was stored in a vacuum oven at 40 °C until further use.

PDMA: M_n = 36.6 kg mol^{-1}, PDI = 1.13. ^{1}H NMR ($CDCl_3$, 300 MHz): δ = 1.1 - 1.9 (br m, CH_2), 2.0 - 2.7 (br m, CH), 2.7 - 3.2 (br m, CH_3) ppm.

5.2.4 Synthesis of P4VP-*b*-PDMA

To a 50 mL round-bottom flask equipped with a Teflon stirring bar was added the trithiocarbonate end-capped P4VP macro-CTA (1.13 g, 0.0456 mmol) described in

the previous section and 2.5 mL of DMF. The mixture was stirred until the homopolymer had dissolved completely, resulting in a dark yellow solution. AIBN (0.5 mL of a 1.8 mg mL^{-1} solution in DMF, 0.0055 mmol) and DMA (1.5 mL, 14.6 mmol) were added to the solution, and the flask was connected to a high-vacuum line. The reaction mixture was subjected to freeze-pump-thaw cycles (10^{-6} mbar) until no more gas release was observed. After backfilling with nitrogen the flask was closed and submerged in a thermostated oil bath at 70 °C. After a reaction time of 20 h the polymerization was stopped by quenching the reaction mixture in liquid nitrogen. The obtained viscous yellow reaction mixture was diluted by adding 7 mL of CH_2Cl_2, and subsequently the polymer was precipitated in a 10-fold excess of toluene/hexane 50:50 (v/v). The pale yellow solid was isolated via filtration over a pore size 3 glass filter and dried under vacuum overnight at 40 °C. Residual solvent traces were removed by placing the product for 30 min in an oven at 130 °C. Next, the polymer (2.33 g) was dissolved in 15 mL of CH_2Cl_2 and reprecipitated in a 10-fold excess of hexane/diethyl ether 50:50 (v/v). The product was isolated via filtration over a pore size 3 glass filter and dried under vacuum overnight at 40 °C followed by 1 h in an oven at 130 °C, yielding P4VP-*b*-PDMA as a slightly yellow solid (2.12 g, 69% yield).

P4VP-*b*-PDMA: M_n = 46.6 kg mol^{-1}, f_{P4VP} = 0.53, PDI = 1.35. ^{1}H NMR ($CDCl_3$, 300 MHz): δ = 1.0 - 2.0 (br m, CH and CH_2 - P4VP and PDMA), 2.0 - 2.7 (br m, CH - PDMA), 2.7 - 3.2 (br m, CH_3 - PDMA), 6.0 - 6.7 (br m, ArH - P4VP), 8.0 - 8.5 (br. m, ArH - P4VP) ppm.

5.2.5 Sample preparation

Polymer films of P4VP-*b*-PDMA, P4VP(PDP)$_{1.0}$, PDMA(PDP)$_{1.0}$, [P4VP-*b*-PDMA](PDP)$_{0.5}$, and [P4VP-*b*-PDMA](PDP)$_{1.0}$ were obtained by dissolving ca. 100 mg of the pure polymer or the polymer together with the calculated amount of PDP amphiphile in 7 mL of $CHCl_3$. The resulting clear solutions were stirred for at least 1 h at room temperature. The solutions were cast in Petri dishes which were then placed into an atmosphere saturated with $CHCl_3$ so that the solvent was allowed to evaporate slowly. After at least one week of solvent annealing, during which all the solvent had evaporated, the Petri dishes were heated for 30 min in an oven at 130 °C.

Ultrathin sections of the prepared films were obtained using a Leica EM UC7 cryo-microtome. Microtomed sections were stained using iodine to obtain contrast during TEM so that the microphase separation of the diblock copolymer in the [P4VP-*b*-PDMA](PDP)$_{1.0}$ supramolecular complex could be observed. The samples were stained from 5 up to 60 min. Unstained samples were used in TEM to observe the microphase separation of PDP from the polymer backbone.

Shear-induced alignment of the [P4VP-*b*-PDMA](PDP)$_{1.0}$ sample was conducted using a homemade tooth rheometer.[18-20] This is a modified Bohlin VOR rheometer, specially designed to perform in-situ SAXS studies on the alignment of complex fluids induced by large-amplitude oscillatory shear (LAOS). The instrument is a kind of plate-plate rheometer, but instead of the normally used relatively large plates, its plates are rather small and look like "teeth" (Figure 5.21). In this study a tooth couple of 5 by 3 mm in size have been employed. Using the rheometer gives rise to adequate rheological measurements despite the small-size geometry.[19] Although the main advantage of this setup is the possibility to perform in-situ SAXS measurements, during this study the tooth rheometer has solely been utilized ex-situ to shear very small amounts of sample, 30 mg or even less. The samples have been sheared inside a 0.5 mm gap between the rheometer teeth. After loading the sample in the rheometer at 80 °C a required gap width between the rheometer teeth was set, and any excess of the sample around the tooth edges was removed prior to shear. Shear alignment was performed in a continuous oscillatory mode at a frequency of 1 Hz, with shear strain amplitude of ca. 85% and a constant temperature of 80 °C. Typical time limit for the shear-induced alignment was ca. 1 h during which rheological characteristics, such as the storage and loss moduli G' and G'', respectively, as well as the phase angle ϕ, were also measured. After the alignment, the sample was first allowed to cool to room temperature and, prior to its removal from the rheometer, cooled further using liquid nitrogen. Aligned samples were analyzed using SAXS and TEM. During SAXS measurements the beam passed through a 5 mm long sample in the tangential direction, through a 3 mm long sample in the radial direction and through a 0.5 mm long sample in the normal direction.

5.2.6 Characterization

Gel permeation chromatography (GPC) measurements were performed in *N,N*-dimethylformamide with 0.01 M LiBr on a Viscotek GPCMAX equipped with model 302 TDA detectors, using two columns (PSS-Gram-1000/30, 10μm, 30 cm). Calibration was performed using narrow disperse polystyrene standards (Polymer Laboratories). The molecular weights and the polydispersity indices of both homopolymers and the polydispersity index of the block copolymer were determined using universal calibration (UC). The refractive index increment (d*n*/d*c*) was measured using the Viscotek Model 302 refractometer detector.

^{1}H and ^{13}C nuclear magnetic resonance (NMR) spectra were recorded on a 300 MHz Varian VXR at room temperature, using $CDCl_3$ as solvent.

Attenuated total reflection (ATR) infrared measurements were performed using a Specac Golden Gate accessory with heated diamond top-plate on a Bruker IFS88 spectrometer equipped with a MCT-A detector at resolution 4 cm^{-1}.

Differential scanning calorimetry was performed using a DSC Q1000 (TA Instruments). The pure polymers were analyzed during a heat/cool/heat cycle in a range between 0 to 180 °C using a heating/cooling rate of 10 °C min^{-1}. The second heating cycle was used to determine the glass transition temperature of the polymers. The glass transition temperatures reported are determined by the inflection point method using Universal Analysis software provided by TA Instruments. The supramolecular complexes were analyzed during a heat/cool/heat cycle in a range between -20 and 130 °C using a heating/cooling rate of 5 °C min^{-1}; the cooling cycle was used for analysis.

Simultaneous small-angle X-ray scattering (SAXS) and wide-angle X-ray scattering (WAXS) measurements were performed at the Dutch-Belgian Beamline (DUBBLE) station BM26B of the European Synchrotron Radiation Facility (ESRF) in Grenoble (France).[21-23] The sample-to-detector distances used were ca. 2 m and ca. 6 m. The wavelength was 1.033 Å. A Dectris-Pilatus 1 M detector with a resolution of 981 × 1043 pixels and a pixel size of 172 × 172 μm has been employed to record the 2D-SAXS scattering patterns. A Dectris-Pilatus 300 K-W detector with a resolution of 1475 × 195 pixels and a pixel size of 172 × 172 μm has been employed to record the 2D-WAXS scattering patterns. Standard corrections for sample absorption and background subtraction have been performed. The data were normalized with respect

to the incident beam intensity in order to correct for primary beam intensity fluctuations. The scattering patterns from silver behenate (AgBh) were used for the detector calibration. The scattering vector q is defined as $q = 4\pi/\lambda \sin\theta$ with 2θ being the scattering angle. The SAXS and WAXS intensity profiles were acquired as a function of temperature during cooling from the melt with either 5 °C min^{-1} from 120 to 0 °C or 10 °C min^{-1} from 180 to 0 °C using an acquisition time of 30 s for each frame.

Additional SAXS measurements on aligned samples were performed at the University of Groningen using an advanced Nano-Star SAXS setup which is a homemade assembly of a NanoStar camera and a Microstar X-ray generator (both by Bruker AXS). The collimation line between the rotating anode generator and the camera consists of multilayer optics Montel-P (by Incoatec) and 3 pinholes (by Rigaku) of 0.5, 0.3, and 0.5 mm in diameter spaced at distances of ca. 14, 40, and 62 cm from the middle of the optics unit, respectively. Passing through the optics, the primary beam is monochromized for Cu K_α radiation (a wavelength of 0.1542 nm) and simultaneously collimated to get a low divergent beam (the divergence is below 1 × 1 $mrad^2$). Both the optics and the collimation line with the first and the second pinholes are evacuated. The third pinhole located in the sample chamber of the NanoStar camera is in air. All the three pinholes are manually adjusted. A measured sample, which is also in air, is thus located at ca. 66 cm from the optics, while the sample-to-detector distance is either ca. 24, 64, or 104 cm. The major part of the distance is to be inside of an evacuated flight tube. The maximal parameters of the rotating anode X-ray generator are 45 kV and 60 mA. At these parameters the flux of the primary X-ray beam at the sample position is estimated to be ca. 8 x 10^8 photons·s^{-1} mm^{-2}, while the size of the beam is about 0.4 mm in diameter. The SAXS intensity profiles were acquired at room temperature using an acquisition time of 3 min.

Cryo-transmission electron microscopy (cryo-TEM) was carried out using a field emission cryo-electron microscope (JEOL JEM-3200FSC) which was operating at 300 kV voltage. Images were taken in bright field mode and using zero loss energy filtering (omega type) with a slit width of 20 eV. Micrographs were recorded using Gatan Ultrascan 4000 CCD camera. The specimens were cooled with liquid helium and maintained at a temperature of -255 °C during the imaging.

5.3 Results and discussion

5.3.1 Synthesis

5.3.1.1 P4VP and PDMA homopolymers

The RAFT polymerization of 4VP and DMA resulted in well-defined P4VP and PDMA homopolymers with a PDI of 1.20 and 1.13, respectively. Table 5.1 lists the properties of the homopolymers prepared. The concentration of the thermal initiator, AIBN, was kept low so that the majority of the polymer chains were initiated by the carboxylic acid containing R-group of the RAFT agent DIBTTC. The reaction mixtures were degassed thoroughly using multiple freeze-pump-thaw cycles on a high-vacuum line to ensure the complete removal of oxygen. This proved to be necessary in order to prevent oxidation of the RAFT agent during the reaction.[24] Especially when the homopolymer needs to be extended to obtain a diblock copolymer, as described in paragraph 5.3.1.2, it is important that the majority of the homopolymer precursor contains the CTA end group and oxidation should be circumvented. The synthesis of the diblock copolymers even proved to be impossible when the freeze-pump-thaw cycles were done with a moderate vacuum setup, as could be observed by a color change of the reaction mixture from orange to black.

Table 5.1. Reaction times, conversions and molecular characteristics of the P4VP and PDMA homopolymers.

	time (h)	conv [a] (%)	$M_{n,calc}$ [b] (kg mol^{-1})	M_n [c] (kg mol^{-1})	PDI [c]
P4VP	21	75	26.4	24.7	1.20
PDMA	14	100	34.7	36.6	1.13

[a] Determined by ^{1}H NMR spectroscopy. [b] Calculated using the monomer/initiator ratio, the conversion and the molecular weights of the monomer and the RAFT agent. [c] Determined by GPC (DMF).

The results in Table 5.1 show that the synthesis of PDMA is very fast compared to P4VP since a conversion of 100% is reached in a much shorter reaction time. This difference is originating from the fewer possibilities of PDMA to stabilize the

propagating radical end group via resonance compared to the styrene-like monomer 4VP. Even though the polymerization of PDMA reached 100% conversion the PDI is only 1.13, indicating that the polymerization is well controlled. Longer reaction times have also been investigated for the polymerization of PDMA (results not shown), resulting in polymers with a higher PDI which is caused by the increased chance of bimolecular termination. The ^{1}H NMR spectra of P4VP and PDMA are shown in Figures 5.1a and 5.1b, respectively.

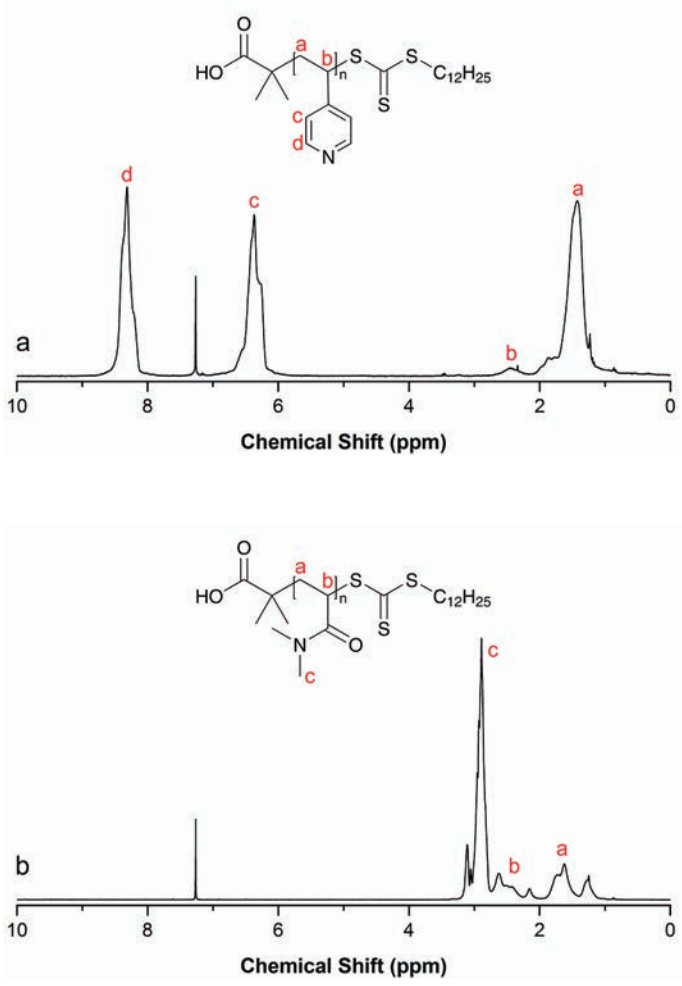

Figure 5.1 ^{1}H NMR spectra of P4VP (a) and PDMA (b) (solvent: $CDCl_3$).

5.3.1.2 P4VP-*b*-PDMA diblock copolymer

When synthesizing P4VP-*b*-PDMA diblock copolymers it is important to start with the least reactive monomer; otherwise, reinitiation will be inefficient which will subsequently lead to ill-defined block copolymers.[25, 26] Compared to DMA, 4VP is much better able to stabilize the reactive radical end-group via resonance and is therefore the least reactive building block. Therefore, the block copolymer synthesis was started using the P4VP homopolymer described in section 5.3.1.1 as macro-CTA (Scheme 5.2). Furthermore, it was shown that for DMA the monomer conversion went to 100% within 14 h while maintaining good control over the molecular weight and its distribution. This observation was utilized by adding DMA in such an amount that complete monomer consumption results in a symmetric P4VP-*b*-PDMA diblock copolymer. The polymerization was stopped after 20 h and subsequent analysis using ^{1}H NMR proved that complete conversion of the DMA monomer was achieved.

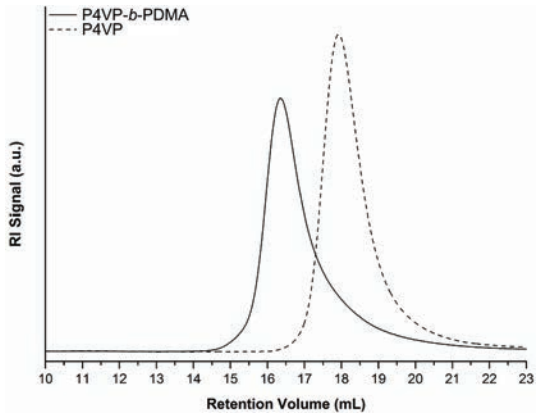

Figure 5.2 GPC chromatograms of P4VP homopolymer (dashed line) and the P4VP-*b*-PDMA diblock copolymer (solid line).

Figure 5.2 presents the GPC chromatograms of the P4VP homopolymer and the P4VP-*b*-PDMA diblock copolymer. It clearly shows the successful extension of the P4VP macro-CTA. The GPC chromatogram of the diblock copolymer shows slightly more tailing on the higher elution volume side of the chromatogram than the P4VP homopolymer indicating the presence of P4VP homopolymer. However, it should be taken into account that the d*n*/d*c* of P4VP and PDMA are 0.12 mL g^{-1} and

0.076 mL g^{-1}, respectively, and therefore P4VP has a larger influence on the refractive index compared to PDMA. As a result, the P4VP homopolymer will be more pronounced in the RI signal than the diblock copolymer.

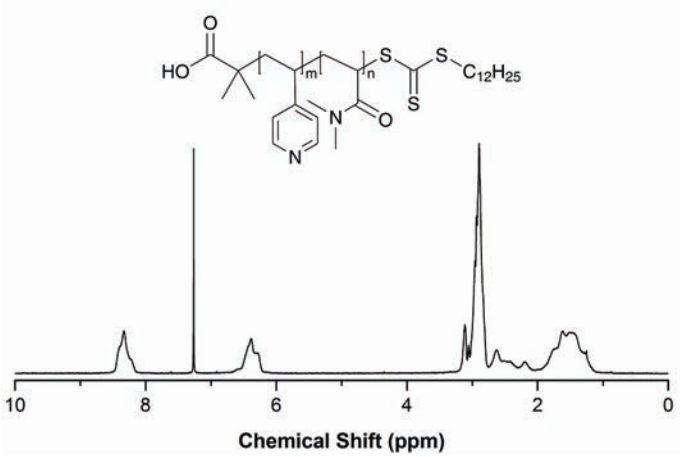

Figure 5.3 ^{1}H NMR spectrum of P4VP-*b*-PDMA (f_{P4VP} = 0.53; solvent: $CDCl_3$).

The ^{1}H NMR spectrum of the P4VP-*b*-PDMA diblock copolymer is shown in Figure 5.3. The block fractions were calculated from the ^{1}H NMR spectrum of the P4VP-*b*-PDMA diblock copolymer using the chemical shift caused by the two aromatic protons of P4VP (8.0 - 8.5 ppm) and, after correction, the chemical shift in the alkane region of the protons of PDMA (1.0 - 3.2 ppm). This results in a P4VP weight fraction f_{P4VP} of 0.53, which is in perfect agreement with the reaction stoichiometry. The molecular weight of the P4VP-*b*-PDMA diblock copolymer can then be calculated using f_{P4VP} in combination with the M_n of the P4VP precursor. In Table 5.2, the molecular weight, weight fraction, and polydispersity are listed for the P4VP-*b*-PDMA diblock copolymer.

Table 5.2 Reaction time, conversion and molecular characteristics of the P4VP-*b*-PDMA diblock copolymer.

	time (h)	conv [a] (%)	M_n [b] (kg mol^{-1})	f_{P4VP} [c]	PDI [d]
P4VP-*b*-PDMA	21	100	46.6	0.53	1.35

[a] Determined by ^{1}H NMR spectroscopy. [b] Calculated using the GPC results of P4VP and the ratio of integrated intensities of the proton signals in ^{1}H NMR. [c] Calculated from the ratio of integrated intensities of proton signals in ^{1}H NMR. [d] Determined by GPC (DMF).

Figure 5.4 presents the DSC thermograms of P4VP, PDMA, and P4VP-*b*-PDMA obtained during the second heating scan using a heat rate of 10 °C min^{-1}. The thermograms demonstrate that the diblock copolymer has two separate glass transition temperatures (T_g) that correspond to PDMA (126 °C) and P4VP (150 °C). Although nothing can be said about the nature of the microphase separated morphology, the presence of two T_g's proves that the two blocks of P4VP-*b*-PDMA are phase separated. Of course, a lamellar morphology is to be expected.

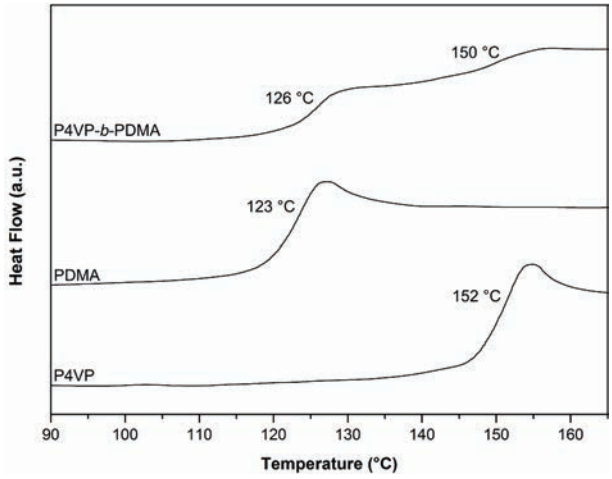

Figure 5.4 DSC thermograms recorded during the second heating at 10 °C min^{-1} of P4VP, PDMA, and P4VP-*b*-PDMA. The corresponding T_g is displayed next to each transition.

5.3.2 Supramolecular double-comb copolymer complex

5.3.2.1 Infrared spectroscopy

The interactions between polymers and short amphiphiles can be studied using infrared spectroscopy. Upon successful formation of the complex, a shift in several infrared bands can be observed for the functional groups involved in the complex formation. In order to analyze the double-comb diblock copolymer complexes using IR spectroscopy, supramolecular complexes of PDP with both the homopolymers, P4VP and PDMA, were investigated first. The results of IR spectroscopy studies on P4VP(PDP)$_x$ complexes are already extensively reported in the literature,[27, 28] and some of those results were reproduced for our study. This ensured that the results are all obtained in the same manner, and the observed shifts in the bands of the different supramolecular complexes can be compared with each other.

A P4VP(PDP)$_{1.0}$ film was prepared using the synthesized P4VP (M_n = 24.7 kg mol^{-1}, PDI = 1.20) with the calculated amount of PDP. Upon formation of the complex, several bands of P4VP change, reflecting the change in electronic distributions. The changes that are of particular interest are the stretching modes of the pyridine ring of P4VP at 1597, 1415, and 993 cm^{-1}, which shift to 1603 (+6), 1421 (+6) and 1008 (+15) cm^{-1}, respectively.[27] The shift of the bands to higher frequencies after the formation of the complex reflects the strengthening of the bonds in the pyridine ring. Figure 5.5 presents the scale-expanded infrared spectra of the areas of interest of P4VP(PDP)$_{1.0}$, P4VP, and PDP. Shifts to higher frequencies of the bands of the pyridine ring stretching modes are observed, as was expected. The shifts 1594 to 1600 (+6) cm^{-1}, 1413 to 1420 (+7) cm^{-1}, and 992 to 1006 (+14) cm^{-1} are similar in magnitude compared to the results found in the literature. The band near 1000 cm^{-1} in Figure 5.5d originates from the phenyl ring of PDP.[27] Slight differences in the position of the absorption and in the peak intensities are due to the use of ATR-IR instead of transmission IR, as in the literature.

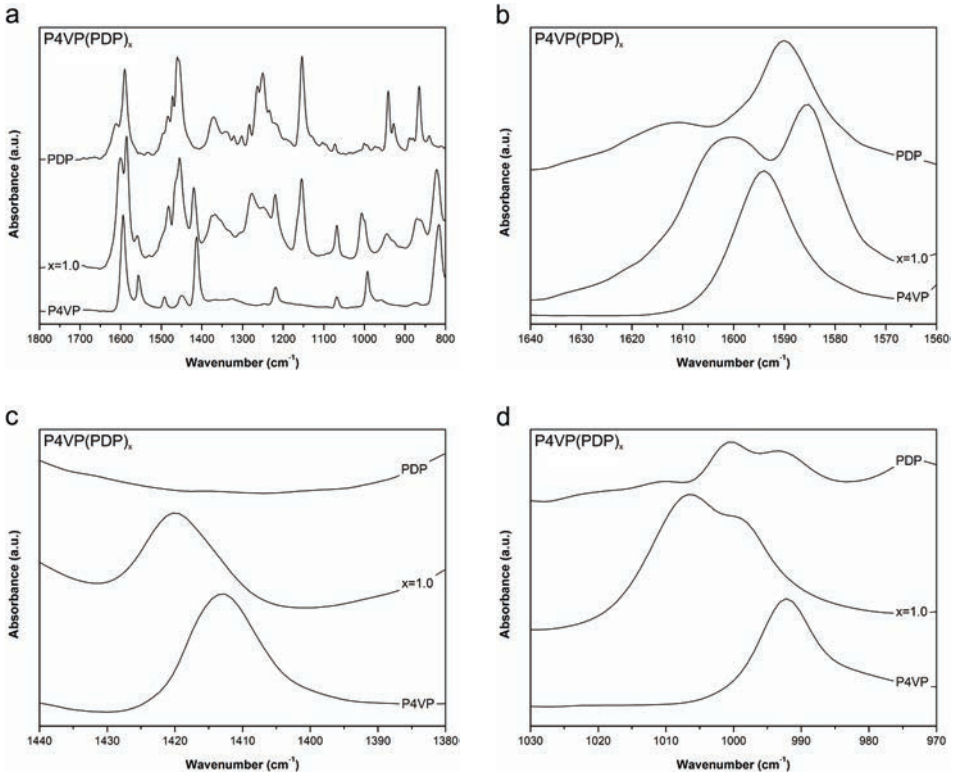

Figure 5.5 Infrared spectra of P4VP(PDP)$_{1.0}$, P4VP, and PDP, in the regions 1800 - 800 cm^{-1} (a), 1640 - 1560 cm^{-1} (b), 1440 - 1380 cm^{-1} (c), and 1030 - 970 cm^{-1} (d).

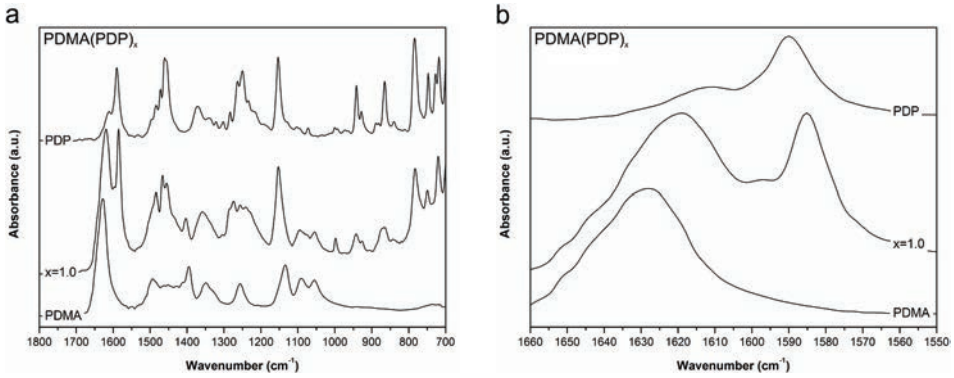

Figure 5.6 Infrared spectra of PDMA(PDP)$_{1.0}$, PDMA, and PDP, in the regions 1800 - 700 cm^{-1} (a) and 1660 - 1550 cm^{-1} (b).

The complex formation of PDMA and PDP was also investigated via infrared spectroscopy. For this, a PDMA(PDP)$_{1.0}$ film was prepared using the synthesized PDMA (M_n = 36.6 kg mol^{-1}, PDI = 1.13) with the calculated amount of PDP. Primarily, the carbonyl group of PDMA is involved in the hydrogen-bonding process and therefore the corresponding absorption band was studied.[29-31] A study on PDMA hydrogen-bonded to poly(acrylic acid) shows that the carbonyl band shifts from 1642 to 1616 (-26) cm^{-1} due to weakening of the carbonyl bond.[30] PDMA hydrogen-bonded to phenol-formaldehyde resins results in an even larger shift of the carbonyl absorption band, from 1642 to 1608 (-34) cm^{-1}.[31]
Figure 5.6 presents the scale-expanded infrared spectra in the regions 1800 - 700 cm^{-1} (Figure 5.6a) and 1660 and 1550 cm^{-1} (Figure 5.6b) of PDMA(PDP)$_{1.0}$, PDMA, and PDP. The observed shift of the carbonyl band in the complex is from 1628 to 1619 (-9) cm^{-1} (Figure 5.6b), clearly demonstrating the formation of hydrogen bonds. This shift is smaller than the shifts reported in the literature, and this is mainly caused by the lower value found for the carbonyl absorption band of the PDMA homopolymer, 1628 vs 1642 cm^{-1}. This is most likely the result of a small amount of water present in the sample due to the high hygroscopicity of PDMA.

Infrared studies on the behavior of the hydrogen-bonded complex between P4VP and PDP at increased temperatures demonstrated that the hydrogen-bonding is almost complete for temperatures below 100 °C when equal numbers of pyridine and phenol groups are present.[28] Upon further increasing the temperature, an increase of free pyridine groups is identified by shifts to lower frequencies of the bands of the stretching modes of the pyridine ring. In order to investigate the temperature dependency of the hydrogen-bonding between PDMA and PDP, infrared spectra of PDMA(PDP)$_{1.0}$ were recorded during heating from 25 to 145 °C, of which the results are presented in Figure 5.7. Upon increasing the temperature a shift to higher wavenumbers can be observed for the absorption maximum, implying that the hydrogen bonds are being weakened in this system as well. At 145 °C the main band that corresponds to the carbonyl vibration lies at ~1623 cm^{-1}. Upon heating a small shoulder arises at higher frequencies, indicating an increase in carbonyl groups not participating in hydrogen-bonding. Nevertheless, at temperatures below 100 °C a majority of the PDP molecules is still hydrogen-bonded to PDMA.

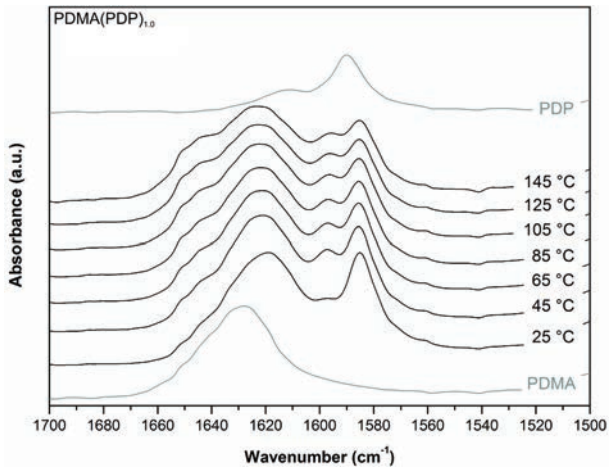

Figure 5.7 Infrared spectra at different temperatures of $PDMA(PDP)_{1.0}$ in the 1700 - 1500 cm^{-1} region together with the infrared spectra of PDMA and PDP recorded at room temperature.

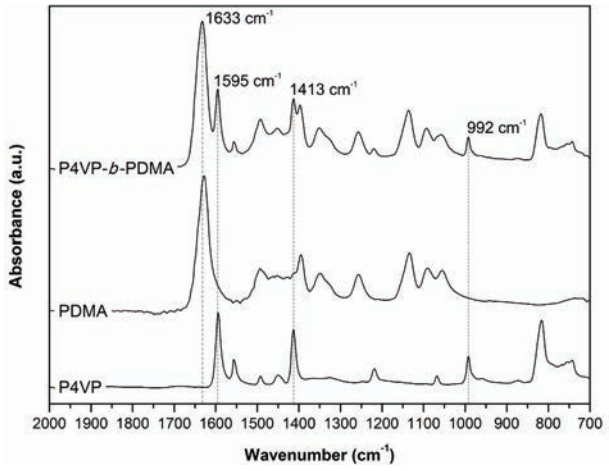

Figure 5.8 Infrared spectra of P4VP-*b*-PDMA, PDMA, and P4VP.

So far, the successful formation of a supramolecular complex via hydrogen-bonding between the homopolymers and PDP has been demonstrated via IR spectroscopy. For

the supramolecular complex envisioned it is necessary that PDP is hydrogen-bonded to both blocks of the P4VP-*b*-PDMA diblock copolymer simultaneously. Figure 5.8 presents the IR spectra of P4VP-*b*-PDMA, PDMA, and P4VP, in which the dashed lines indicate the position of the four bands (1633, 1595, 1413, and 992 cm^{-1}) which were previously shown to shift upon hydrogen-bonding. All four bands can be observed clearly even though there is some overlap. Furthermore, since the IR spectrum of P4VP-*b*-PDMA is simply a sum of both homopolymers, a comparison of the supramolecular double-comb complex with the complexes formed by the homopolymers and PDP is allowed.

Two films were prepared to study the hydrogen-bonding between P4VP-*b*-PDMA (M_n= 46.6 kg mol^{-1}, PDI = 1.35, f_{P4VP} = 0.53) and PDP: one with a stoichiometric composition, [P4VP-*b*-PDMA](PDP)$_{1.0}$, and one in which the amount of PDP amphiphiles per functional group is reduced to x = 0.5, [P4VP-*b*-PDMA](PDP)$_{0.5}$. The resulting scale-expanded infrared spectra in the regions 2000-700 cm^{-1}, 1700-1550 cm^{-1}, 1440-1380 cm^{-1}, and 1030-970 cm^{-1} of [P4VP-*b*-PDMA](PDP)$_{1.0}$, [P4VP-*b*-PDMA](PDP)$_{0.5}$, P4VP-*b*-PDMA, and PDP are shown in Figures 5.9a to 5.9d, respectively. Upon addition of PDP, all four important absorption bands shift to lower (the band of the carbonyl stretching mode of PDMA) or higher (the bands of the pyridine stretching modes of P4VP) wavenumbers. For the diblock copolymer with a stoichiometric amount of PDP added, [P4VP-*b*-PDMA](PDP)$_{1.0}$, the shift of the three characteristic bands of the stretching modes of the pyridine ring of P4VP, 1595 to 1598 (+3) cm^{-1}, 1413 to 1420 (+7) cm^{-1}, and 992 to 1007 (+15) cm^{-1}, are almost identical to the shifts observed in the P4VP(PDP)$_{1.0}$ complex. The shift of the band corresponding to the stretching mode of the carbonyl group of PDMA, 1633 to 1621 (-12) cm^{-1}, is somewhat larger compared to the PDMA(PDP)$_{1.0}$ complex due to the difference in position of the carbonyl band in the pure block copolymer. Likely, the diblock copolymer sample contained less water than the PDMA homopolymer sample, resulting in the band of the carbonyl group appearing at a higher wavenumber. Although the exact distribution of the amphiphiles along the diblock copolymer cannot be abstracted from the data, it is clear that PDP forms a complex with the P4VP block as well as the PDMA block in the diblock copolymer.

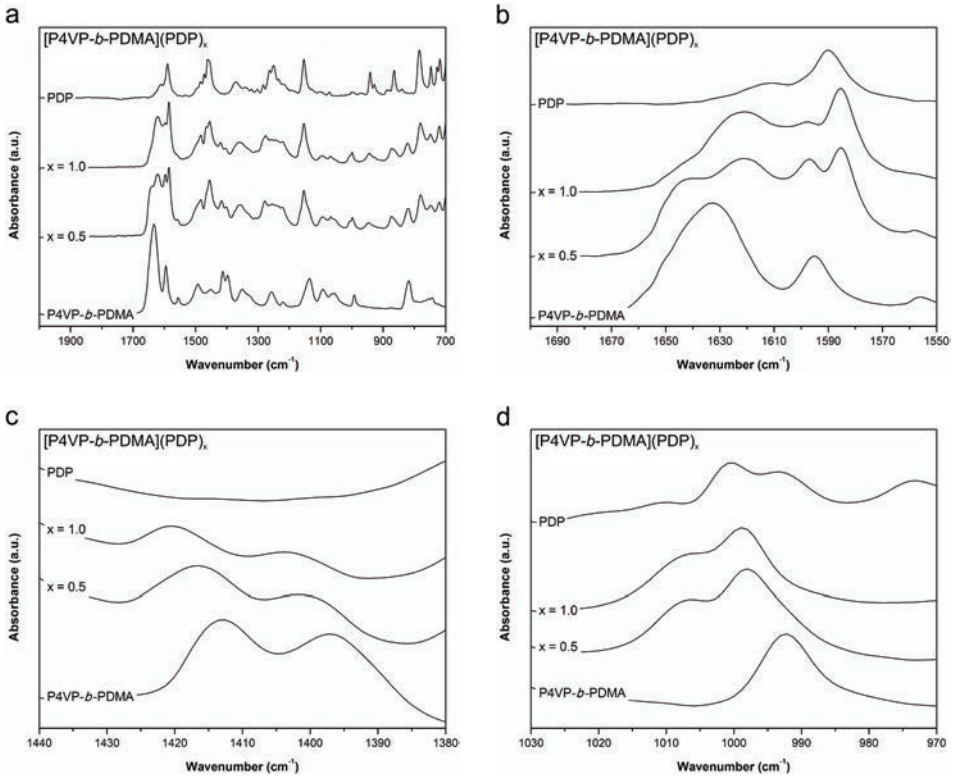

Figure 5.9 Infrared spectra of [P4VP-*b*-PDMA](PDP)$_x$ (x = 0.5 and 1.0), P4VP-*b*-PDMA, and PDP, in the regions 2000 - 700 cm^{-1} (a), 1700 - 1550 cm^{-1} (b), 1440 - 1380 cm^{-1} (c), and 1030 - 970 cm^{-1} (d).

Lowering the amount of PDP per functional group to a half showed a different result. The position of the band of the carbonyl stretch after formation of hydrogen bonds, 1621 cm^{-1}, is the same as found for x = 1.0. However, a small shoulder is visible around 1641 cm^{-1} reflecting the presence of free carbonyl groups. The shifts in the characteristic bands of the stretching modes of the pyridine ring are slightly smaller compared to the sample with a stoichiometric composition: 1595 to 1597 (+2) cm^{-1}, 1413 to 1417 (+4) cm^{-1}, and 992 to 1006 (+14) cm^{-1}. The small shifts observed for the pyridine bands are also reported in the literature for P4VP homopolymers with less than stoichiometric amounts of PDP.[27] The presence of free pyridine rings for x = 0.5 is furthermore supported by a residual absorption band at 992 cm^{-1} in Figure 8d which

is not present for x = 1.0. However, this band is not clearly visible due to the overlap of the absorption band of the phenyl ring of PDP near 1000 cm^{-1}. The results clearly indicate that PDP is hydrogen bonded to P4VP as well as PDMA, although it is impossible to conclude anything about the exact distribution of the amphiphile over both blocks.

5.3.2.2 Differential scanning calorimetry

DSC thermograms of P4VP(PDP)$_{1.0}$, PDMA(PDP)$_{1.0}$, [P4VP-*b*-PDMA](PDP)$_{0.5}$, and [P4VP-*b*-PDMA](PDP)$_{1.0}$ that were recorded during cooling from the melt with 5 °C min^{-1} from 120 to -20 °C, are presented in Figure 5.10. The thermogram of P4VP(PDP)$_{1.0}$ is showing an order-disorder transition (ODT) at 68.9 °C followed by a strong exothermic peak at 20.9 °C that corresponds to the crystallization of the alkyl tails of PDP, similar to results reported in the literature.[6]

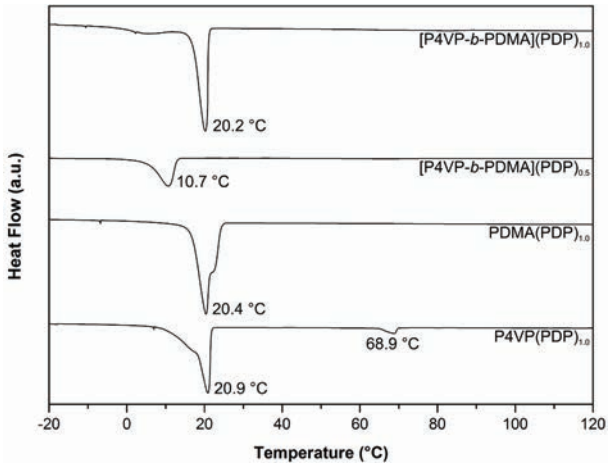

Figure 5.10 DSC thermograms recorded during cooling at 5 °C min^{-1} of P4VP(PDP)$_{1.0}$, PDMA(PDP)$_{1.0}$, [P4VP-*b*-PDMA](PDP)$_{0.5}$, and [P4VP-*b*-PDMA](PDP)$_{1.0}$.

The thermogram of PDMA(PDP)$_{1.0}$ also shows a strong exothermic peak at 20.4 °C due to the crystallization of the alkyl tails of PDP; however, no ODT is observed at higher temperatures. The presence of a small shoulder in the crystallization peak at 22.7 °C indicates that an ODT occurs at a temperature where after passing the ODT

the alkyl tails of PDP crystallize immediately. Increasing the cooling rate to 10 °C min^{-1} results in a shift of the crystallization temperature from 20.4 to 19.6 °C due to its dependence on the cooling rate (Figure 5.11). As a result, the ODT at 22.7 °C now becomes clearly visible as a separate peak.

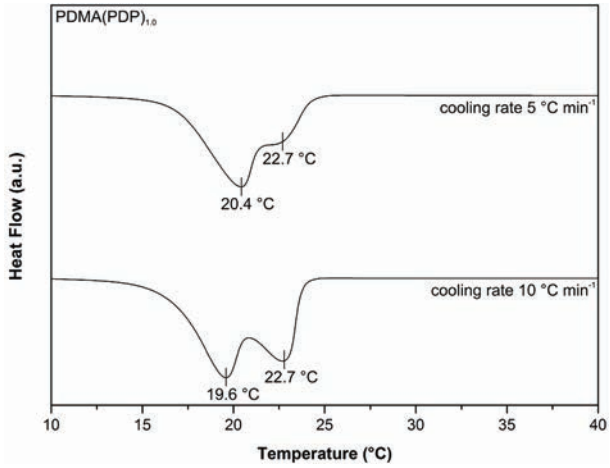

Figure 5.11 DSC thermograms of $PDMA(PDP)_{1.0}$ recorded during cooling at 5 °C min^{-1} and 10 °C min^{-1}, respectively. Increasing the cooling rate causes the peak due to the crystallization of the alkyl tails of PDP to shift from 20.4 to 19.6 °C resulting in the ODT at 22.7 °C to be clearly visible as a separate peak.

At first glance, the thermogram of [P4VP-*b*-PDMA]$(PDP)_{1.0}$ only seems to show an exothermic peak at 20.2 °C due to the crystallization of the alkyl tails of PDP. Even though the results from the infrared measurements clearly indicate that PDP is hydrogen-bonded to both blocks of the double-comb supramolecular complex, no ODT originating from the P4VP-PDP complex seems to be present at higher temperatures. Magnifying the area between 40 and 120 °C (see Figure 5.12)), however, revealed that between 58 and 88 °C a weak broad exothermic signal can be discerned, indicating the presence of an ODT. The signal is much weaker since there is less P4VP-PDP complex present during a measurement of the diblock copolymer than when the homopolymer-PDP complex is measured. The broadening of the signal may be due to the fact that locally the ODT depends on whether the PDP is

hydrogen-bonded to a pyridine group located either in the vicinity of the PDMA block or far away from it.

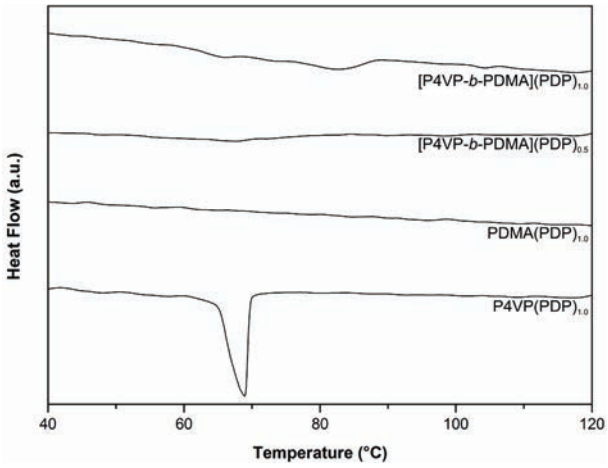

Figure 5.12 Scale expanded DSC thermograms between 40 and 120 °C recorded during cooling at 5 °C min^{-1} of $P4VP(PDP)_{1.0}$, $PDMA(PDP)_{1.0}$, $[P4VP\text{-}b\text{-}PDMA](PDP)_{0.5}$, and $[P4VP\text{-}b\text{-}PDMA](PDP)_{1.0}$.

Lowering the amount of PDP to x = 0.5 results in a reduction of the exothermic crystallization peak which is also appearing at a distinctly lower temperature. The reduction of the exothermic peak is caused by the fact that there is less PDP that can crystallize. The decrease in temperature at which crystallization occurs is thought to arise from the fact that the material needs more undercooling in order to crystallize due to the less efficient packing possibilities of the amphiphiles which are spread along the polymer backbone.

5.3.3 Self-assembly of the supramolecular double-comb diblock copolymer complex

5.3.3.1 Small angle X-ray scattering

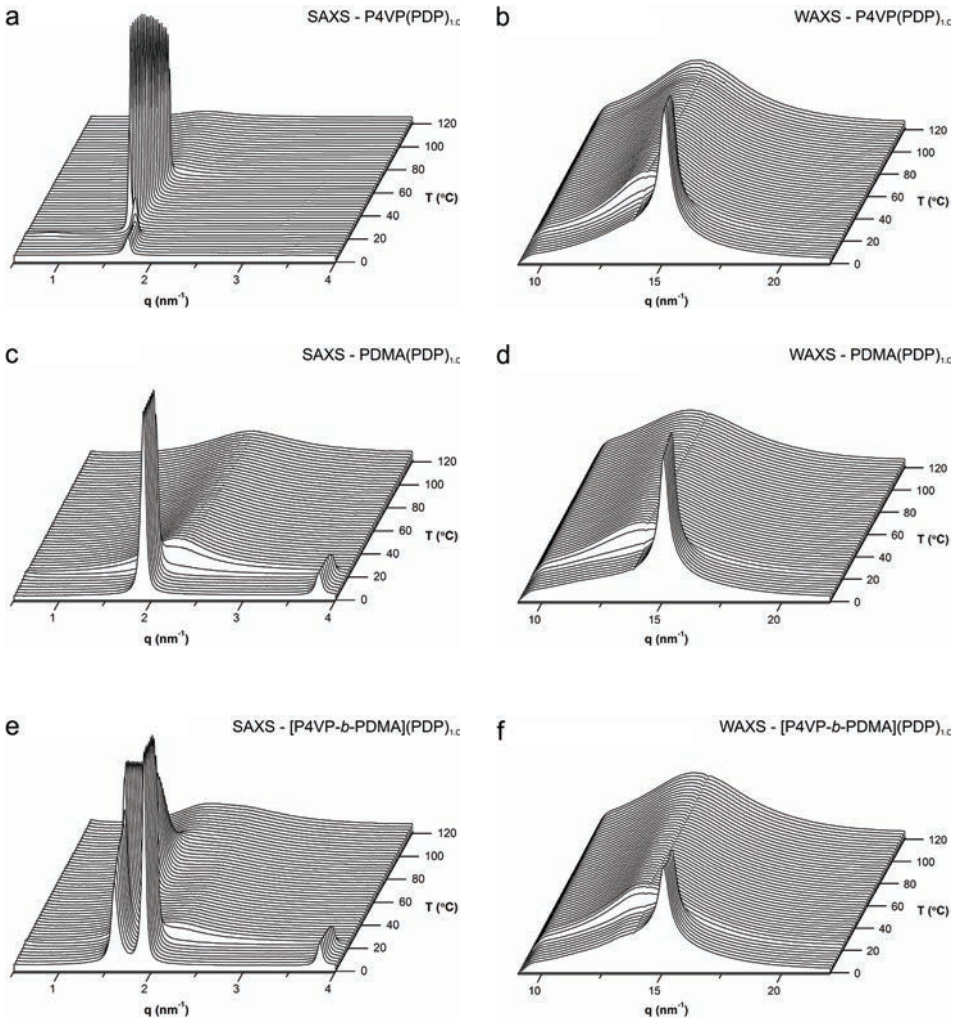

Figure 5.13 SAXS and WAXS intensity profiles of P4VP(PDP)$_{1.0}$ (a, b), PDMA(PDP)$_{1.0}$ (c, d), and [P4VP-*b*-PDMA](PDP)$_{1.0}$ (e, f) during cooling with 5 °C min^{-1} from the melt at 120 °C.

Simultaneous SAXS and WAXS measurements were used to investigate the self-assembled structures of the short length scale formed by the supramolecular complexes of both the homopolymers and the diblock copolymer with PDP. Figure 5.13 presents the SAXS (Figures 5.13a, c, e) and WAXS (Figures 5.13b, d, f) intensity profiles as a function of temperature during cooling from the melt with 5 °C min^{-1} from 120 to 0 °C for $P4VP(PDP)_{1.0}$, $PDMA(PDP)_{1.0}$ and $[P4VP\text{-}b\text{-}PDMA](PDP)_{1.0}$, respectively.

The SAXS intensity profile of $P4VP(PDP)_{1.0}$ in Figure 5.13a shows, as was already reported in the literature,[6] a strong increase in scattering around 65 °C when the temperature of the system is passing the ODT. On further cooling a second transition is observed at 20 °C at which the alkyl tails of PDP start to crystallize. These results of the SAXS and WAXS are in accordance with the DSC data. A very weak second order diffraction peak can be observed after passing the ODT at an angle twice as large as the angle of the main diffraction peak. Figure 5.14 presents the SAXS intensity profile for $P4VP(PDP)_{1.0}$ using a logarithmic scale for the intensity so that the second order diffraction peak can be observed more clearly. The ratio between the orders of diffraction q and $2q$ indicates a lamellar morphology[32] with a domain spacing of 3.8 nm. The domain spacing of the lamellar morphology decreases on crystallization to 3.6 nm due to better packing of the alkyl tails after the crystallization.

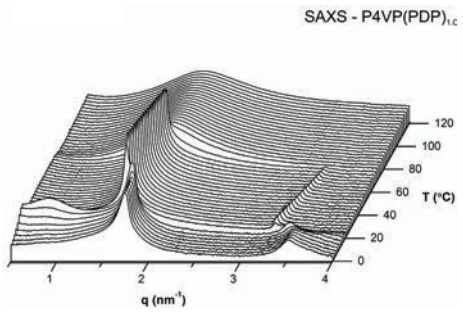

Figure 5.14 SAXS intensity profile $P4VP(PDP)_{1.0}$ during cooling with 5 °C min^{-1} from the melt at 120 °C. A logarithmic scale is used for the intensity in order to make the second order diffraction peak visible.

Confirming the results observed in the DSC thermogram, the SAXS intensity profile of PDMA(PDP)$_{1.0}$ in Figure 5.13c shows that there is no ODT present at higher temperatures. There is, however, a strong increase in scattering due to the crystallization of the side chains around 20 °C. As was already mentioned in paragraph 0, for the PDMA(PDP)$_{1.0}$ complex the alkyl tails of PDP start crystallizing immediately after passing the ODT. The lower ODT compared to the P4VP system indicates a slightly weaker repulsion. After crystallization a second order diffraction peak can be seen clearly at an angle twice as large as the main scattering peak, indicating a lamellar morphology with a domain spacing of 3.3 nm, slightly smaller than the domain spacing observed in the P4VP(PDP)$_{1.0}$ complex.

The SAXS intensity profile of [P4VP-*b*-PDMA](PDP)$_{1.0}$, Figure 5.13e, seems to consist of a combination of the intensity profiles found for the two supramolecular complexes of the homopolymers with PDP, albeit with some small differences. At higher temperatures, at which the system is in the melt, a characteristic correlation hole peak is present. The correlation hole peak in Figure 5.13e is wider than observed for both the separate homopolymer complexes and contains two weak maxima. On cooling, an ODT is observed around 85 °C for the "P4VP-PDP side" of the diblock copolymer while nothing appears to be happening on the "PDMA-PDP side". The temperature at which the ODT is observed is much higher than observed for pure P4VP(PDP)$_{1.0}$ alone. Apparently, the presence of the PDMA block with hydrogen-bonded PDP promotes the formation of an ordered state of "P4VP-PDP side" of the supramolecular diblock copolymer complex. It is also a clear indication that both supramolecular blocks are microphase separated at elevated temperatures. When decreasing the temperature even further, the crystallization of the alkyl tails takes place at 20 °C. This results in a change in intensity of the scattering peak on the "P4VP-PDP side" of the SAXS intensity profile and the appearance of a strong scattering peak and its second order peak on the "PDMA-PDP side".

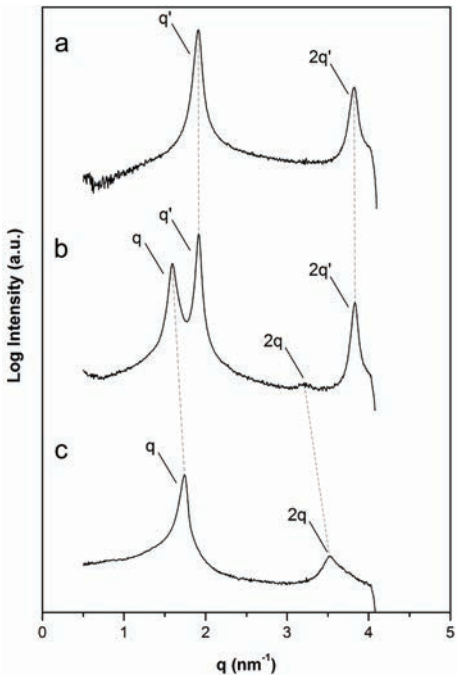

Figure 5.15 SAXS intensity profiles of PDMA(PDP)$_{1.0}$ (a), [P4VP-*b*-PDMA](PDP)$_{1.0}$ (b), and P4VP(PDP)$_{1.0}$ (c) at 0 °C after cooling with 5 °C min^{-1} from the melt at 120 °C.

In order to see these subtle differences more clearly, the SAXS intensity profiles obtained at 0 °C of P4VP(PDP)$_{1.0}$, PDMA(PDP)$_{1.0}$, and [P4VP-*b*-PDMA](PDP)$_{1.0}$ shown in Figures 5.13a, 4.13c and 4.13e, respectively, are again presented in Figure 5.15 using a logarithmic scale for the intensity. The gray dashed lines connect the scattering peaks observed for both P4VP(PDP)$_{1.0}$ and PDMA(PDP)$_{1.0}$ to the corresponding scattering peaks in the intensity profile of [P4VP-*b*-PDMA](PDP)$_{1.0}$. The scattering peaks originating from the "PDMA-PDP side" of the supramolecular diblock copolymer complex, q' and the second order 2 q', are positioned at exactly the same positions as found in the PDMA(PDP)$_{1.0}$ intensity profile. This indicates that the complex between PDMA and PDP results in a lamellar self-assembled morphology with a domain spacing of 3.3 nm in the homopolymer as well as in the diblock copolymer complex. As was already explained, the SAXS intensity profile of

P4VP(PDP)$_{1.0}$ in Figure 5.13a shows a shift of the primary scattering peak q to a larger angle on crystallization of the alkyl tails, indicating a decrease in the lamellar domain spacing due to interdigitation of the alkyl chains of PDP.[33] Using the logarithmic scale in Figure 5.15 clearly shows the presence of the second order in the intensity profile of P4VP(PDP)$_{1.0}$. Both q and $2q$ are also present in the intensity profile of [P4VP-*b*-PDMA](PDP)$_{1.0}$, only now at a slightly smaller angle. This indicates that the decrease in the domain spacing on crystallization of the alkyl tails of PDP is not taking place in the diblock copolymer complex, resulting in a lamellar morphology with a domain spacing of 3.9 nm in contrast to the 3.6 nm found in P4VP(PDP)$_{1.0}$. Apparently, the presence of the PDMA-PDP layers prevents the further interdigitation of the alkyl chains in the P4VP-PDP layers on crystallization. This is further supported by comparing the relative peak heights in Figures 5.13a and 5.13e. In Figure 5.13a the peak reduction on crystallization is very pronounced due to the diminished contrast, whereas in Figure 5.13e there is only a slight decrease in intensity.

The SAXS and WAXS intensity profiles of [P4VP-*b*-PDMA](PDP)$_{0.5}$ as a function of temperature during cooling from the melt with 5 °C min^{-1} from 120 to 0 °C are shown in Figure 5.16. Reducing x to 0.5 allows PDP to distribute over the polymer backbone evenly or preferentially bind to either P4VP or PDMA. At higher temperatures a broad correlation hole peak is present, indicating that both blocks contain hydrogen-bonded PDP. On cooling, a weak increase in scattering is observed on the "P4VP-PDP side" indicating the presence of an ODT. The scattering is much weaker than observed for a stoichiometric composition and is very slowly increasing upon decreasing the temperature. Upon lowering the temperature to 10 °C, at which the alkyl tails of PDP are crystallizing, the scattering peak originating from the "PDMA-PDP side" of the block copolymer starts to appear. Even though it is a weak scattering peak, a second order is clearly visible at twice the original angle. Upon crystallization, the "P4VP-PDP side" is shifting to a larger angle and is ending up as a shoulder on the left side of the PDMA-PDP scattering peak. In contrast to the stoichiometric composition, there is enough mobility in the system for the alkyl tails of PDP connected to P4VP to adopt a better packing upon crystallization. However, it is clear that even for less than stoichiometric compositions PDP distributes over both blocks with a slight preference for PDMA as indicated by the more intense scattering peaks.

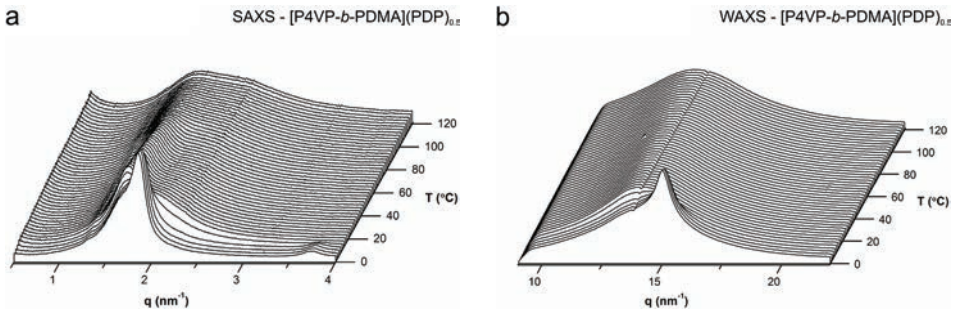

Figure 5.16 SAXS (a) and WAXS (b) intensity profiles of [P4VP-*b*-PDMA](PDP)$_{0.5}$ during cooling with 5 °C min^{-1} from the melt at 120 °C.

Although it is already clear that the diblock copolymer backbone is phase separated, it is not clear which self-assembled structure is formed. To establish which large length scale morphology is formed, additional SAXS measurements were performed using a setup with a larger sample-detector distance in order to observe scattering peaks at smaller angles. Figure 5.17 presents the SAXS and WAXS intensity profiles for [P4VP-*b*-PDMA](PDP)$_{1.0}$ obtained during cooling with 10 °C min^{-1} from 180 to 0 °C. Several intensity profiles at specific temperatures are shown separately in Figure 5.18.

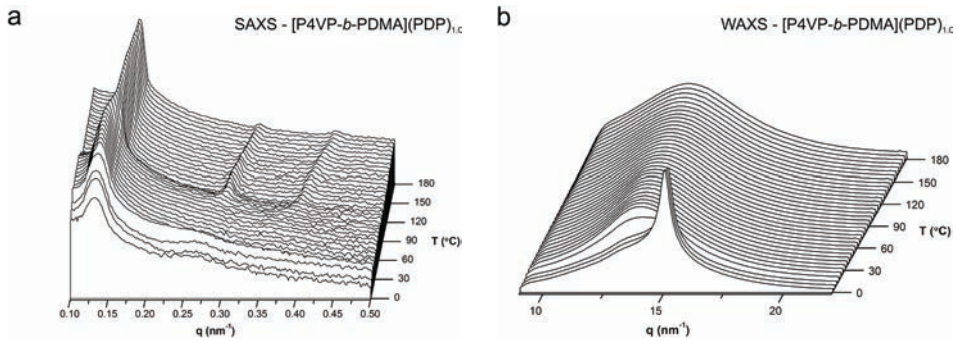

Figure 5.17 SAXS (a) and WAXS (b) intensity profiles of [P4VP-*b*-PDMA](PDP)$_{1.0}$ during cooling with 10 °C min^{-1} from the melt at 180 °C.

At temperatures above 70 °C up to three scattering peaks can be discerned located at a *q*-value ratio of 1:√4:√7, characteristic for a hexagonally packed cylinder structure (Figure 5.18).[32] The domain spacing is calculated to be about 39 nm. During cooling the dimension of the structure changes slightly as indicated by the shift of the scattering peaks to smaller angles. Below 70 °C, only a single scattering peak remains, rendering it impossible to draw a conclusion about the exact nature of the structure formed. When lowering the temperature below 15 °C, PDP starts to crystallize as can be clearly observed in the WAXS intensity profile shown in Figure 5.17b. The increase in the cooling speed, compared to the SAXS measurements performed on the short length scale, results in a lower crystallization temperature of the alkyl tails of PDP. After crystallization of the alkyl tails of PDP, two relatively broad scattering peaks are observed in SAXS with a ratio of 1:2, indicating that at least at this stage a lamellar morphology with a domain spacing of ca. 47 nm is present (Figure 5.18).

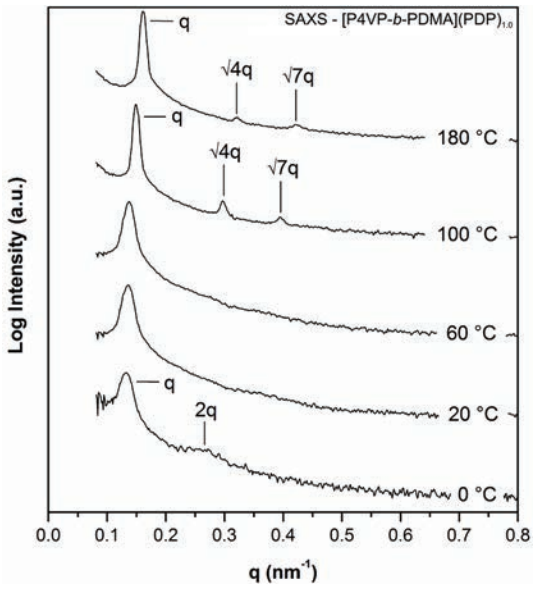

Figure 5.18 SAXS intensity profiles of [P4VP-*b*-PDMA](PDP)$_{1.0}$ at specific temperatures obtained during cooling with 10 °C min^{-1} from the melt at 180 °C.

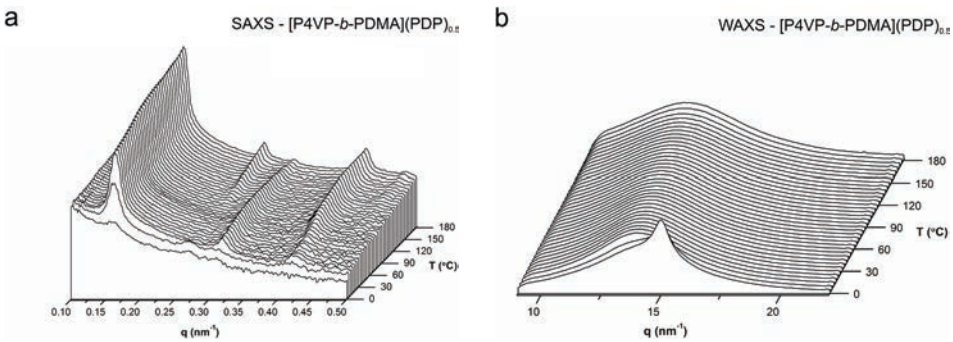

Figure 5.19 SAXS (a) and WAXS (b) intensity profiles of [P4VP-*b*-PDMA](PDP)$_{0.5}$ during cooling with 10 °C min^{-1} from the melt at 180 °C.

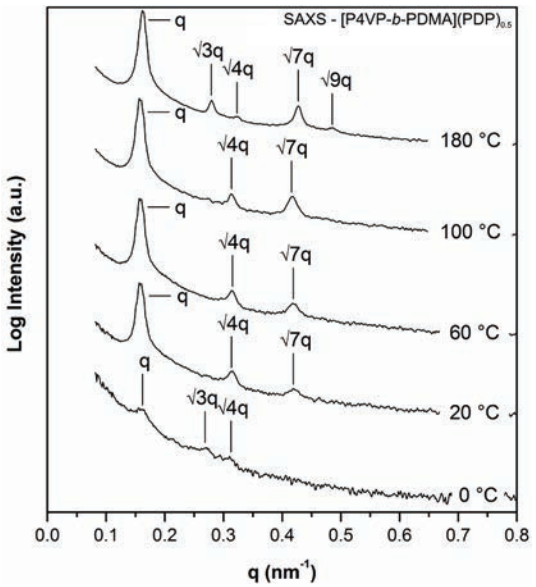

Figure 5.20 SAXS intensity profiles of [P4VP-*b*-PDMA](PDP)$_{0.5}$ at specific temperatures obtained during cooling with 10 °C min^{-1} from the melt at 180 °C.

Figure 5.19 presents the SAXS and WAXS intensity profiles for [P4VP-*b*-PDMA](PDP)$_{0.5}$ obtained during cooling with 10 °C min^{-1} from 180 to 0 °C. Several intensity profiles at specific temperatures are shown separately in Figure 5.20. The scattering peaks observed at 180 °C are at a ratio of 1:√3:√4:√7:√9, characteristic for a hexagonally packed cylinder structure. Cooling to a temperature of 100 °C, results in the disappearance of the scattering peaks at √3*q* and √9*q*, presumably due to a minimum in the form factor scattering. Upon lowering the temperature to 0 °C the scattering peak at √7*q* disappears while a weak peak at √3*q* can be observed again. The remaining very weak peaks at 0 °C are at a ratio of 1: √3*q*:√4*q* and have a domain spacing of 40 nm. In contrast to the lamellar morphology adopted by the [P4VP-*b*-PDMA](PDP)$_{1.0}$ after crystallization of the amphiphiles, the hexagonally packed cylinder structure is retained during the whole temperature scan.
Although the remaining part of this article will focus on the structures formed when a stoichiometric composition is used, further investigation on nonstoichiometric compositions could prove to be very interesting.

5.3.3.2 Shearing

The results of the SAXS measurements show that at sufficiently low temperatures both blocks of the diblock copolymer in the [P4VP-*b*-PDMA](PDP)$_{1.0}$ supramolecular complex are phase separated from each other as well as from PDP. All length scales correspond to a lamellar morphology. Most striking is the fact that for the short length scales both sides retain a difference in their respective layer spacing. This difference in layer spacing is even increased compared to the difference in the domain spacing between both homopolymer complexes due to the fact that on crystallization the alkyl tails on the "P4VP-PDP side" are prevented from adopting a better packing. The question arises how this self-assembled structure containing three different length scales is precisely realized. Therefore, alignment of a [P4VP-*b*-PDMA](PDP)$_{1.0}$ sample was undertaken to investigate their relative orientation. Large-amplitude oscillatory shear-induced (LAOS) alignment of a [P4VP-*b*-PDMA](PDP)$_{1.0}$ sample was conducted using a tooth rheometer.[18-20] The sample was loaded into the gap between the rheometer teeth couple of 5 by 3 mm at 80 °C, see Figure 5.21. After the required gap of 0.5 mm was set, the excess of sample around the tooth edges was removed prior to shear.

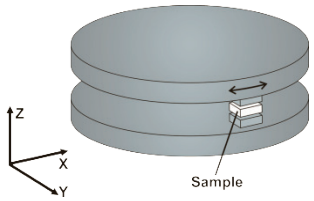

Figure 5.21 Illustration of the shearing plates of the tooth rheometer containing two teeth of the same size that are positioned on top of each other and the sample in between. Here, x is the tangential direction (direction of shear), y is the radial direction, and z the normal direction.

The [P4VP-*b*-PDMA](PDP)$_{1.0}$ sample was subjected to large-amplitude oscillatory shear with a strain amplitude γ of 85% and a frequency f of 1 Hz. Changes of the storage G' and loss G'' moduli and the phase angle ϕ measured in the LAOS mode are presented in Figure 5.22. As the shear starts, a steep decrease in G' and G'' and a steep increase in ϕ is observed during the first 10 min of the alignment. Further alignment is characterized by a gradual change in the rheological parameters until asymptotic values are reached.

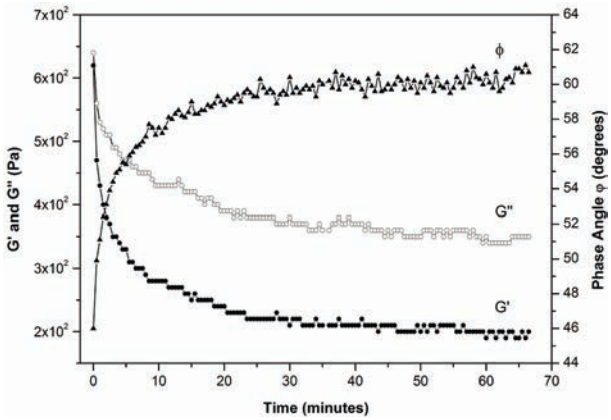

Figure 5.22 Changes of the dynamic G' and G'' moduli and the phase angle ϕ in time at 80 °C during the LAOS alignment of a freshly loaded [P4VP-*b*-PDMA](PDP)$_{1.0}$ sample, performed at f = 1 Hz and γ = 85%.

Shearing was stopped after ca. 1 h and the sample was allowed to cool gradually to room temperature. Prior to removal, the sample was further cooled with liquid nitrogen in order to remove the sample without destroying the alignment. The obtained shear-induced aligned sample was measured in the tangential (x-axis), radial

(y-axis), and normal (z-axis) direction using SAXS; the resulting 2D- and 3D-SAXS images are presented in Figure 5.23.

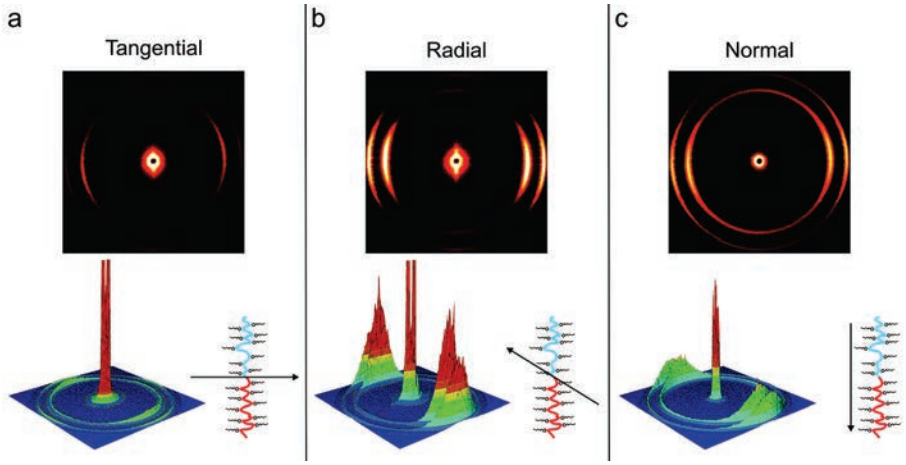

Figure 5.23 2D- and 3D-SAXS images obtained from SAXS measurements on the sheared sample in the tangential (a), radial (b), and normal (c) direction at room temperature after subjecting the sample to an oscillatory shear with a frequency of 1 Hz and a shear strain of 85% at 80 °C for ca. 1 h. The arrows indicate the direction of the SAXS beam relative to the orientation. The tangential direction corresponds to the direction of shear.

Comparing the obtained SAXS patterns presented shows that the measurements in the three different directions result in distinctly different SAXS patterns which clearly demonstrate the alignment of the sample. All images show an isotropic scattering ring as background of the reflections of the short length scale due to the fact that the sample is not perfectly ordered. The SAXS pattern obtained in the radial direction (Figure 5.23b) clearly shows the perpendicular orientation of the phase separated amphiphiles with respect to the phase separated polymer backbone. It also shows that the amphiphiles hydrogen-bonded to both blocks are orientated in the same direction. Furthermore, the polymer backbone is orientated perpendicular to the shear plane, while the amphiphiles are oriented parallel to the shear plane. This is confirmed by the measurements done in the normal and the tangential direction. In the normal direction (Figure 5.23c), when both blocks of the polymer backbone are in line, the scattering

peak close to the beam stop disappears and only the scattering peaks of the amphiphiles are visible. Moving to the tangential direction (Figure 5.23a), the direction of shear, the amphiphiles are mostly orientated in line of the X-ray beam, and therefore the reflections are severely reduced while there is a small scattering peak from the phase separated polymer backbone slightly visible close to the beam stop. The described orientations of the molecules of the supramolecular complex in relation to the direction of the SAXS measurements are also illustrated in in Figure 5.23.
The results indicate that in order for the self-assembled structure to fill space, the system should adapt the size of the lamellae near the boundary between the two blocks of the block copolymer. This can be achieved by distributing the chains of the diblock copolymer over different lamellae in a manner as depicted in Figure 5.24.

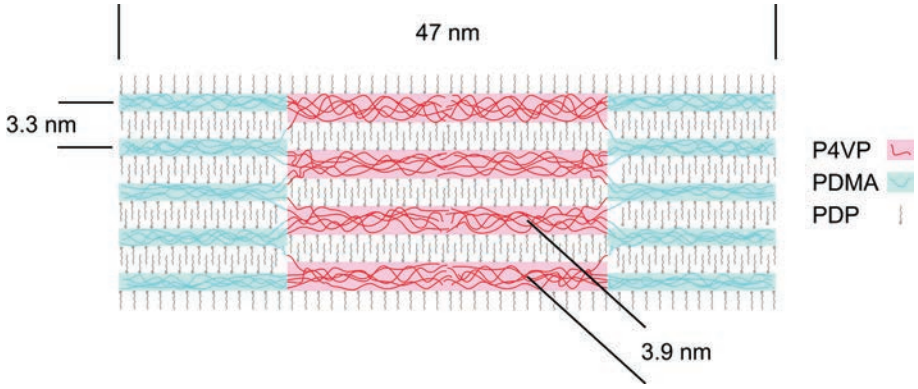

Figure 5.24 Illustration of the expected lamellar morphology formed in the microphase separated [P4VP-*b*-PDMA](PDP)$_{1.0}$ supramolecular complex.

5.3.3.3 Transmission electron microscopy (TEM)

The results obtained with SAXS are clearly indicating that upon self-assembly of the [P4VP-*b*-PDMA](PDP)$_{1.0}$ supramolecular complex a hierarchical morphology is formed. Especially the difference in the domain spacing of the short length scale lamellae requires further investigation using TEM. Since the samples are very hygroscopic, it was necessary to cut the samples under dry conditions using a cryo-microtome. Furthermore, it was necessary to use a cryo-TEM operating at liquid helium temperature in order to clearly image the sections without destroying the

structure. In TEM imaging of polymer systems, it is quite a common procedure to selectively enhance the contrast of certain parts of the formed morphology by staining these sections using an appropriate staining agent. For example, I_2 is often used for polymers containing P4VP. However, staining can be diffusion dependent and result in incomplete stained samples in which the observed structure is not the real self-assembled morphology. Furthermore, a very small difference in the domain spacing of the lamellae, of about 0.6 nm, needs to be observed unaltered by a selective staining agent. It is therefore necessary to observe the formed structure directly, without the use of a staining agent.

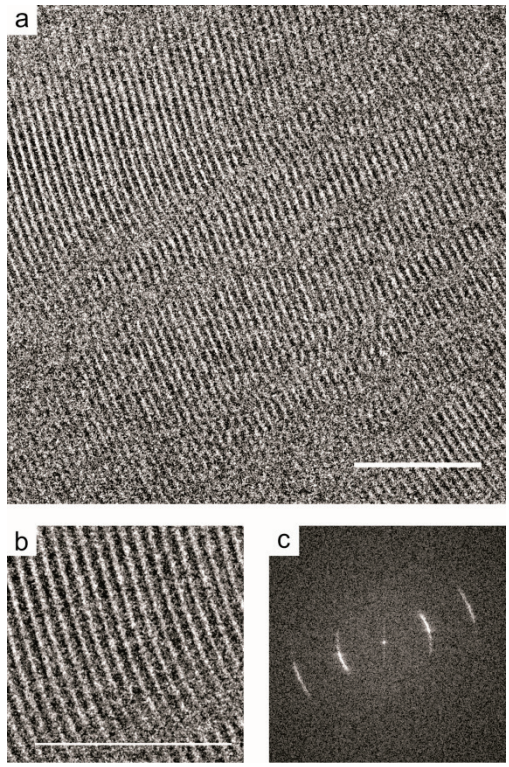

Figure 5.25 Bright-field TEM images of an unstained sample of the PDMA(PDP)$_{1.0}$ supramolecular complex, (a) and (b); both scale bars represent 50 nm. The result of the Fourier transformation for the image (a) is shown in (c).

TEM studies of P4VP-PDP and P4VP-NDP hydrogen-bonded systems have been reported in the literature.[6, 11] Although in these studies mainly I_2 staining is used to observe the morphology formed, it is possible to observe the lamellar morphology of the P4VP-PDP complex without the use of a staining agent. However, it was not clear if the PDMA-PDP lamellar morphology could be observed without staining. Figure 5.25 presents the TEM images of unstained thin sections of PDMA(PDP)$_{1.0}$. Enough contrast could be obtained in order to clearly observe the formed lamellar structure. The domain spacing of the lamellar morphology according to the TEM is 3.4 nm. The domain spacing found in SAXS is 3.3 nm; the small difference is probably caused by a slight difference in the calibration of both instruments used.

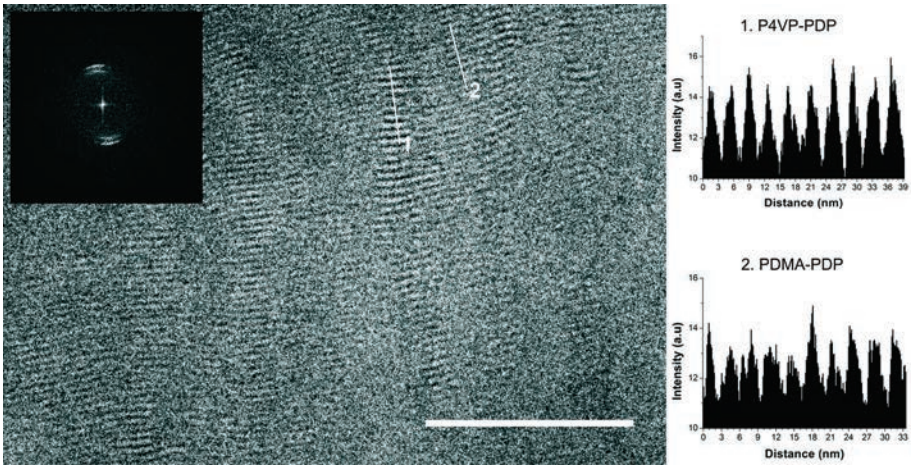

Figure 5.26 Bright-field TEM image of the [P4VP-*b*-PDMA](PDP)$_{1.0}$ supramolecular complex in which the dark regions correspond to the P4VP-*b*-PDMA domains. The inset shows the FFT of this image. The two white lines indicate the position at which the profiles shown on the right are created. Both profiles encompass 10 lamellae formed by the P4VP-PDP (1) and PDMA-PDP (2) phases. The scale bar represents 100 nm.

Since it is possible to view unstained P4VP(PDP)$_{1.0}$ as well as unstained PDMA(PDP)$_{1.0}$ separately in TEM, it is the challenge to image both morphologies at the same time. In Figure 5.26 a TEM image of an unstained sample of the

supramolecular complex is shown. Although the contrast in TEM of the PDMA-PDP complex in Figure 5.26 is very weak compared to the P4VP-PDP complex, clearly two lamellar morphologies with a different domain spacing are observed. The profile obtained at the positions indicated by the two white lines in the TEM image are taken of 10 lamellae and show a domain spacing in that area of ca. 3.9 and 3.3 nm, respectively. This is in accordance with the results found with the SAXS. The Fourier transform of the image, shown as an inset, confirms the presence of two length scales.

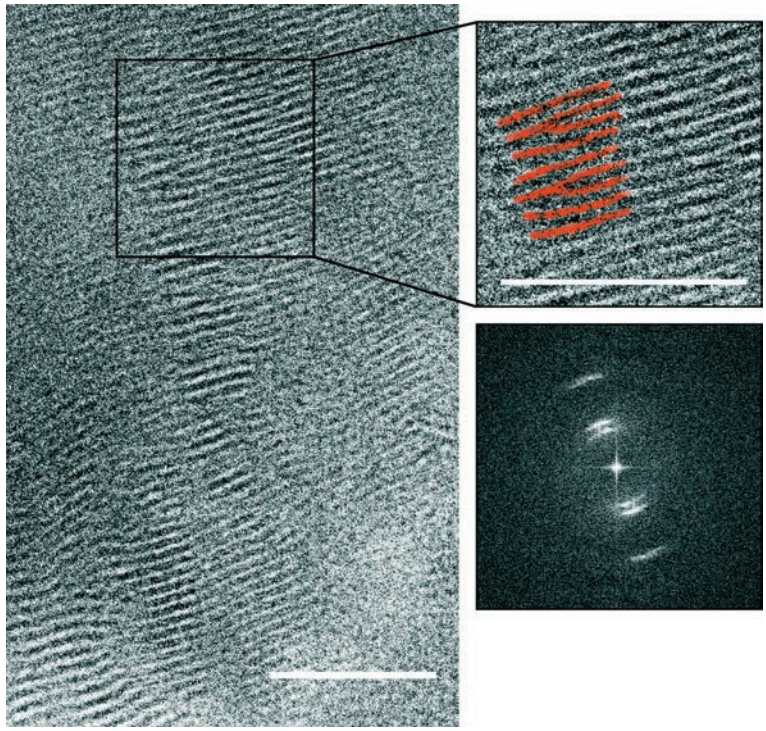

Figure 5.27 Bright-field TEM image of the [P4VP-*b*-PDMA](PDP)$_{1.0}$ supramolecular complex together with the result of the Fourier transformation of this image and an enlarged section as indicated by the black box. The dark regions correspond to the P4VP-*b*-PDMA domains. The red lamellae in the enlarged section of the TEM image indicate how the two lamellar morphologies are organized near the interface to incorporate the transition. Both scale bars represent 50 nm.

Figure 5.27 presents another TEM image of an unstained [P4VP-*b*-PDMA](PDP)$_{1.0}$ sample. Again a Fourier transform is shown, proving the presence of two lamellar domains. However, a more important aspect is the magnification of a section of the image, indicated by the black box, showing the area between the two lamellar complexes. For clarity, the lamellae in the area of interest are colored red. It clearly shows that, in order to facilitate the difference in the domain spacing, the PDMA part of the polymer backbone can cross over to other lamellae through the PDP layers near the interface between the two lamellar structures.

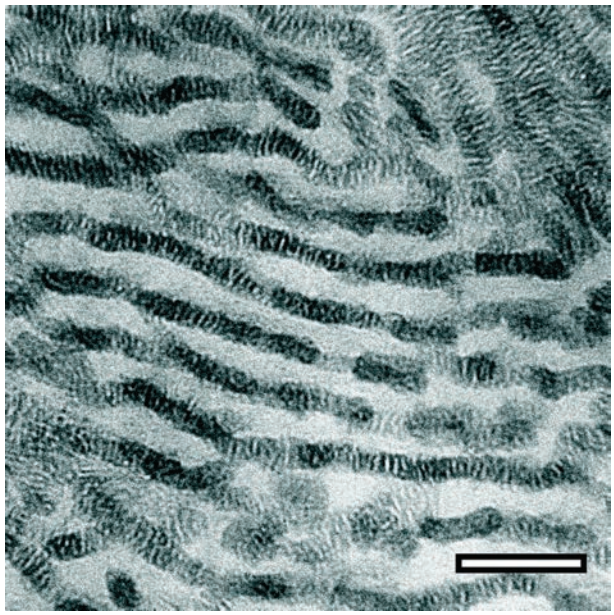

Figure 5.28 Bright-field TEM image of an iodine stained sample of the [P4VP-*b*-PDMA](PDP)$_{1.0}$ supramolecular complex. The sample was stained for about 5 min. The scale bar represents 100 nm.

Although the lamellae formed by P4VP-PDP as well as PDMA-PDP are visible, the large length scale still stays unresolved. In order to enhance the contrast between the two polymer phases, a sample was shortly stained with I_2. Figure 5.28 presents an image in which the P4VP phase is selectively stained showing a lamellar phase

separated morphology. Although it seems that the long-range ordering of the microphase separated structure is limited, it has to be taken into account that cutting the sample is very difficult and most likely destroys the morphology partly. Furthermore, some sections seem to contain more layers which results in "smeared" areas. Within the P4VP-PDP phase a smaller lamellar structure is visible perpendicular to the large length scale caused by the phase separation of P4VP and PDP. The small length scale has been distorted by the I_2 staining, as was expected. Although the PDMA(PDP)$_{1.0}$ phase seems to show no lamellar-in-lamellar morphology, closer inspection shows that such a lamellar morphology can be observed also within the PDMA-PDP phase, albeit very faint, when longer staining times are applied (Figure 5.29). The domain spacing of the lamellar structure formed by the phase separation of the block copolymer observed in TEM is found to be around 45 nm. This is slightly smaller but still consistent with the results found in SAXS.

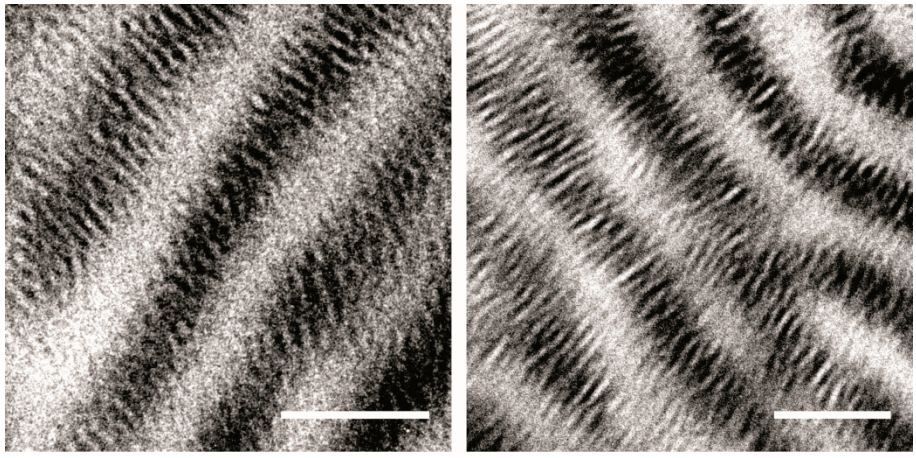

Figure 5.29 Bright-field TEM images of iodine stained samples of the [P4VP-*b*-PDMA](PDP)$_{1.0}$ supramolecular complex. The samples were stained for about 60 min. Both scale bars represent 50 nm.

5.4 Conclusion

RAFT polymerization of a P4VP-*b*-PDMA was performed successfully and resulted in a well-defined diblock copolymer. The formation of hydrogen bonds between PDP and both P4VP and PDMA was studied using infrared spectroscopy. Both blocks of the diblock copolymer in the supramolecular complex contain hydrogen-bonded PDP and therefore a supramolecular double-comb diblock copolymer is successfully obtained.

SAXS and TEM investigations show that the supramolecular complex of P4VP-*b*-PDMA with stoichiometric amounts of PDP results in a hierarchical lamellar-in-lamellar structure. A large length scale of about 47 nm is formed by the phase separation of the polymer backbone which can be clearly observed in TEM when the contrast is enhanced by staining with I_2. Both domains contain a smaller lamellar morphology orientated perpendicular with respect to the large length scale. The two small length scales originating from the phase separation of PDP and the block copolymer show a difference in domain spacing: 3.9 and 3.3 nm for P4VP-PDP and PDMA-PDP, respectively. This difference was already observed in the homopolymers, but it is retained, slightly increased even, in the [P4VP-*b*-PDMA](PDP)$_{1.0}$ supramolecular complex.

Self-assembled morphologies using double-comb diblock copolymer via a supramolecular principle proves to be very interesting, and a unique hierarchical structure is observed in the system studied here. Further investigations in bulk as well as in thin films are necessary to discover the scope of possibilities of such systems. Results obtained by reducing the amount of PDP to x of 0.5 already indicate that the morphology formed by the self-assembly of the diblock copolymer is altered to form a hexagonally packed cylinder structure with a domain spacing of 40 nm. Since the starting point was a nearly symmetric diblock copolymer, the presence of a large length scale cylindrical structure in both (x = 0.5 and 1.0) supramolecular systems investigated indicate the possibility of an uneven distribution of PDP over both blocks.

5.5 References

1. Rzayev, J.; Hillmyer, M. A. *J. Am. Chem. Soc.* **2005,** 127, (38), 13373-13379.
2. Lo, K. H.; Chen, M. C.; Ho, R. M.; Sung, H. W. *ACS Nano* **2009,** 3, (9), 2660-2666.
3. Park, M.; Harrison, C.; Chaikin, P. M.; Register, R. A.; Adamson, D. H. *Science* **1997,** 276, (5317), 1401-1404.
4. Osuji, C. O.; Chao, C. Y.; Ober, C. K.; Thomas, E. L. *Macromolecules* **2006,** 39, (9), 3114-3117.
5. Pollino, J. M.; Weck, M. *Chem. Soc. Rev.* **2005,** 34, (3), 193-207.
6. Ruokolainen, J.; Torkkeli, M.; Serimaa, R.; Komanschek, B. E.; Ikkala, O.; ten Brinke, G. *Phys. Rev. E* **1996,** 54, (6), 6646-6649.
7. Ikkala, O.; ten Brinke, G. *Science* **2002,** 295, (5564), 2407-2409.
8. Vukovic, I.; Voortman, T. P.; Merino, D. H.; Portale, G.; Hiekkataipale, P.; Ruokolainen, J.; ten Brinke, G.; Loos, K. *Macromolecules* **2012,** 45, (8), 3503-3512.
9. Sidorenko, A.; Tokarev, I.; Minko, S.; Stamm, M. *J. Am. Chem. Soc.* **2003,** 125, (40), 12211-12216.
10. van Zoelen, W.; Bondzic, S.; Landaluce, T. F.; Brondijk, J.; Loos, K.; Schouten, A. J.; Rudolf, P.; ten Brinke, G. *Polymer* **2009,** 50, (15), 3617-3625.
11. Ruokolainen, J.; Tanner, J.; Ikkala, O.; ten Brinke, G.; Thomas, E. L. *Macromolecules* **1998,** 31, (11), 3532-3536.
12. Ruokolainen, J.; Makinen, R.; Torkkeli, M.; Makela, T.; Serimaa, R.; ten Brinke, G.; Ikkala, O. *Science* **1998,** 280, (5363), 557-560.
13. Markov, V.; Subbotin, A.; ten Brinke, G. *Physical review. E, Statistical, nonlinear, and soft matter physics* **2011,** 84, (4 Pt 1), 041807.
14. Maeda, R.; Hayakawa, T.; Tokita, M.; Kikuchi, R.; Kouki, J.; Kakimoto, M.; Urushibata, H. *React. Funct. Polym.* **2009,** 69, (7), 519-529.
15. Zamfir, M.; Patrickios, C. S.; Montagne, F.; Abetz, C.; Abetz, V.; Oss-Ronen, L.; Talmon, Y. *J. Polym. Sci. Pol. Chem.* **2012,** 50, (8), 1636-1644.
16. Convertine, A. J.; Lokitz, B. S.; Vasileva, Y.; Myrick, L. J.; Scales, C. W.; Lowe, A. B.; McCormick, C. L. *Macromolecules* **2006,** 39, (5), 1724-1730.
17. Wong, K. H.; Davis, T. P.; Bamer-Kowollik, C.; Stenzel, M. H. *Polymer* **2007,** 48, (17), 4950-4965.
18. Polushkin, E.; van Ekenstein, G. A.; Dolbnya, I.; Bras, W.; Ikkala, O.; ten Brinke, G. *Macromolecules* **2003,** 36, (5), 1421-1423.
19. Polushkin, E.; van Ekenstein, G. A.; Ikkala, O.; ten Brinke, G. *Rheol. Acta* **2004,** 43, (4), 364-372.

20. van Ekenstein, G. A.; Polushkin, E.; Nijland, H.; Ikkala, O.; ten Brinke, G. *Macromolecules* **2003,** 36, (10), 3684-3688.
21. Borsboom, M.; Bras, W.; Cerjak, I.; Detollenaere, D.; van Loon, D. G.; Goedtkindt, P.; Konijnenburg, M.; Lassing, P.; Levine, Y. K.; Munneke, B.; Oversluizen, M.; van Tol, R.; Vlieg, E. *J. Synchrot. Radiat.* **1998,** 5, 518-520.
22. Bras, W.; Dolbnya, I. P.; Detollenaere, D.; van Tol, R.; Malfois, M.; Greaves, G. N.; Ryan, A. J.; Heeley, E. *J. Appl. Crystallogr.* **2003,** 36, 791-794.
23. Nikitenko, S.; Beale, A. M.; van der Eerden, A. M. J.; Jacques, S. D. M.; Leynaud, O.; O'Brien, M. G.; Detollenaere, D.; Kaptein, R.; Weckhuysen, B. M.; Bras, W. *J. Synchrot. Radiat.* **2008,** 15, 632-640.
24. Li, C. X.; He, J. P.; Zhou, Y. W.; Gu, Y. K.; Yang, Y. L. *J. Polym. Sci. Pol. Chem.* **2011,** 49, (6), 1351-1360.
25. Perrier, S.; Takolpuckdee, P. *J. Polym. Sci. Pol. Chem.* **2005,** 43, (22), 5347-5393.
26. Moad, G.; Rizzardo, E.; Thang, S. H. *Polymer* **2008,** 49, (5), 1079-1131.
27. Ruokolainen, J.; ten Brinke, G.; Ikkala, O.; Torkkeli, M.; Serimaa, R. *Macromolecules* **1996,** 29, (10), 3409-3415.
28. Eichhorn, K. J.; Fahmi, A.; Adam, G.; Stamm, M. *J. Mol. Struct.* **2003,** 661, 161-170.
29. Meaurio, E.; Cesteros, L. C.; Katime, I. *Macromolecules* **1997,** 30, (16), 4567-4573.
30. Hamou, A. S. H.; Djadoun, S. *Macromol. Symp.* **2011,** 303, (1), 114-122.
31. Yang, T. P.; Pearce, E. M.; Kwei, T. K.; Yang, N. L. *Macromolecules* **1989,** 22, (4), 1813-1818.
32. Hamley, I. W.; Castelletto, V. *Prog. Polym. Sci.* **2004,** 29, (9), 909-948.
33. Luyten, M. C.; van Ekenstein, G.; ten Brinke, G.; Ruokolainen, J.; Ikkala, O.; Torkkeli, M.; Serimaa, R. *Macromolecules* **1999,** 32, (13), 4404-4410.

Summary

Thanks to their intriguing properties, polymers are being used extensively in consumer goods as well as in advanced technologies. The simplest form of a polymer is a homopolymer in which the polymer consists of chemically identical monomers.
Block copolymers are formed by the coupling of two or more chemically distinct polymer chains. Self-assembly of these block copolymers results in intriguing nanoscale morphologies in bulk, thin films, and in solution, due to the repulsive interactions between the different blocks. The arising microphase separated structures are of interest for possible applications in nanotechnology in which they can be used as templates to create nanoscale objects previously not accessible or as nanoporous membranes after selective removal of one of the blocks. Subtle changes in the chemical structure of the monomers and the copolymer architecture can lead to enhanced control of the morphologies formed or even result in exciting new morphologies. It is therefore very important to obtain a better understanding of these parameters available to access and fine-tune specific morphologies, the domain spacing and the responsiveness to external stimuli.
This thesis describes the investigation of several self-assembling polymer systems, focusing on binary block copolymers and supramolecular complexes using hydrogen-bonding. The supramolecular complexes consist of low molecular weight amphiphiles connected to a polymer backbone. This principle can be employed to influence the self-assembly of diblock copolymers. An overview of the syntheses methods used and the relevant literature are described in Chapter 1.

Chapter 2 describes the synthesis and self-assembly of four poly(*tert*-butoxystyrene)-*b*-poly(4-vinylpyridine) diblock copolymers (P*t*BOS-*b*-P4VP) having different weight fractions of 4-vinylpyridine: *t*BOS$_{62}$-*b*-4VP$_{28}$, *t*BOS$_{62}$-*b*-4VP$_{199}$, *t*BOS$_{146}$-*b*-4VP$_{120}$, and *t*BOS$_{146}$-*b*-4VP$_{190}$ (subscripts indicate degree of polymerization). Although the system is quite similar to the extensively investigated polystyrene-*b*-poly(4-vinylpyridine) diblock copolymers (PS-*b*-P4VP), the presence of the *tert*-butoxy group at the para position of the phenyl ring of styrene changes the interaction parameter and therefore also the phase behavior observed. The interaction parameter reported in literature for this monomer pair, $\chi_{4\mathrm{VP},t\mathrm{BOS}}$, is approximately 0.39 as was determined using a random copolymer blend study.
The morphologies formed via self-assembly of the diblock copolymers were studied using small-angle X-ray scattering (SAXS) and transmission electron microscopy (TEM). Both the *t*BOS$_{62}$-*b*-4VP$_{199}$ and *t*BOS$_{146}$-*b*-4VP$_{120}$ diblock copolymers form remarkably well-ordered structures: lamellae and hexagonally packed P4VP cylinders, respectively. However, the *t*BOS$_{62}$-*b*-4VP$_{28}$ diblock copolymer showed a disordered morphology of P4VP spheres in a liquid-like short-range order. Based on $\chi_{4\mathrm{VP},t\mathrm{BOS}}$, the estimated value of χN exceeds 50 and for this level of segregation an ordered spherical morphology is expected. For the *t*BOS$_{146}$-*b*-4VP$_{190}$ surprisingly a bicontinuous gyroid morphology is observed despite the estimated strong segregation of $\chi N \cong 150$. Although the presence of the gyroid morphology at strong segregations has been observed before and this possibility has been theoretically confirmed, it remains a fact that it is mainly observed at weak to intermediate segregations. Based on the results it cannot be excluded that the value for $\chi_{4\mathrm{VP},t\mathrm{BOS}}$ found in literature is too high.

In Chapter 3 the self-assembly of symmetric A-*b*-(B-*b*-A)$_n$-*b*-B multiblock copolymers having large A- and B end-blocks is investigated using SAXS and TEM. A hexablock copolymer and an octablock copolymer, both with a large polystyrene (S) and a large poly-*p*-hydroxystyrene (*p*HS) end block, and 2 respectively 3 short inner S-*b*-*p*HS diblocks, have been synthesized successfully using sequential living anionic polymerization. For the hexablock a single periodic lamellar morphology was observed while the octablock showed a lamellar-in-lamellar self-assembled morphology in which two thin layers formed by the inner blocks are present inside the two thick layers

formed by the end blocks. The absence of additional "thin" layers in the hexablock copolymer is due to the small number of inner blocks and the relatively small molar mass of the inner blocks. Both results are in excellent agreement with the theoretical predictions for a comparable A-*b*-(B-*b*-A)$_n$-*b*-B-*b*-A two-length-scale binary multiblock copolymer system.

Chapter 4 investigates the supramolecular copolymer complex in which alkylpyridine amphiphiles are hydrogen-bonded to a poly(*p*-hydroxystyrene) homopolymer (P*p*HS). Although this complex is similar to the extensively studied poly(4-vinylpyridine)/3-pentacedylphenol (P4VP-PDP), remarkable differences are observed between the self-assembly of these two systems.
Three different 4-alkylpyridine amphiphiles were synthesized: 4-heptadecylpyridine (HDPy), 4-nonadecylpyridine (NDPy), and 4-heneicosylpyridine (HEPy). Infrared spectroscopy showed that the formed hydrogen-bonded complex between P*p*HS and HEPy is nearly complete when stoichiometric amounts are used. Competition with the intramolecular P*p*HS hydrogen-bonding seems to reduce the P*p*HS-HEPy hydrogen-bonding somewhat compared to the "reversed" P4VP-PDP system and as a result a small but significant fraction of pyridine groups is still free when stoichiometric amounts are used.
The formation of an ordered lamellar morphology depends on the length of the alkyl tail of the amphiphile and the amphiphile mole fraction x. When the alkyl tail is too short, as in the case of HDPy, they are not phase separated from the polymer backbone. Increasing the length of the alkyl tail from 17 to 19 or even 21 carbon atoms to obtain NDPy and HEPy, respectively, results in the formation of ordered structures of the respective supramolecular complexes. The crystallization of the alkyl tails is occurring at similar temperatures as for the pure amphiphiles, suggesting that the alkyl tails are phase separated from the polymer backbone. Upon cooling a lamellar ordered structure is obtained in which the domain spacing is dependent on the length of the alkyl tail.

Chapter 5 describes the synthesis and self-assembly of a supramolecular double-comb diblock copolymer complex in which 3-pentadecylphenol is hydrogen-bonded to both blocks of a poly(4-vinylpyridine)-*b*-poly(*N*,*N*-dimethylacrylamide) diblock copolymer

(P4VP-*b*-PDMA). The formation of hydrogen bonds between PDP and both P4VP and PDMA was studied using infrared spectroscopy. Both blocks contain hydrogen-bonded PDP and a supramolecular double-comb diblock copolymer was successfully obtained.

SAXS and TEM analysis show that the supramolecular complex of P4VP-*b*-PDMA with stoichiometric amounts of PDP results in a hierarchical lamellar-in-lamellar self-assembled structure. A large length scale of about 47 nm is formed by the phase separation of the polymer backbone. Both lamellar domains contain a smaller lamellar morphology orientated perpendicular with respect to the large length scale. The two small length scales originating from the phase separation of PDP and the block copolymer show a difference in domain spacing: 3.9 and 3.3 nm for P4VP-PDP and PDMA-PDP, respectively. This difference was already observed in the supramolecular complexes with the respective homopolymers, but it is retained, slightly increased even, in the [P4VP-*b*-PDMA](PDP)$_{1.0}$ supramolecular complex.

Self-assembled morphologies using double-comb diblock copolymer via a supramolecular principle proves to be very interesting, and a unique hierarchical structure is observed in the system studied here. Further investigations in bulk as well as in thin films are necessary to discover the scope of possibilities of such systems.

Samenvatting

Dankzij hun fascinerende eigenschappen worden polymeren veelvuldig toegepast in zowel consumentenartikelen als in geavanceerde technologieën. De eenvoudigste vorm van een polymeer is een homopolymeer bestaande uit een aaneenschakeling van chemisch identieke monomeren. Door het koppelen van twee of meer verschillende homopolymeren wordt een blokcopolymeer verkregen. Dankzij de vaak repulsieve interacties tussen de verschillende blokken treedt er in blokcopolymeren een spontane fasescheiding op. Dit resulteert in de formatie van een reeks geordende structuren op nanometerschaal. Dergelijke nanostructuren zijn zeer interessant vanwege de mogelijke toepassingen in de nanotechnologie. Het creëren van uiteenlopende nanostructuren met behulp van zelf-assemblage van blokcopolymeren en de toepassing daarvan is daarom een belangrijk onderwerp van vele wetenschappelijke studies. Subtiele verschillen in de chemische structuur van de gebruikte monomeren en in de architectuur van de blokcopolymeren kan leiden tot een verbeterde controle over de gevormde morfologie of kan zelfs resulteren in de formatie van geheel nieuwe structuren. Het is daarom zeer belangrijk om goed te begrijpen welke parameters van invloed zijn en in welke mate deze veranderd kunnen worden om zo unieke structuren mogelijk te maken, de grootte van de structuren te beïnvloeden of de responsiviteit op externe stimulatoren te vergroten.

Dit proefschrift beschrijft het onderzoek naar de synthese en zelf-assemblage van verschillende soorten blokcopolymeren waarbij de nadruk ligt op binaire blokcopolymeren en supramoleculaire complexen. De supramoleculaire complexen bestaan uit laagmoleculaire amfifielen gebonden aan een polymeerketen met behulp van waterstofbruggen. Het koppelen van de laagmoleculaire amfifielen aan een

polymeer kan worden gebruikt om de door zelf-assemblage gevormde structuren te beïnvloeden. Een overzicht van de gebruikte syntheses en de relevante literatuur wordt gegeven in hoofdstuk 1.

Hoofdstuk 2 beschrijft de synthese en zelf-assemblage van vier poly(*tert*-butoxystyreen)-*b*-poly(4-vinylpyridine) diblokcopolymeren (P*t*BOS-*b*-P4VP) met verschillende gewichtsfracties 4-vinylpyridine: *t*BOS$_{62}$-*b*-4VP$_{28}$, *t*BOS$_{62}$-*b*-4VP$_{199}$, *t*BOS$_{146}$-*b*-4VP$_{120}$, en *t*BOS$_{146}$-*b*-4VP$_{190}$ (subschriften geven de polymerisatiegraad aan). Ondanks dat dit systeem sterk lijkt op de veelvuldig onderzochte polystyreen-*b*-poly(4-vinylpyridine) diblokcopolymeren (PS-*b*-P4VP), zorgt de aanwezigheid van de *tert*-butoxygroep op de parapositie van de benzeenring van styreen voor een gewijzigde interactieparameter χ en daardoor ook voor een ander fasegedrag. De in de literatuur vermelde interactieparameter voor dit monomeerpaar, $\chi_{4\mathrm{VP},t\mathrm{BOS}}$, is ongeveer 0.39.
De gevormde structuren zijn onderzocht met behulp van kleine-hoekverstrooiing van röntgenstraling (SAXS) en elektronenmicroscopie (TEM). De zelf-assemblage van zowel *t*BOS$_{62}$-*b*-4VP$_{199}$ als *t*BOS$_{146}$-*b*-4VP$_{120}$ resulteerde in de verwachte structuren, respectievelijk lamellen en hexagonaal gepakte P4VP cilinders. De gevormde structuren worden gekenmerkt door hun zeer goede ordening. Het *t*BOS$_{62}$-*b*-4VP$_{28}$ diblokcopolymeer vormt echter een ongeordende structuur bestaande uit P4VP bollen met een vloeistofachtige ordening. De geschatte waarde voor χN voor dit systeem is groter dan 50 en voor een dergelijke mate van segregatie wordt juist een geordende sferische morfologie verwacht. Verassend genoeg vormt *t*BOS$_{146}$-*b*-4VP$_{190}$ een gyroïdstructuur wat juist opmerkelijk is vanwege de sterke segregatie van dit systeem ($\chi N \cong 150$). Ondanks dat de aanwezigheid van een gyroidstructuur bij een sterke segregatie al eerder is aangetroffen, zowel theoretisch als experimenteel, blijft het een feit dat de gyroïdstructuur voornamelijk voorkomt in systemen die zwakke tot middelmatige segregatie vertonen. Gebaseerd op deze resultaten kan niet worden uitgesloten dat de gevonden literatuurwaarde voor $\chi_{4\mathrm{VP},t\mathrm{BOS}}$ te hoog is.

In hoofdstuk 3 wordt de synthese en zelf-assemblage van symmetrische A-*b*-(B-*b*-A)$_n$-*b*-B multiblokcopolymeren met lange A- en B eindblokken beschreven. Een hexablokcopolymeer en een octablokcopolymeer, beide met lange polystyreen (PS)

en poly-*para*-hydroxystyreen (P*p*HS) eindblokken en respectievelijk 2 en 3 korte PS-*b*-P*p*HS middenblokken, werden gesynthetiseerd met behulp van anionische polymerisatie. Zelf-assemblage van het hexablokcopolymeer resulteerde in een lamellaire morfologie met een enkelvoudige periodiciteit. Het octablokcopolymeer gaf na zelf-assemblage een lamel-in-lamel structuur bestaande uit twee dunne lagen ingeklemd tussen twee dikkere lagen. De twee dunne lamellen worden gevormd door de korte middenblokken van het multiblokcopolymeer terwijl de grotere lamellen door de langere eindblokken worden gevormd. De afwezigheid van additionele dunne lagen in het hexablokcopolymeer wordt veroorzaakt door de kleinere hoeveelheid middenblokken samen met de relatief lage moleculaire massa van deze middenblokken. Beide resultaten zijn in overeenstemming met de theoretische voorspellingen gedaan voor vergelijkbare A-*b*-(B-*b*-A)$_n$-*b*-B-*b*-A multiblokcopolymeren.

In hoofdstuk 4 wordt het onderzoek beschreven naar supramoleculaire copolymeercomplexen waarin verschillende alkylpyridine amfifielen worden gebonden aan een P*p*HS homopolymeer. Dit systeem is vergelijkbaar met het uitgebreid onderzochte poly(4-vinylpyridine)/3-pentacedylphenol (P4VP-PDP), maar er blijken uitzonderlijke verschillen op te treden.
Voor dit onderzoek zijn drie verschillende 4-alkylpyridines gesynthetiseerd: 4-heptadecylpyridine (HDPy), 4-nonadecylpyridine (NDPy) en 4-heneicosylpyridine (HEPy). Infraroodspectroscopie laat zien dat formatie van waterstofbruggen in het complex nagenoeg volledig is als er stoichiometrische hoeveelheden worden gebruikt. Competitie met de intramoleculaire waterstofbrugvorming van P*p*HS blijkt de waterstofbrugvorming tussen P*p*HS en HEPy te reduceren. Dit resulteert in een kleine maar wel significante fractie aan vrije alkylpyridine.
Onderzoek met behulp van SAXS en WAXS toont aan dat de formatie van een geordende lamellaire structuur afhangt van de lengte van de alkylstaart van de alkylpyridine en de molfractie x. Een te korte alkylstaart, zoals in het geval van HDPy, zorgt er voor dat er geen fasescheiding plaats vindt. Verlenging van de alkylstaart van 17 naar 19 of zelfs 21 koolstofatomen (NDPy en HEPy) resulteert in de formatie van geordende structuren na zelf-assemblage van de supramoleculaire complexen. Het verlagen van de molfractie HEPy van 1,0 naar 0,5 laat zien dat er geen structuren meer gevormd worden.

De temperaturen waarbij de kristallisatie van de alkylstaarten in het supramoleculaire complex plaats vindt is gelijk aan de temperaturen gevonden voor de pure amfifielen. Dit suggereert dat de alkylstaarten fase-gescheiden zijn van de polymeerketen. Bij het afkoelen wordt een lamellair geordende structuur gevormd waarvan de lengteschaal afhangt van de lengte van de alkylstaarten.

Hoofdstuk 5 beschrijft de synthese en zelforganisatie van een supramoleculair 'dubbele kam' diblokcopolymeer waarin 3-pentadecylfenol (PDP) met behulp van waterstofbruggen gebonden is aan beide blokken van een poly(4-vinylpyridine)-*b*-poly(*N*,*N*-dimethylacrylamide) diblokcopolymeer (P4VP-*b*-PDMA). De formatie van waterstofbruggen tussen PDP en zowel P4VP als PDMA is geanalyseerd met infraroodspectroscopie. Beide blokken blijken gelijktijdig PDP te binden.
SAXS en TEM tonen aan dat het supramoleculaire complex van P4VP-*b*-PDMA met stoichiometrische hoeveelheden PDP resulteert in een hiërarchische lamel-in-lamel structuur. Een grote lamellaire structuur met lengteschaal van ongeveer 47 nm wordt gevormd door de fasescheiding van de twee blokken van het blokcopolymeer. Beide domeinen bevatten een kleinere lamellaire structuur die loodrecht op de grote lengteschaal is georiënteerd. Deze kleine lamellen worden gevormd door de fasescheiding tussen PDP en het blokcopolymeer. De lengteschaal van de kleine lamellen verschillen van elkaar: 3,9 nm voor P4VP-PDP en 3,3 nm voor PDMA-PDP. Dit verschil was al zichtbaar in de supramoleculaire complexen van PDP met de beide homopolymeren, maar het is opvallend dat dit behouden blijft in het supramoleculair complex van het blokcopolymeer. De unieke morfologie waargenomen in het supramoleculaire dubbele kam complex is zeer interessant en verder onderzoek is vereist om de mogelijkheden van dergelijke systemen verder te onderzoeken.

Dankwoord
Acknowledgements

Met het schrijven van deze laatste woorden voor mijn proefschrift komt ook het besef dat er nu echt een einde is gekomen aan een bijzondere periode. Het was een tijd met veel nieuwe uitdagingen en waardevolle ervaringen die mij op zowel wetenschappelijk als op persoonlijke vlak verder hebben gevormd. Met heel veel plezier maar af en toe ook met de nodige frustraties heb ik de afgelopen jaren intensief onderzoek gedaan en het resultaat hiervan ligt nu voor u. Deze resultaten waren echter nooit tot stand gekomen zonder de bijdragen van alle mensen waarmee ik aangenaam en productief heb samengewerkt. Daarvoor ben ik hen mijn dank schuldig.

Allereerst wil ik Prof. Gerrit ten Brinke en Prof. Katja Loos bedanken voor het vertrouwen en de mogelijkheid die zij mij hebben gegeven om mijn promotieonderzoek te mogen uitvoeren. Gerrit, ik heb het zeer bijzonder gevonden om met je samen te werken. Uiteraard ging er eerst heel veel synthesewerk aan vooraf maar uiteindelijk heeft het geresulteerd in interessante zelf-organiserende blokcopolymeren. Jouw gepassioneerde uitleg over waarom bepaalde structuren gevormd worden is altijd zeer inspirerend geweest.
Katja, I am very grateful that you encouraged me to stay a while longer after finishing my study. I enjoyed working with you and really appreciate that you were always available for advice. Your knowledge about the chemistry and the discussions we had about the results has been essential for my research.

I would also like to thank the members of my reading committee, Prof. O. Ikkala, Prof. Y. Matsushita, and Prof. dr. V. Abetz who have been so kind to evaluate my manuscript both quickly and thoroughly.

Graag wil ik een aantal mensen van de vaste staf van polymeerchemie bedanken die mij enorm geholpen hebben met het uitvoeren van metingen en het interpreteren van de verkregen data. Joop Vorenkamp, bedankt voor al je assistentie bij de GPC- en de infrarood metingen. Gert Alberda van Ekenstein, bedankt voor al je hulp bij de vele thermische analyses. Evgeny Polushkin, thank you for all the assistance with the SAXS measurements and the useful discussions. Not only in Groningen but also during the long working days in Grenoble.

I am grateful to the people at the Dutch-Belgian beamline (ESRF, Grenoble, France). Especially Dr. Wim Bras, Dr. Daniel Hermida Merino, Dr. Giuseppe Portale for their help during the measurements.
I am very grateful to Prof. Janne Ruokolainen en Jani Seitsonen for their help with the cutting and imaging of the water soluble 'double-comb' diblock copolymer. Without their help the results would not have been so impressive.
Ik ben verder Marc Stuart en alle andere mensen van elektronenmicroscopie zeer erkentelijk voor zijn hulp bij het gebruik van de microscoop.

Tijdens het onderzoek heb ik het genoegen gehad om samen te kunnen werken met aantal excellente studenten: Mark ten Cate, Nanda Harinck, Vincent Voet, Anton Hofman. Zonder jullie zouden zulke mooie resultaten niet mogelijk geweest zijn.
Vincent, vele uren hebben wij besteed aan het polymeriseren van multiblokcopolymeren met behulp van het hoog-vacuüm-systeem. Dankzij het zeer goede teamwork en de bijbehorende muzikale ondersteuning (initiatiesong, MJ) hebben wij zeer mooie resultaten verkregen.
Anton, jij hebt zowel je bachelor- als je masteronderzoek bij mij gedaan en wij hebben altijd goed kunnen samenwerken. Je hebt aan de basis gestaan van vele prachtige resultaten die terug te vinden zijn in dit proefschrift.
Vincent en Anton ik wens jullie beide veel succes met jullie eigen promotieonderzoek.

I enjoyed working with a lot of nice people during my years at the Polymer Chemistry department and I will name a few. Jeroen van der Vlist, sinds de studie komen wij elkaar met enige regelmaat tegen en altijd is er sprake van nuttige discussies, zeer goede samenwerking en veel plezier. Dank je daarvoor en ik ben blij dat we dit tijdens het

werk kunnen voortzetten. Wouter Kloosterman, mijn partner in de VVP, tijdens de MMC werkcolleges en tijdens de barbecues en feestjes. Dank je voor de gezellige tijd. Gerrit Gobius du Sart, ik ben je zeer dankbaar voor het bijbrengen van de fijne kneepjes van het hoog-vacuüm systeem en het tonen van de schoonheid van anionische polymerisatie. Jakob, I really enjoyed our frequent discussions on all kind of topics both on the lab and during the many short breaks. Ivana, it was a pleasure to have you as my colleague and I want to thank you for all your help, useful discussions and the great time in Grenoble. Karin bedankt voor alle gezelligheid en de hulp met het regelen van allerlei administratieve zaken. But of course also, in random order: Vladimir, Ralph, Joost, Teunis, Frans, Wendy, Sasa, Jelger, Leendert, Nienke, Yuliya, Tanya, Sergey, Prof. Arend-Jan Schouten, Berend, Sander, Wouter F., Thu, Milica, Pu Tian, Prof. Ton Loontjens, Carla, Laura, Yin Jie, Fei, Lia, Rachmawati, Jur, Anke, Minseok, Deepak, Prof. Andreas Hermann, Andreas B., Jan-Willem, Lieuwe-Jan, Steven, Thomas, Nemanja, Frank, Maarten, Arnoud, Christa, René, Anne-Marije, Tobias, Manfred, Diego, Alberto, Erythrina, Jelena, Salomeh, Lizette (Oudhuis), Albert, Danijela, Niels, Yvonne, Hinke, Dejan, Patrick, Kamlesh, Guiseppe, Zheng, Mark, Martijn, Agnieszka, Pavlo, Alina, Kai and all the other people I forgot to mention. Thank you for all the coffee breaks, drinks, barbecues and all the other memorable moments.

Mijn vader en moeder wil ik bedanken voor de steun en het vertrouwen die zij mij altijd hebben gegeven.

Lieve Lizette, zonder jouw steun was dit niet mogelijk geweest. Dank je voor je liefde, je onuitputtelijke geduld en de rust die jij uitstraalt. Samen met Alexander gaan wij genieten van alles wat er nog komen gaat.

Martin